RPSEA

FINAL TECHNICAL REPORT

12122.52.FINAL

Hugh Daigle, Nicholas W. Hayman, Kyle Spikes, Julia Gale,
Peter Eichhubl, Kitty L. Milliken
University of Texas at Austin

Connectivity between Fractures and Pores in Hydrocarbon-Rich Mudrocks

Contract Number 12122-52

June 24, 2016

Principal Investigator: Hugh Daigle
Assistant Professor
Department of Petroleum and Geosystems Engineering
University of Texas at Austin
200 E Dean Keeton St., Stop C0300,
Austin, TX 78712-1585

LEGAL NOTICE

This report was prepared by the University of Texas at Austin as an account of work sponsored by the Research Partnership to Secure Energy for America, RPSEA. Neither RPSEA, members of RPSEA, the National Energy Technology Laboratory, the U.S. Department of Energy, nor any person acting on behalf of any of these entities:

a. MAKES ANY WARRANTY OR REPRESENTATION, EXPRESS OR IMPLIED WITH RESPECT TO ACCURACY, COMPLETENESS, OR USEFULNESS OF THE INFORMATION CONTAINED IN THIS DOCUMENT, OR THAT THE USE OF ANY INFORMATION, APPARATUS, METHOD, OR PROCESS DISCLOSED IN THIS DOCUMENT MAY NOT INFRINGE PRIVATELY OWNED RIGHTS, OR

b. ASSUMES ANY LIABILITY WITH RESPECT TO THE USE OF, OR FOR ANY AND ALL DAMAGES RESULTING FROM THE USE OF, ANY INFORMATION, APPARATUS, METHOD, OR PROCESS DISCLOSED IN THIS DOCUMENT.

THIS IS A FINAL REPORT. THE DATA, CALCULATIONS, INFORMATION, CONCLUSIONS, AND/OR RECOMMENDATIONS REPORTED HEREIN ARE THE PROPERTY OF THE U.S. DEPARTMENT OF ENERGY.

REFERENCES TO TRADE NAMES OR SPECIFIC COMMERCIAL PRODUCTS, COMMODITIES, OR SERVICES IN THIS REPORT DOES NOT REPRESENT OR CONSTITUTE AN ENDORSEMENT, RECOMMENDATION, OR FAVORING BY RPSEA OR ITS CONTRACTORS OF THE SPECIFIC COMMERCIAL PRODUCT, COMMODITY, OR SERVICE.

Abstract

Several lines of evidence show that the majority of pores in mudrocks are at the nano-scale, many of them even below the resolution of electron microscopy. In laboratory- and reservoir-scale experiments and production efforts, fractures appear to govern the permeability of mudrocks. Although few detailed studies have been done, most of these induced and natural fractures appear to be spaced at approximately the centimeter scale or greater, raising the possibility that the surrounding rock deforms poroelastically. However, history-matching of production data and other lines of evidence suggest that the apparent matrix permeability surrounding fracture-stimulated wells in some cases is 100 times the value obtained in the laboratory. This suggests that fracture stimulation has additional effects on the shale matrix beyond the formation of the primary fracture network, allowing prolific hydrocarbon production in many cases. In this project we investigated the following question: Do fracture systems induced during stimulation and production form a network of connected flow pathways that access nano-scale porosity in a way that is important to the overall flow regime through mudrock?

To answer this question, we performed a suite of measurements on preserved samples of a siliceous oil-bearing shale from the northern Rocky Mountains as well as Eagle Ford shale samples from a well in Karnes County, Texas. These measurements centered on establishing the characteristics of the pore system in shale samples before and after shear failure induced in the laboratory. These consisted of measuring syn-deformational changes in nuclear magnetic resonance (NMR) T_2 response to "map" changes in pore structure during failure; measuring micropore size distributions using low-pressure N_2 and CO_2 adsorption on intact and failed material; measuring ultrasonic compressional and shear wave velocities during deformation and failure to characterize changes in dynamic elastic properties prior to and during failure; comparisons effective medium modeling and numerical simulation with ultrasonic measurements to help estimate changes in seismic response as a result of failure; and analysis of scanning electron microscope (SEM) and focused ion beam (FIB)-SEM images on intact and failed material to visually investigate the development, if any, of microcracks or other pore-scale changes as a result of shear failure.

We found that in most cases, cracks with apertures on the order of tens of nm developed after failure, and that these fractures propagated into the organic matter and intersected the organic-hosted pores, which would allow for enhanced production of hydrocarbons from their initial place of residence. This finding was based on NMR and gas adsorption results, which indicated an increase in pore volume in the 10-100 nm size range following shear failure, and imaging, which clearly showed the growth of cracks into organic matter, intersecting organic-hosted pores. This behavior is apparently driven by contrasts in mechanical strength at the grain scale, with clays deforming ductilely while causing fractures to propagate into more brittle organic matter.

THIS PAGE INTENTIONALLY LEFT BLANK

1. Introduction

Mudrocks are fine grained sedimentary rocks that are the dominant rock type in shale reservoirs currently targeted for gas and liquid exploration and production. A mixture of silt and clay-sized materials from a variety of geological sources, mudrocks can host hydrocarbon-rich pores that generally are at a sub-micron scale (Sondergeld et al., 2010a,b; Passey et al., 2010; SIlin and Kneafsey, 2012; Milliken et al., 2013). Given the size and heterogeneous distribution of mudrock pores, corresponding matrix permeabilities tend to be in the sub-microdarcy range (Javadpour et al., 2007). Therefore, most research on both production and contaminant transport has focused on fractures that provide fluid-flow pathways potentially leading to relatively high bulk permeabilities (Gale et al., 2007; Engelder et al., 2009; United States Environmental Protection Agency, 2011; Myers, 2012a,b; Williams-Stroud et al., 2013).
Mudrocks can fracture, as illustrated by: (i) largely cemented natural fractures that formed during their diagenetic histories, (ii) generally open fractures formed during core recovery and subsequent sample storage, and (iii) induced fractures that form during production (and waste-water injection) as monitored by production curves and seismic responses (Fisher et al., 2004; Warpinski et al., 2005; Gale et al., 2007; Maxwell et al., 2009; Milliken et al., 2012a,b; Frohlich, 2012; Keranen et al., 2013). Yet, as documented below and throughout the cited literature, core descriptions and quantitative microscopy of mudrock samples from a wide variety of basins exhibit fractures with predominantly ≥~centimeter spacing rather than over a complete range of fracture sizes and spaces. Notably, the microfractures that could enhance flow from the otherwise isolated pores appear to be scarce. We, therefore, ask the following question: *Following primary hydraulic fracture stimulation, is production possible only from larger-scale porosity, or is nano-scale porosity connected by networks of smaller fractures that develop during production?*

In order to answer this question, we envision two fluid-flow regimes (Fig. 1). In the first regime, hydrocarbons move through the mudrock pore system toward the fractures induced by hydraulic fracture stimulation, and once the hydrocarbon volume near the fractures is depleted, production rates decline rapidly because hydrocarbons that are located farther from the fractures are unable to migrate over production time scales. In the second regime, fractures exist not only because of hydraulic fracture stimulation but also within the rock volume between these main fractures. Flow may occur through additional microfractures produced by local stresses normal to the wall of the primary hydraulic fracture. In either case, hydrocarbons must still migrate through the pore system before reaching the fractures. Because the fracture network is more laterally extensive than individual induced fractures, the migration distance is shorter (order of cm), and more of the rock volume is available for production. Higher production rates and longer production durations may be sustained by availability of hydrocarbons throughout the entire rock volume, not just nearest to the main fracture system.

Different deformation mechanisms possibly govern the two possible fluid-flow regimes. For the regime where hydrocarbons are sourced locally around the induced fracture, deformation away from this fracture might be poroelastic. Accordingly, any hydrocarbon supplies would be short-lived as the stress dissipates and strain is recovered. In terms of the second fluid-flow regime,

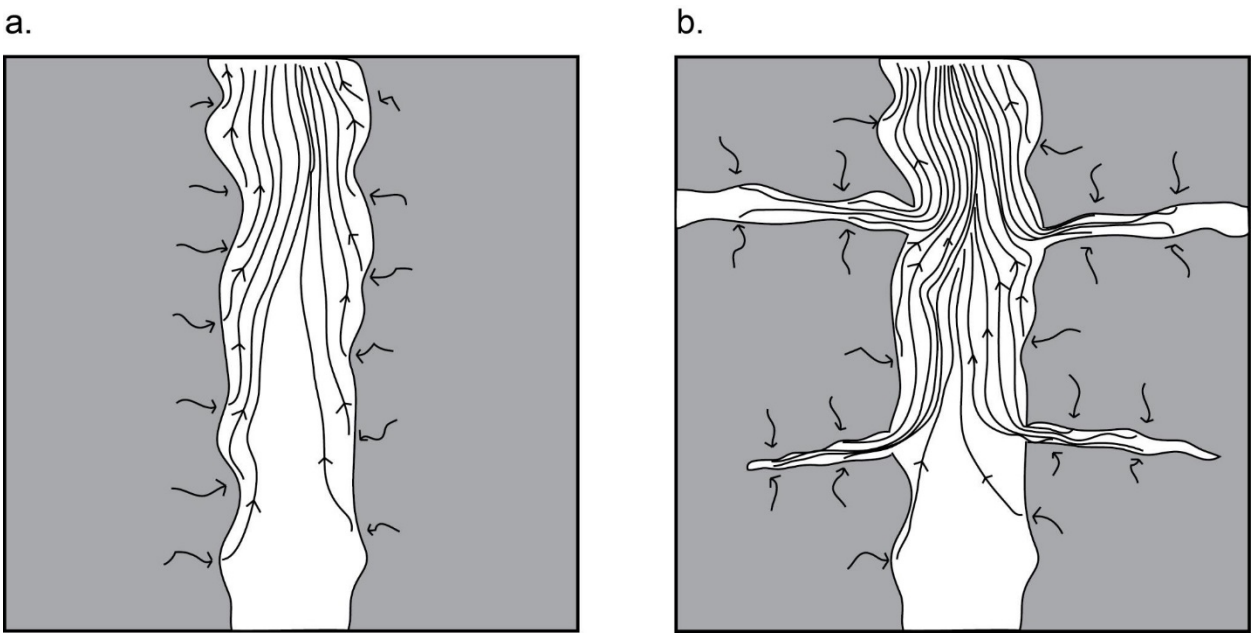

Figure 1. We consider two possible flow regimes. (a) Hydraulic fracture stimulation produces a fracture system that produces hydrocarbons only from the area immediately around the fracture. (b) Additional fractures are developed in the rock matrix due to local stress changes during fracture stimulation or production.

away from an induced fracture, strain might at first be poroelastic. At the grain scale, this poroelastic strain might depend on locations near minerals with larger elastic moduli and, importantly, on the initial pore shapes and their orientations relative to the direction of applied stress. Fluid-flow rates during this poroelastic phase might vary spatially where some pores might close but others open instantaneously. Where fluid migration can continue, viscoelastic (time-dependent) deformation will likely take place, dependent again on the local mineralogy (Tembe et al., 2010; Chang et al., 2006), in particular around the softer materials (clays and organic material). Deformation would continue in the areas where fluid-flow is enhanced by connected pores and microcracks, eventually forming larger-scale fracture networks. This deformation, by definition, will be permanent or plastic.

Mudrocks are characterized by fine-scale bedding cut by cemented natural fractures and, in outcrop or drill core, widely spaced bedding-parallel fractures and a second set at a high angle to bedding (Fig. 2a). Such fractures can have a range of spacing due to tectonic and burial/diagenetic history, as well as induced fracturing during production and coring, with widely (>tens of centimeters) to tightly (>0.5 cm) spaced joints (open fractures) (Fig. 2a), and networks of natural, cemented fractures (Fig. 2b) (Gale et al., 2007; Engelder et al., 2009). Both open and cemented fractures can serve as conduits for hydrocarbon flow at depth. Analysis of microseismic events combined with reservoir simulations and borehole logging data appear to confirm the importance of fractures in production, with great variability in scaling laws of fracture spacing, length, and aperture (Mayerhofer et al., 2008; Maxwell et al., 2009; Silin and Kneafsey, 2012; Williams-Stroud et al., 2013, and references therein). In these and related modeling efforts, fracture scaling laws are generally specified for lengths up to hundreds of

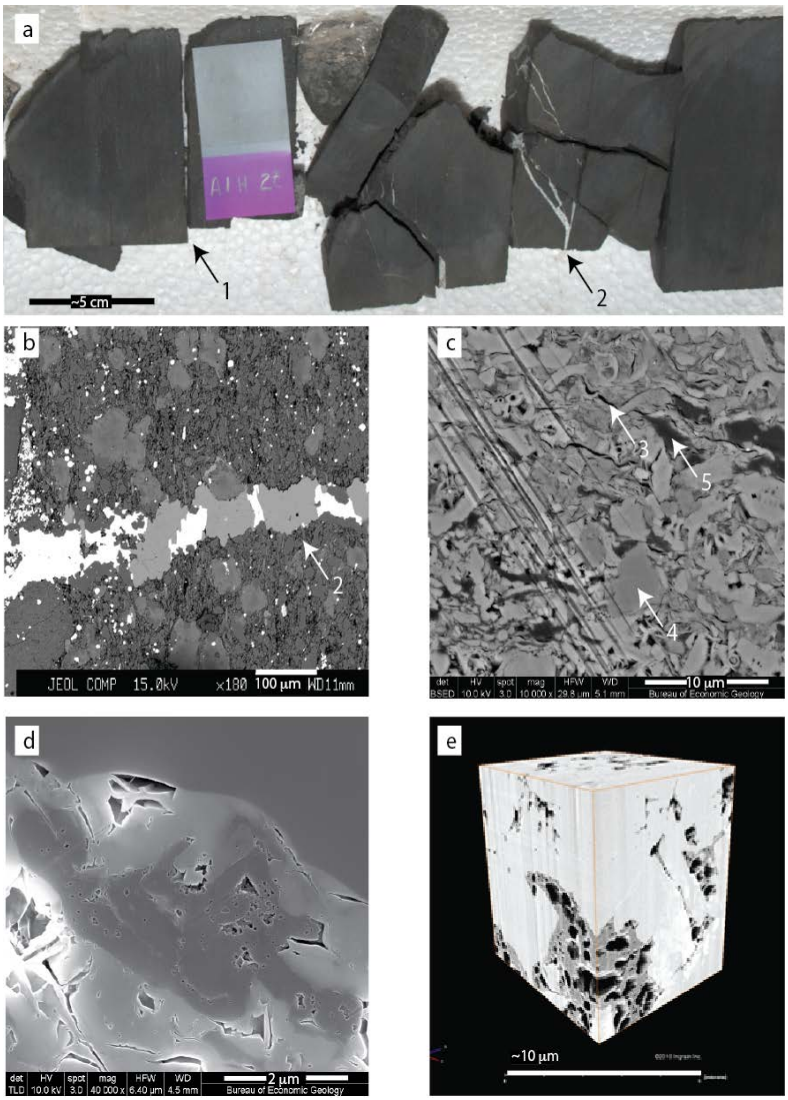

Figure 2. Examples of natural mudrocks at a variety of scales. (a) Mudrock core with coring-induced fractures (1), and natural, cemented fractures (2). (b) SEM image of a natural fracture (2) (from Milliken et al., 2012a). (c) Ion-milled (streaks on left side of image are artifacts of the ion-milling process) sample imaged in FESEM taken in the BEG microscopy laboratory showing silt-sized grains (3) creating inter-granular porosity (e.g., Loucks et al., 2009) (4). Note the organic material (5). (d) Organic material hosts porosity (center). (e) 3D rendering of multiple focused ion beam images (from Walls, 2011).

meters. And though aperture scales with length as addressed by some simulation efforts, few reservoir simulations explore the implications of the fine-scales of fracture density (spacing) distributions.

At the grain-scale, fractures are even scarcer, with mudrock textures defined by silt-sized particles in a matrix of finer-grained clay-sized material (Fig. 2c). In fact, the mudrock porosity is mainly in the form of nanopores (pore diameter < 0.1 micron; Katsube et al., 1992), typically making up 50-100% of the pore space (FIg. 2d) (Milliken et al., 2013). These pores are located in a range of materials including organic material (OM), within mineral and fossil fragments, and interstitially between silt- to clay- sized particles (Loucks et al., 2009; Schneider et al., 2011; Valenza et al., 2013). Furthermore, gas chromatography and other approaches such as X-ray scattering show that many tens-of-percent, to even >80%-95% of pores are at scales that cannot be resolved with SEM. Part of the reason for this distribution of porosity may be that it is located preferentially within OM, with intergranular porosity contributing a very small portion of the total porosity (Passey et al., 2010; Milliken et al., 2013). In these rocks, any hydrocarbon will therefore be present primarily in the nanopores within organic matter.

There is little understanding of how fractures access this nanoporosity. Schneider et al. (2011) visualized the porosity in mudrocks as primarily intergranular, with silt-grains supporting most of

the stresses “protecting” the matrix-porosity. Deformation of such material could allow a bulk poroelastic response as such “stress-bridges” are deformed and pores interconnect. On the other hand, as can be inferred from Fig. 2d, OM might behave in a rather ductile fashion, keeping pores from interconnecting. At the opposite extreme, we cannot rule out that this nanoporosity is rigidly contained within the clay-silt matrix, and only accessed by an as-yet undocumented microfracture network.

Bulk mineralogical and chemical changes in mudrocks during diagenesis strongly suggest that mudrocks are open systems with active fluid transport pathways that persist over large ranges of temperatures and pressures (Milliken, 2003). Fluid transport in mudrocks that have not been fracture stimulated occurs at scales ranging from Ångstroms in nanopores in organic matter to tens of microns in microcracks. At the smallest scales, diffusion is an important transport mechanism both within the pore space and between solid organic matter and the pore volume. These processes account for much of the transport within the intra- and interparticle pore volume. Naturally occurring microfractures can greatly enhance the permeability of mudrocks. These microfractures can have apertures of microns to tens of microns (Bolton et al., 2000) and can enhance permeability by 3-6 orders of magnitude relative to matrix permeability (Wang and Reed, 2009). Mudrock permeability is highly stress-dependent; Soeder (1988) reported a 70% decrease in permeability of an intact Marcellus shale core plug after doubling the confining pressure.

Geophysical characterization of mudrocks has ranged from the laboratory scale to field scale. Delle-Piane et al. (2011) investigated the intrinsic and crack-induced anisotropy of brine-saturated shale core plug samples under different external stresses. They found that elastic anisotropy of these samples depended on the composition and spatial distributions of different minerals and microfractures, and the change of anisotropy depended on the applied stresses, their orientations and the degree of stress anisotropy. This behavior has been modeled in various ways through excess compliance models (Pervukhina et al., 2011; Sayers, 2013) where lower stiffness in a particular direction is introduced through parallel planes of weakness. Alternate ways of describing this behavior include Chapman (2003, 2009), Spikes and Jiang (2013), and Jiang and Spikes (2013) who all use inclusion-based models to account for anisotropic conditions through aligned fractures and/or cracks. The positive side of using effective medium models is that they are predictive in terms of controlled perturbations of the inputs to obtain variational outputs. The drawbacks of the effective medium approaches are that they 1) rely on simply geometries that are not present at the imaging scale under question in this proposal; 2) homogenize the system and treat every material as poroelastic; and 3) are not capable of explaining the deformation process leading to the formation of microfractures. To accommodate the complex rheology in a geophysical sense, a wave must be propagated through a model of the fine-scale rock structure. Wave propagation approaches at this scale have been employed on micro-images of sandstones (e.g., Madonna et al., 2013) to provide comparisons to measured wave speeds.

2. Technical work

The following technical work was to be performed under Task 5.0 of the Statement of Work for this project.

Subtask 5.1 NMR Measurements

NMR T_2 measurements shall be conducted by the subcontractor to assess change in pore space and opening of microcracks during deformation of a mudrock sample. NMR T_2 measurements will be performed using an Oxford Instruments GeoSpec2 2 MHz system on mudrocks in as received state. During measurement, samples will be subjected to an initial confining pressure, and then confining stress will be increased rapidly while maintaining axial stress. At least 10 experiments shall be performed. The maximum confining and axial stresses applied shall be 5000 psi. Following this, confining stress will be decreased rapidly. This stress path will be designed to simulate conditions experienced during a hydraulic fracture stimulation. During the initial loading, the bulk deformation before failure, during failure and post-failure relaxation will be characterized. The internal strain of the sample will be monitored via the T_2 response while monitoring the experimental boundary stresses. The aim is to see how the matrix T_2 values change with stress, and the stress at which evidence of microcracks appears, manifested in appearance of larger T_2 values in the distribution. Additionally, microstructural and sample-scale geophysical-property changes during these stages will be accessed by investigating samples with bulk-rock porosity measurements and microscopy of samples from some experimental runs which do not reach failure, and contrasting those with others that do. At least 10 samples shall be analyzed in this manner.

Subtask 5.2 Gas Adsorption/Desorption Measurements

Following the NMR measurements, N_2 and CO_2 gas adsorption/desorption measurements shall be performed by the subcontractor on dried, crushed samples using a Micromeritics 3Flex 3500 system. At least 10 samples will be taken from material before and after deformation during NMR measurements for 20 total samples. Though this bulk measurement does not characterize microstructural complexity, it provides first-order pore size distributions for the samples that may be compared with NMR T_2 distributions to quantify the relationship between pore size and T_2. Pore size distributions will be determined from the adsorption data using nonlocal density functional theory.

Subtask 5.3 Acoustic Measurements

In parallel with the NMR and gas adsorption/desorption measurements, a triaxial testing apparatus shall be used by the subcontractor to measure compressional and shear wave velocities on samples undergoing triaxial consolidation. The compressional and shear wave velocities shall be used along with bulk density values determined from sample mass and volume to calculate dynamic bulk and shear moduli. The purpose of these measurements is to characterize the change in dynamic elastic properties as mudrocks are subjected to stress and approach failure. Acoustic velocities will be measured in axial and radial directions to characterize anisotropic properties for linking pore system evolution to properties that are measurable from acoustic logs and seismic data.

Subtask 5.4 Geophysical Modeling

The subcontractor shall compare seismic experimental results with both effective medium models and numerical simulations. The numerical simulations will come from finite element wave propagation modeling using a discontinuous Galerkin method. This method is designed to handle discontinuities in the numerical mesh and in the wavefield and is the best suited wave-propagation method to handle the complex topology expected in micro-structure images. These comparisons will be made on samples both pre- and post-deformation to obtain an estimate of the change in the seismic response due to mechanical failure.

The first pass will be to turn the SEM images (Subtask 5.5) into binary segmented models to establish initial meshing and appropriate boundary conditions. To adjust the effective velocities in the wave propagation to match the experimental results, well known mineral moduli for quartz, calcite, pyrite, and clays will then be input. Lastly, the (albeit poorly) known moduli for clays and organic content will be input and varied accordingly.

In relationship to the obtainable acoustic and shear measurements (Subtask 5.3), anisotropic (VTI) effective medium models will be employed with a free parameter (the fifth elastic constant) to allow adjustment to fit experimental results. Similarly, the numerical simulations can be computed by propagating both P and S waves in orthogonal directions through the images.

Subtask 5.5 Imaging

Pre- and post-deformational samples will be imaged with SEM. These measurements will be performed following the NMR (Subtask 5.1) and acoustic/triaxial consolidation measurements (Subtask 5.3). Additionally, an essential feature of our hypothesis-test will be to image the pre- and post-experimental material in three dimensions. Quantitative analysis of the imaged (imaged in both 2- and 3-D) microstructures will be done by construction of pore and grain networks from segmented images.

3. Description of results

3.1 Description of Samples

We received 8 preserved 2/3-round core samples from EOG Resources, each 5-8” in length. 5 of these were from a well drilled in a siliceous, oil-bearing shale in the northern Rocky Mountains (hereinafter referred to as “Siliceous”), and 3 were from a well drilled in the Eagle Ford shale in Karnes County, Texas. Samples of each core were sent to Weatherford Laboratories in Houston, Texas for x-ray diffraction (XRD) and rock-eval/pyrolysis analyses. These analyses identified the mineralogical composition of each sample, as well as organic matter abundance, type, and maturity. Results are shown in Tables 1 and 2.

Sample	CLAYS				CARBONATES			OTHER MINERALS							
	Chlorite	Kaolinite	Illite/Mica	Mix I/S*	Calcite	Dolomite[1]	Dolomite (Fe/Ca*)[2]	Quartz	K-spar	Plag.	Pyrite	Marcasite	Apatite	Gypsum	TOC**
Sil 3-14	1	1	18	18	3	Tr	Tr	39	Tr	11	5	Tr	Tr	0	4
Sil 3-42	1	1	12	10	1	1	1	52	Tr	8	7	0	1	Tr	5
Sil 3-53	1	1	9	10	1	1	2	52	Tr	13	7	Tr	Tr	Tr	3
Sil 4-14	1	1	9	9	Tr	1	3	60	Tr	8	4	Tr	0	0	4
Sil 4-34	2	Tr	18	13	Tr	1	1	50	Tr	8	3	0	1	0	3
EF 1-223	Tr	1	10	8	60	Tr	Tr	13	Tr	3	1	1	0	0	3
EF 2-50	1	Tr	18	20	38	Tr	Tr	13	Tr	2	3	1	0	Tr	4
EF 2-93	Tr	Tr	6	6	67	1	Tr	9	Tr	1	4	1	Tr	0	5

Table 1. XRD analysis results. Values are in weight percent. Sil = Siliceous; EF = Eagle Ford; TOC = total organic carbon.

*Ordered interstratified mixed-layer illite/smectite; approximately 15-25% expandable interlayers.

[1]Dolomite species interpretation based on the d-spacing of the highest intensity peak of dolomite group minerals; other dolomite species may be present.

[2]Dolomite species interpretation based on the d-spacing of the highest intensity peak of dolomite group minerals (which increases with calcium in excess of 50:50 Ca:Mg or substitution of Fe for Mg).

**TOC values from geochemical analysis, not XRD.

Sample	TOC (wt %)	S1	S2	S3	Tmax (°C)	HI	OI
Sil 3-14	4.40	4.54	2.60	0.37	454	59	8
Sil 3-42	4.56	5.02	2.72	0.43	460	60	9
Sil 3-53	3.15	2.42	1.56	0.25	452	50	8
Sil 4-14	3.64	5.18	2.36	0.21	459	65	6
Sil 4-34	2.82	2.58	1.57	0.24	457	56	9
EF 1-223	3.12	8.69	4.83	0.46	445	155	15
EF 2-50	3.79	7.26	5.44	0.45	444	144	12
EF 2-93	4.73	7.83	4.92	0.41	448	104	9

Table 2. Rock-eval/pyrolysis results. Sil = Siliceous; EF = Eagle Ford; TOC = total organic carbon; S1 = volatile hydrocarbon (HC) content, mg HC/g rock; S2 = remaining HC generative potential, mg HC/g rock; S3 = CO_2 content, mg CO_2/g rock; HI = hydrogen index = S2*100/TOC, mc HC/g TOC; OI = oxygen index = S3*100/TOC, mg CO_2/g TOC.

3.2 Subsampling Procedure

To produce core plugs and additional material necessary for measurement, the cores were subsampled using a 1"-diameter rotary coring drillbit with mineral oil as a lubricating fluid. When possible, two plugs were taken orthogonal to the borehole axis (i.e., horizontal in a vertical well or bedding parallel) and one plug was taken parallel to the borehole axis (i.e., vertical in a vertical well or bedding perpendicular). One of the horizontal core plugs was used for the NMR measurements, while the other horizontal plug and the vertical plug were used for the triaxial deformation/acoustic measurements. The resulting core plugs were cylinders 1" in diameter and 1-2" in length. Due to difficulty in coring shales, not every core could be subsampled in this level of detail. This was a particular problem in obtaining vertical core plugs, since the rock had a tendency to part along bedding planes due to torque within the core barrel. A summary of core plugs produced is shown in Table 3. All cores and carcasses were preserved in mineral oil after subsampling.

Prior to testing, roughly 1 cm of material was removed from the bottom of the core plugs for imaging. After testing, a 1-cm slice of material from the middle of each core plug was removed for imaging. Intact material for gas adsorption measurements was taken from the carcass of each core; deformed material was taken from core plugs after testing.

Sample	Horizontal 1	Horizontal 2	Vertical
Siliceous 3-14	X	X	X
Siliceous 3-42	X		
Siliceous 3-53	X		X
Siliceous 4-14	X		
Siliceous 4-34	X		
Eagle Ford 1-223	X	X	X
Eagle Ford 2-50	X	X	X
Eagle Ford 2-93	X	X	

Table 3. Summary of core plugs produced from received samples. Horizontal 1 = samples for triaxial deformation/acoustic measurements; Horizontal 2 = sample for NMR measurements; Vertical = samples for triaxial deformation/acoustic measurements.

3.3 NMR Measurements

NMR measures transverse relaxation times of hydrogen nucleus spin precession (T_2), which is used to infer distribution of pore sizes (Fig. 3) (Kenyon et al., 1995). This technique has been used to characterize distribution of pore sizes as small as 3 nm (Sondergeld et al., 2010a,b). NMR is typically unable to detect pores smaller than ~3 nm due to the extremely fast relaxation of hydrogen in small pores. Correlating T_2 with pore size requires comparing T_2 distributions with pore size distributions measured by other techniques such as mercury injection or gas adsorption/desorption. NMR is valuable particularly for inferring the presence of fractures, which are typically many orders of magnitude larger than pores in mudrocks (e.g., Fig. 2b) and have correspondingly larger T_2 values.

We performed measurements on an Oxford Instruments GeoSpec2 2 MHz benchtop NMR system equipped with a pressure vessel manufactured by Core Laboratories. Core samples were sealed in a polymer membrane and loaded into the pressure vessel. The pressure vessel was then filled with Fluorinert confining fluid, which is composed of carbon chains in which the hydrogen atoms have been replaced with fluorine, thus eliminating any NMR signal. Axial stress was applied through a piston actuator controlled by an independent hydraulic pump. Tests were performed by initially applying 500 psi axial stress and rapidly increasing the confining stress to 4000 psi. Following this, we increased the axial stress to observe any changes that occurred as the differential stress (confining stress – axial stress) decreased. Because we were only able to obtain 4 horizontal core plugs specifically for NMR measurements (Table 3), we ran additional measurements on vertical core plugs that were later used for triaxial deformation and acoustic measurements. This allowed us to obtain the minimum value of 10 samples necessary to meet the success criterion for this subtask.

T_2 measurements were taken progressively throughout each test. We used a standard Carr-Purcell-Meiboom-Gill (CPMG) echo sequence for T_2 measurements (Coates et al., 1999) with an inter-echo spacing of 0.106 ms. Each measurement was run until a signal-to-noise ratio of 100 was achieved. Incremental T_2 distributions, which are directly proportional to pore size distributions (Coates et al., 1999), are shown in Figs. 3-12.

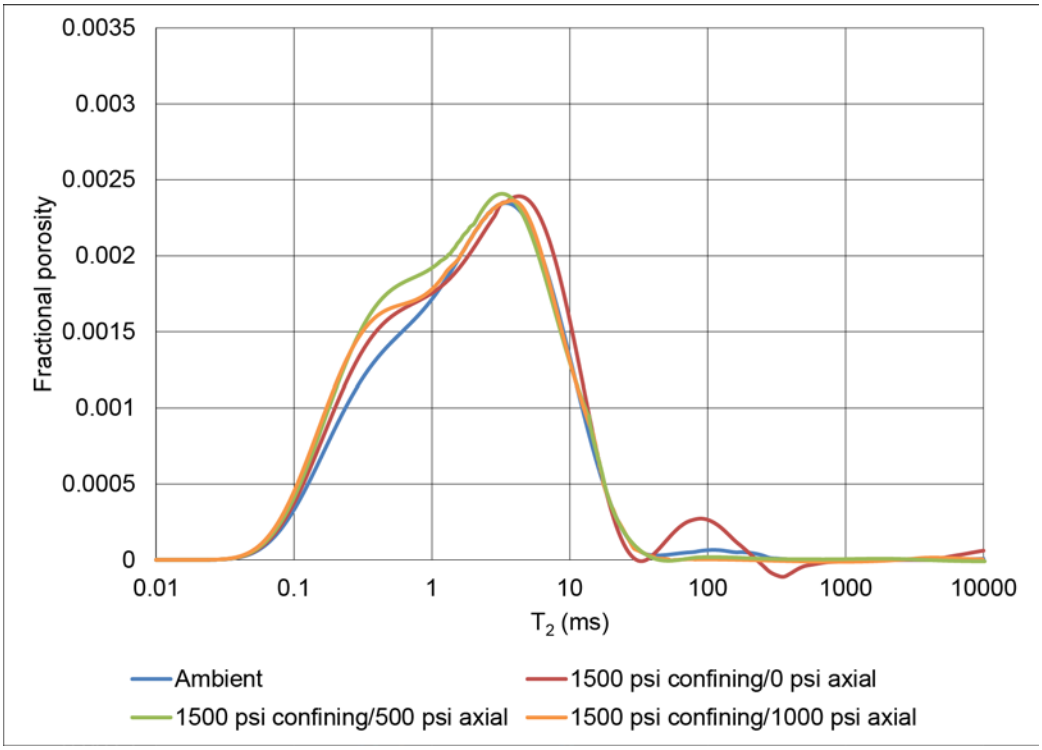

Figure 3. NMR data for Siliceous 3-14, horizontal sample.

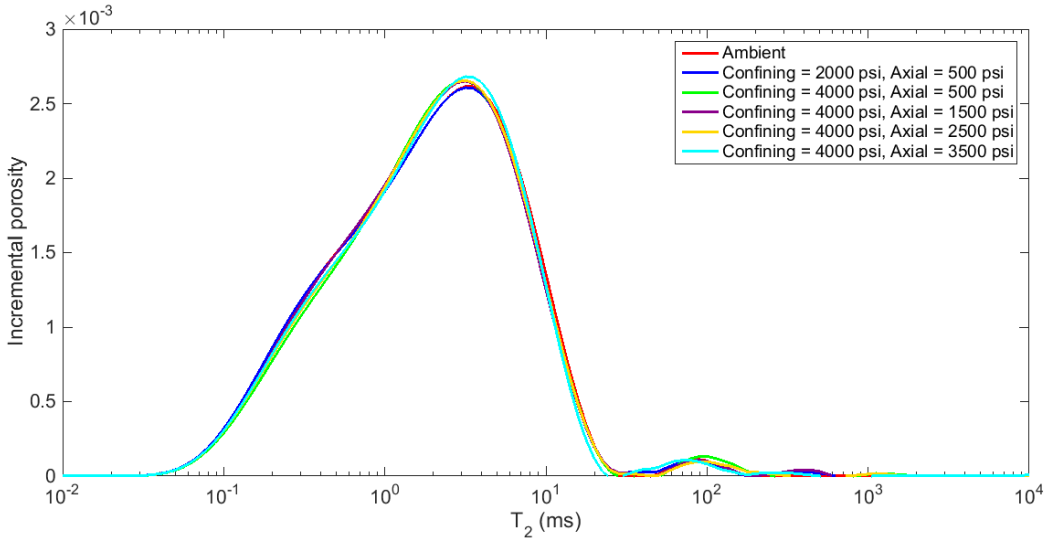

Figure 4. NMR data for Eagle Ford 2-50, horizontal sample.

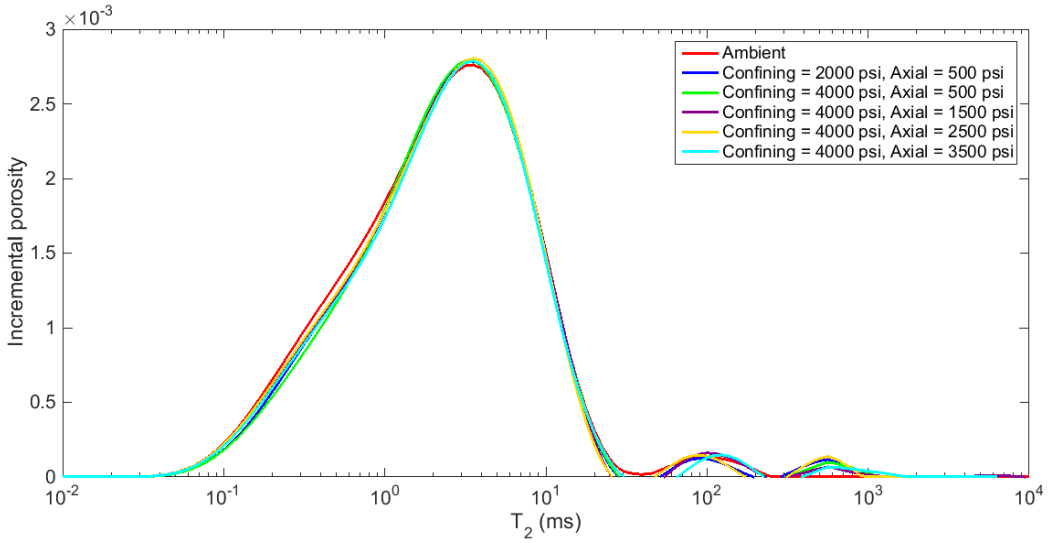

Figure 5. NMR data for Eagle Ford 2-50, horizontal sample (repeat).

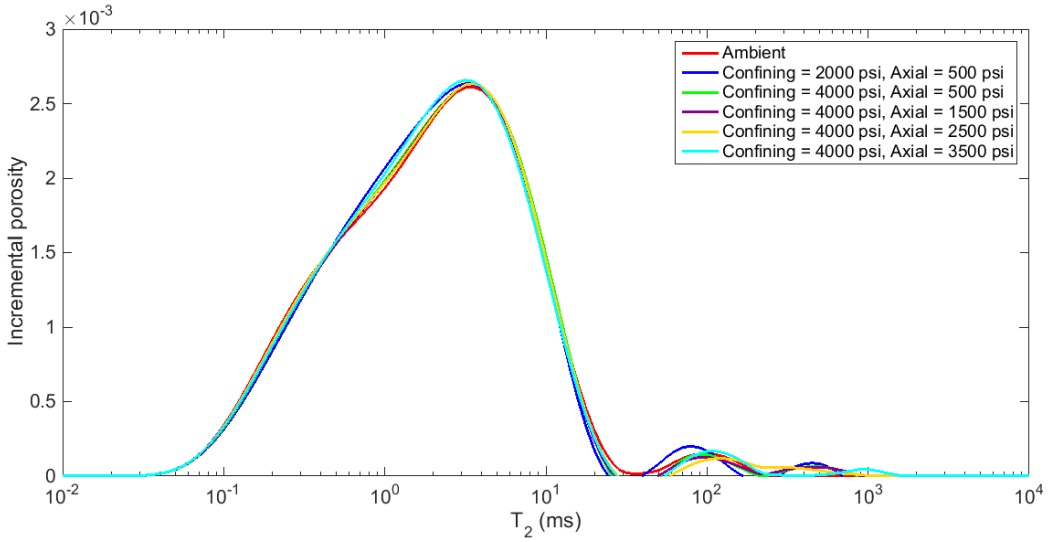

Figure 6. NMR data for Eagle Ford 2-50, vertical sample.

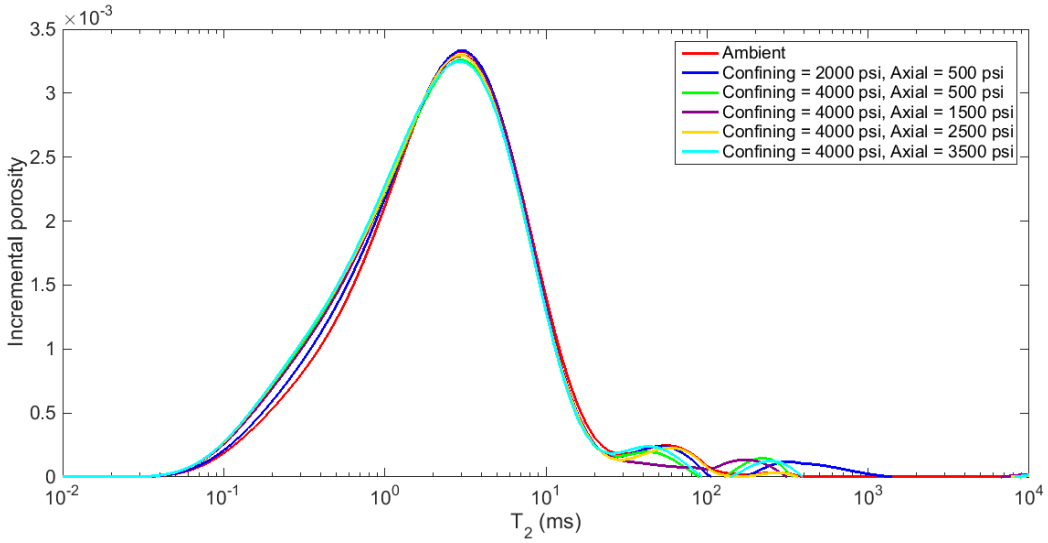

Figure 7. NMR data for Eagle Ford 2-93, horizontal sample.

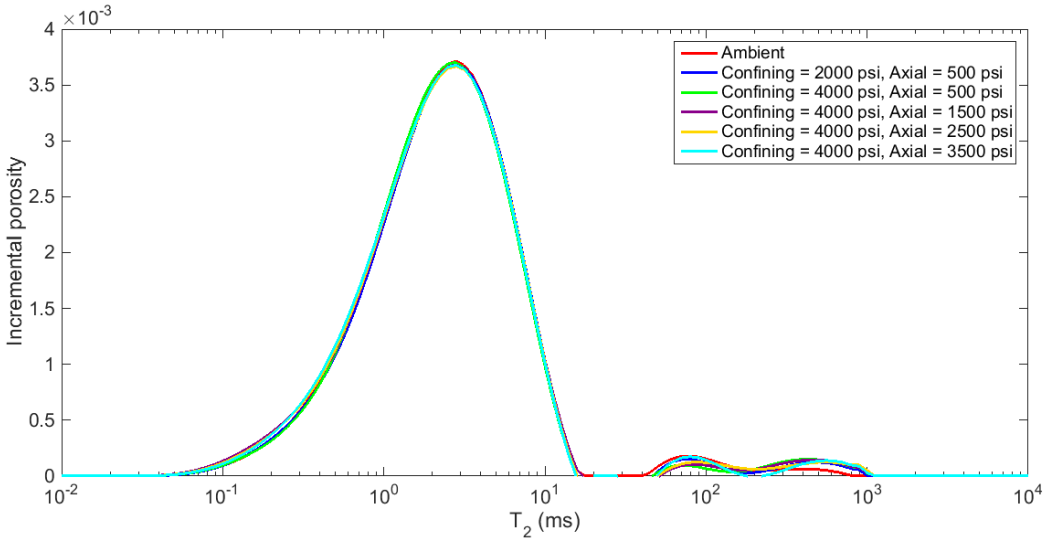

Figure 8. NMR data for Eagle Ford 2-93, horizontal sample (repeat).

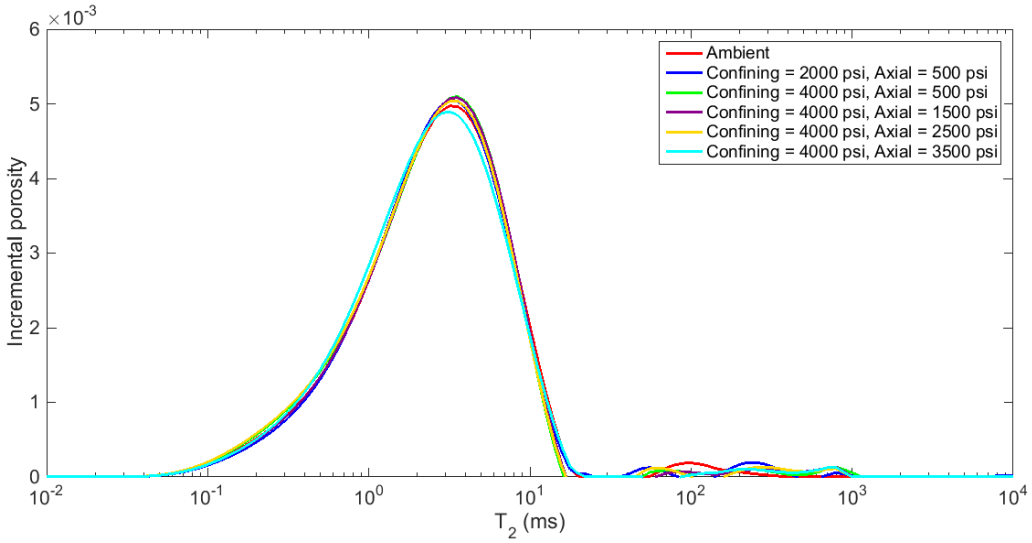

Figure 9. NMR data for Eagle Ford 2-93, horizontal sample 2.

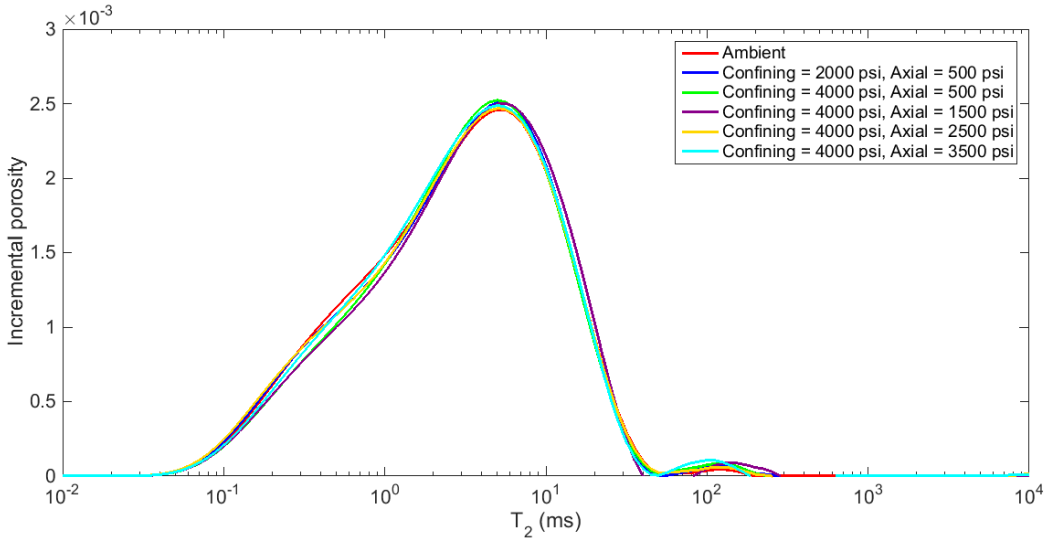

Figure 10. NMR data for Eagle Ford 1-223, horizontal sample.

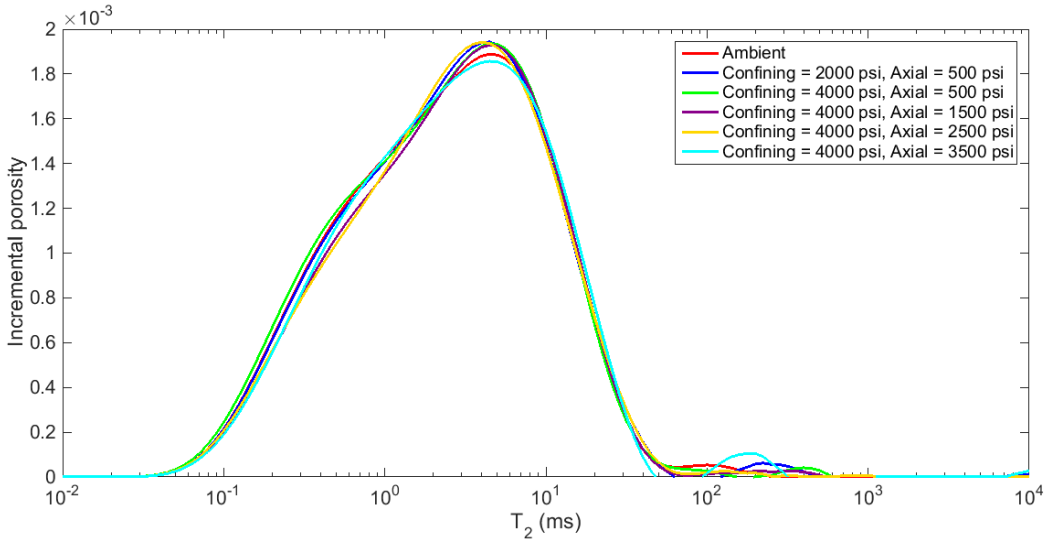

Figure 11. NMR data for Eagle Ford 1-223, horizontal sample (repeat).

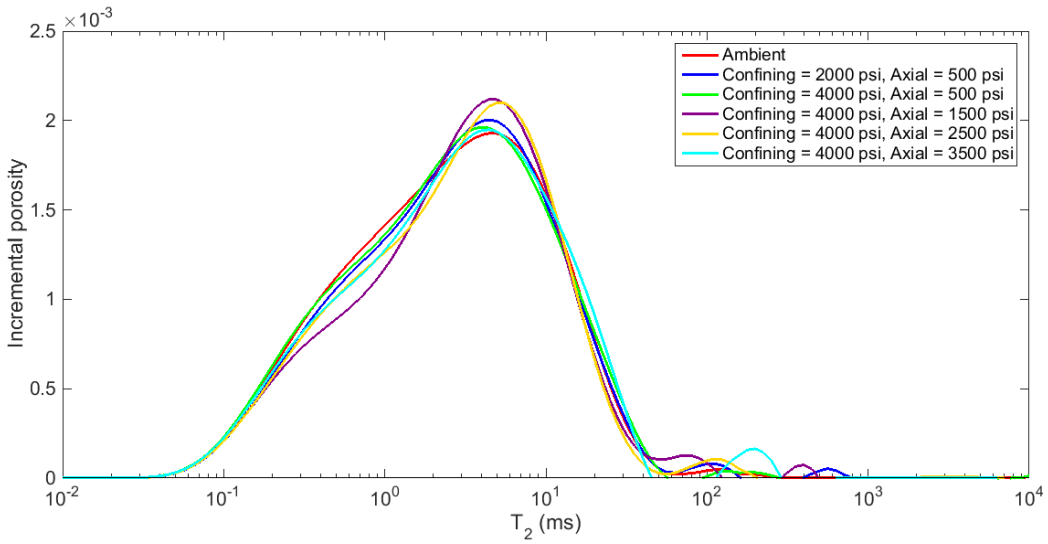

Figure 12. NMR data for Eagle Ford 1-223, vertical sample.

Many of the samples exhibited complex changes in porosity. Figs. 13 and 14 summarize the changes in porosity over the entire pore volume, as well as the change in porosity for T_2 values shorter than 1 ms. This T_2 range was where most of the changes in porosity were observed; it is believed that T_2 values in this range correspond to either clay-bound water or fluids residing in organic matter (Sondergeld et al., 2010b).

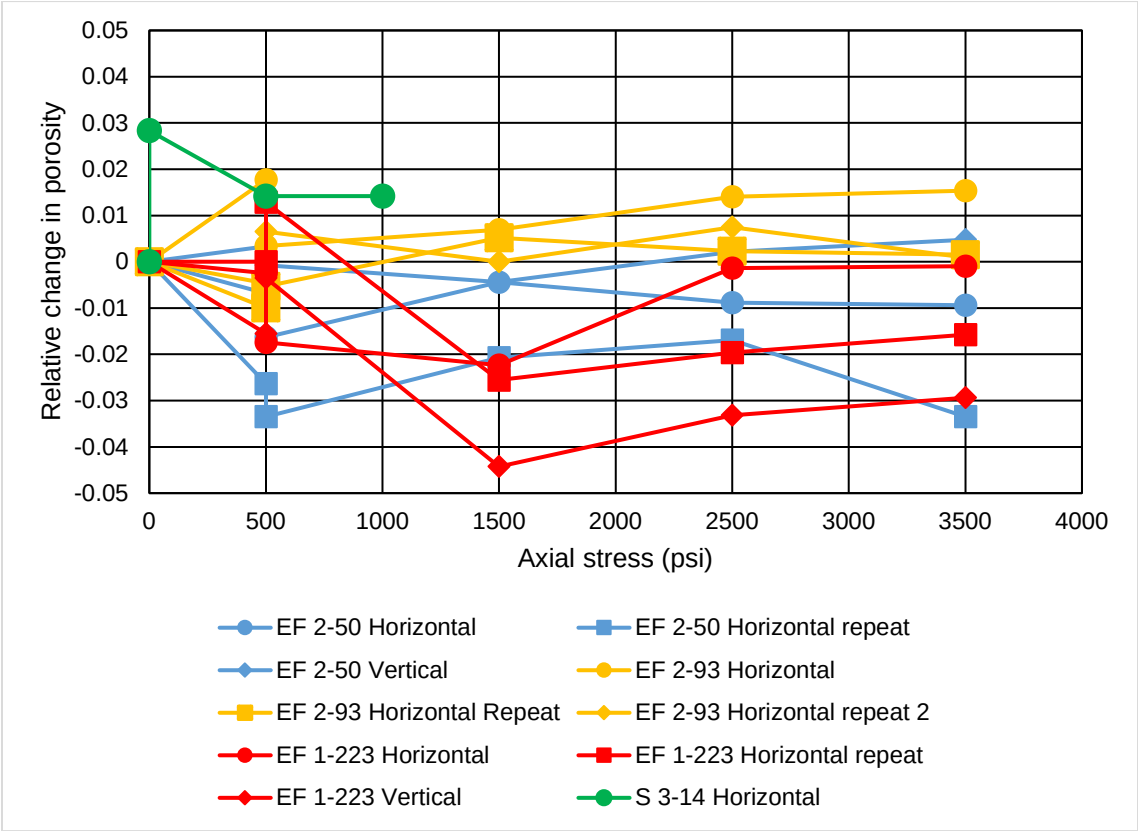

Figure 13. Relative change in total porosity with axial stress.

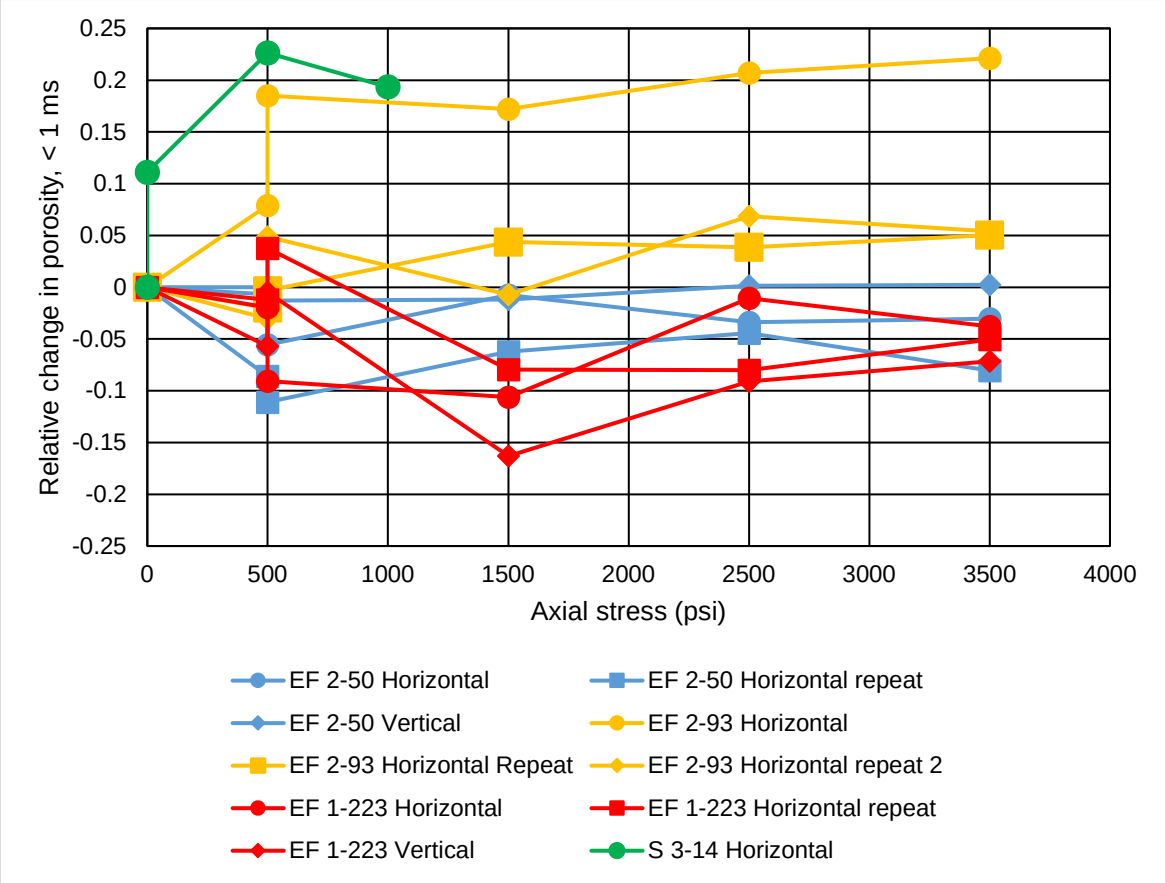

Figure 14. Relative change in porosity for T_2 < 1 ms with axial stress.

As seen in Fig. 13, most samples show a sharp reduction in porosity at an axial stress of 500 psi, corresponding to the rapid increase in confining stress as done in the experiment. However, many samples show progressively increasing porosity as axial stress increases. This is particularly apparent in Fig. 14, which shows the porosity change just for T_2 < 1 ms. The porosity in the smaller pores appears to be responding to deformation dilatantly. This can be corroborated with observations from gas adsorption and imaging.

3.4 Gas Adsorption/Desorption Measurements

Gas adsorption/desorption can determine quantitative pore size distribution and surface area by measuring volume of gas injected or produced during pressurization or depressurization of a sample. Typical gases used for this analysis include N_2, Kr, Ar, and CO_2. N_2 adsorption/desorption has been used successfully to characterize pores in clays and mudrocks as small as 1.7 nm, but the technique is ineffective in pores larger than ~0.3 µm (Kuila and Prasad, 2011; Schmitt et al., 2013). However, this technique provides a means of determining pore volumes associated with pores below the detection limit of NMR or SEM imaging.

Adsorption-desorption isotherms were measured at 77 K for N_2 and 273 K for CO_2 using a Micromeritics 3Flex system following the procedure outlined in Daigle (2014) and Jiang et al.

(2015). Samples were oven dried at 105 °C for 24 hours and hand crushed to < 3 mm size. Then, 0.5 and 1.5 g of crushed sample was placed in a sample tube and degassed under a N_2 stream at 220 °C for an additional 8 hours to remove any volatile fluids. Sample tubes were weighed after degassing and then attached to the instrument manifold. For N_2 sorption measurements, the sample tubes were immersed in liquid N_2 and evacuated. For CO_2 sorption measurements, the sample tubes were immersed in a water ice bath and evacuated. Adsorption proceeded in prescribed volume increments of gas dosing up to a pressure of approximately 1 atm; desorption then preceded by withdrawal of gas in prescribed volume increments. Desorption isotherms were not measured for CO_2 because the micropores probed using CO_2 adsorption are smaller than the capillary critical pore size, which is the pore size below which a vapor and liquid phase cannot coexist at equilibrium within the pores (Ravikovitch et al., 1995; Ravikovitch and Neimark, 2002). Data are presented as volume of gas adsorbed per unit mass of dried sample, corrected to standard temperature and pressure. Pressure is reported as P/P_0, which is pressure normalized with respect to saturation vapor pressure (1 atm for N_2 at 77 K; 34.5 atm for CO_2 at 273 K).

The pressure at which gas condenses in a pore is proportional to the pore size. Therefore, adsorption isotherms may be used to determine pore size distributions. In rocks such as shales that contain micropores or small mesopores (i.e., pores smaller than about 7 nm in width; Lastoskie et al., 1993), pores are small enough that adsorbed layers on opposite walls of the pore interact with each other and with solid material on the opposite pore walls. The relationship between pore size and condensation pressure is therefore determined by considering the chemical potential among all adsorbed molecules and all solid surfaces. From statistical mechanics, the measured isotherm $N(P)$ may be determined by

$$N(P) = \int_{r_{\min}}^{r_{\max}} N(P,r) f(r) dr , \qquad \text{(Eq. 1)}$$

where $N(P,r)$ is the theoretical isotherm kernel of adsorbate in a pore of radius r at pressure P (Roque-Malherbe, 2007), and $f(r)$ is the pore size distribution (Lastoskie et al., 1993). The isotherm kernels $N(P,r)$ may be determined from nonlocal density functional theory (NLDFT) by considering fluid-fluid and solid-fluid interaction potentials and minimizing the grand potential function within a pore (Ravikovitch and Neimark, 2002). The pore size distribution may then be determined iteratively by finding $f(r)$ in (2) that best matches the measured isotherm. Various models for pore size determination by NLDFT have been developed based on different combinations of solids and fluids in various idealized pore geometries. We used a version of NLDFT developed for adsorption in slit-shaped pores in a carbon substrate (Tarazona, 1985a,b).

Results for N_2 adsorption/desorption are shown in Figs. 15-29.

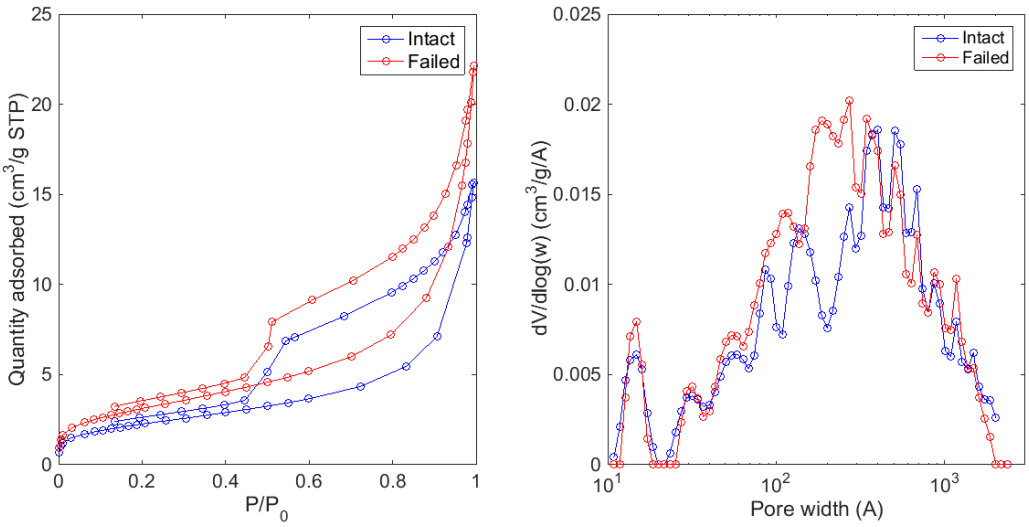

Figure 15. N_2 adsorption/desorption results for Siliceous 3-14, horizontal sample.

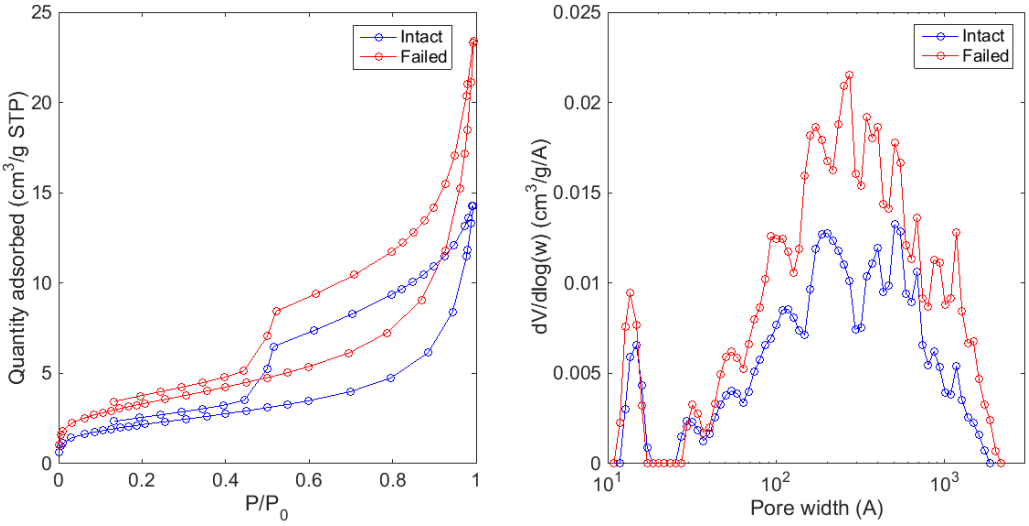

Figure 16. N_2 adsorption/desorption results for Siliceous 3-14, vertical sample.

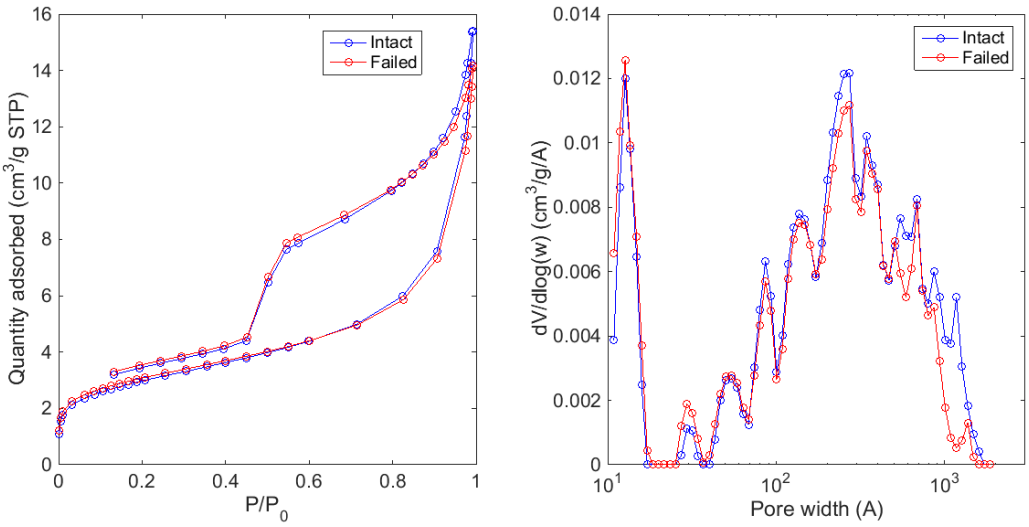

Figure 17. N_2 adsorption/desorption results for Siliceous 3-42, horizontal sample.

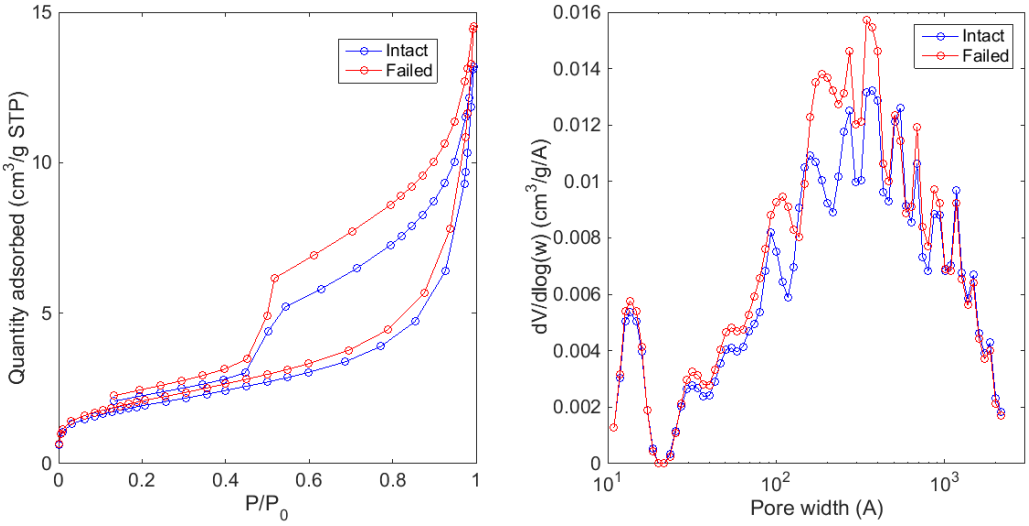

Figure 18. N_2 adsorption/desorption results for Siliceous 3-53, horizontal sample.

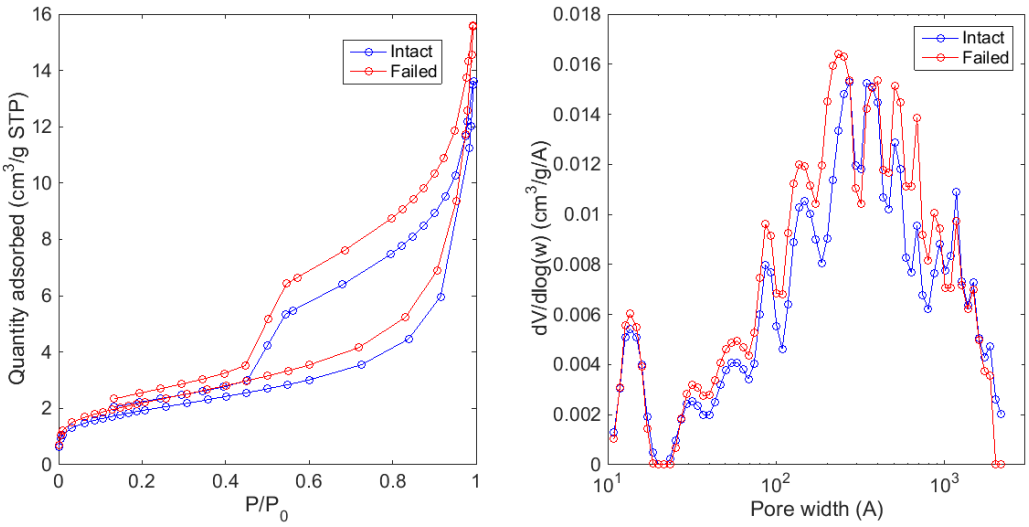

Figure 19. N_2 adsorption/desorption results for Siliceous 3-53, vertical sample.

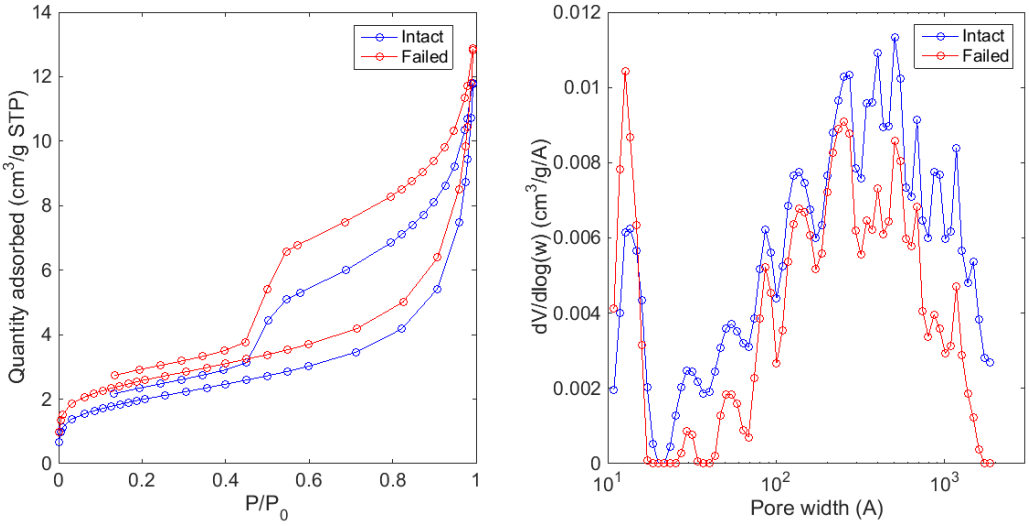

Figure 20. N_2 adsorption/desorption results for Siliceous 4-14, horizontal sample.

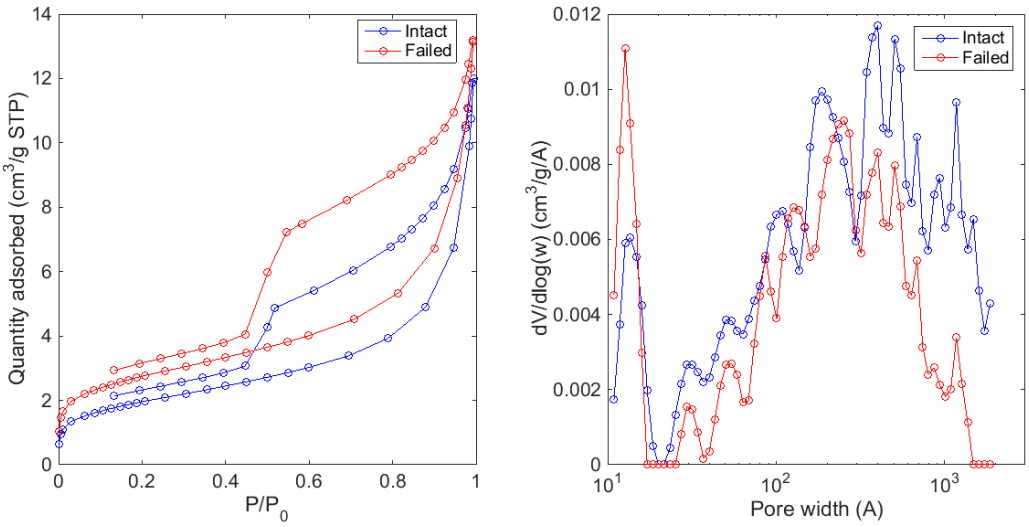

Figure 21. N_2 adsorption/desorption results for Siliceous 4-14, horizontal sample, repeat measurement.

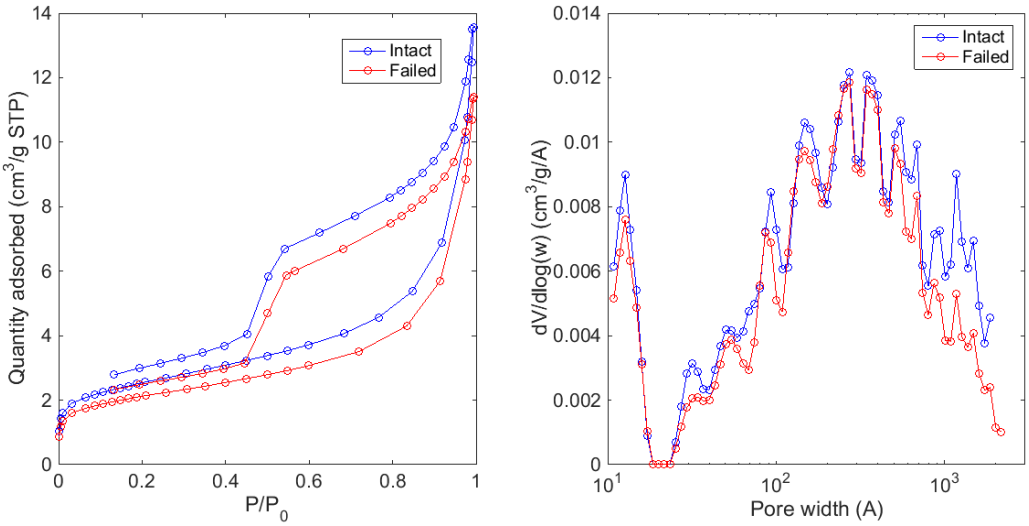

Figure 22. N_2 adsorption/desorption results for Siliceous 4-34, horizontal sample.

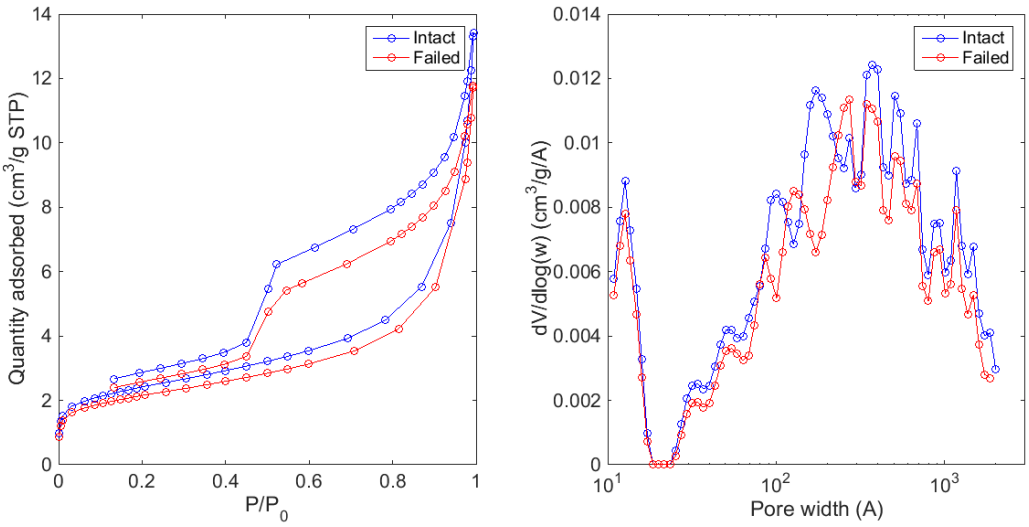

Figure 23. N_2 adsorption/desorption results for Siliceous 4-34, horizontal sample, repeat measurement.

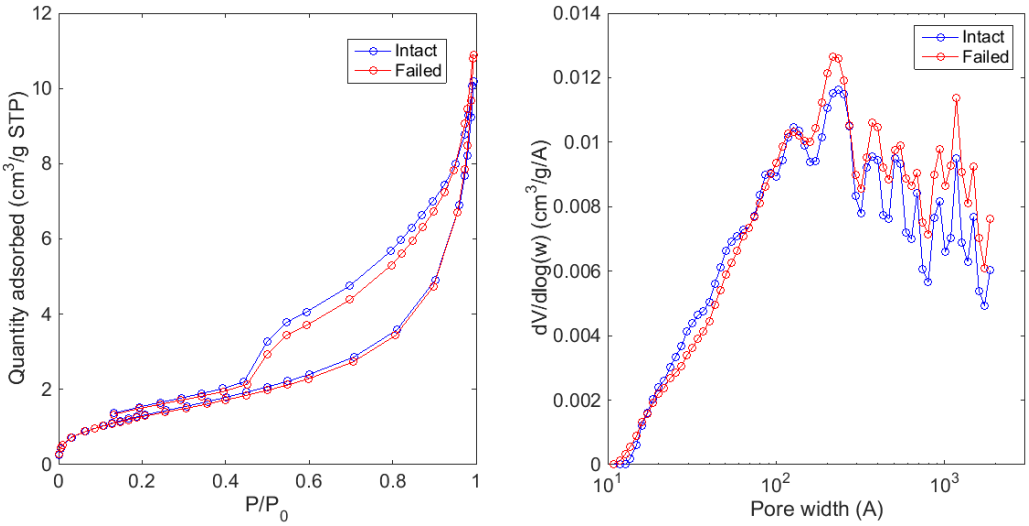

Figure 24. N_2 adsorption/desorption results for Eagle Ford 1-223, horizontal sample.

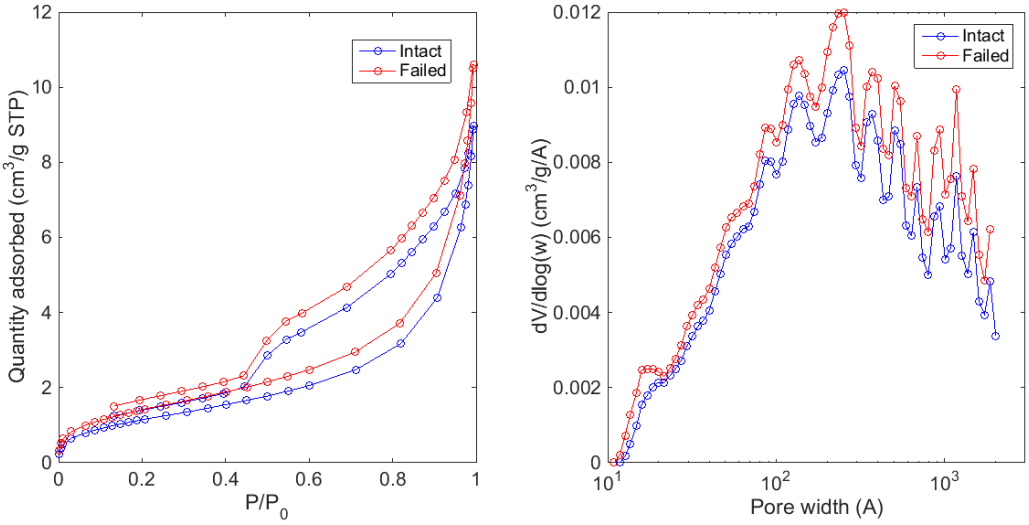

Figure 25. N_2 adsorption/desorption results for Eagle Ford 1-223, vertical sample.

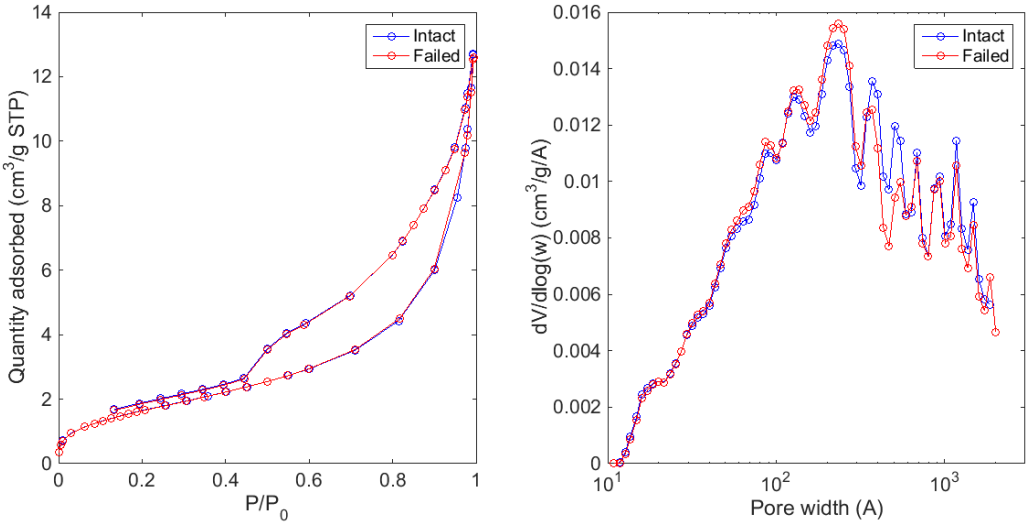

Figure 26. N_2 adsorption/desorption results for Eagle Ford 2-50, horizontal sample.

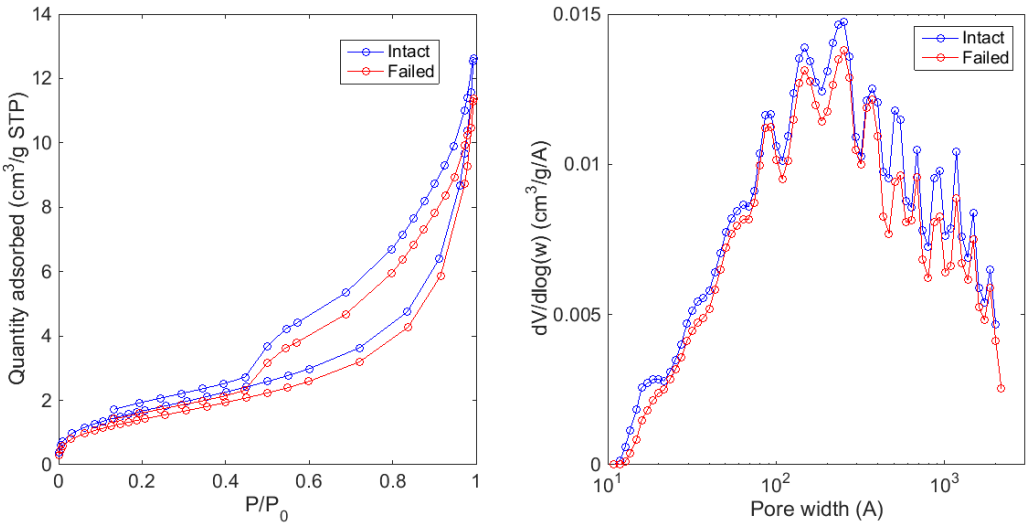

Figure 27. N_2 adsorption/desorption results for Eagle Ford 2-50, vertical sample.

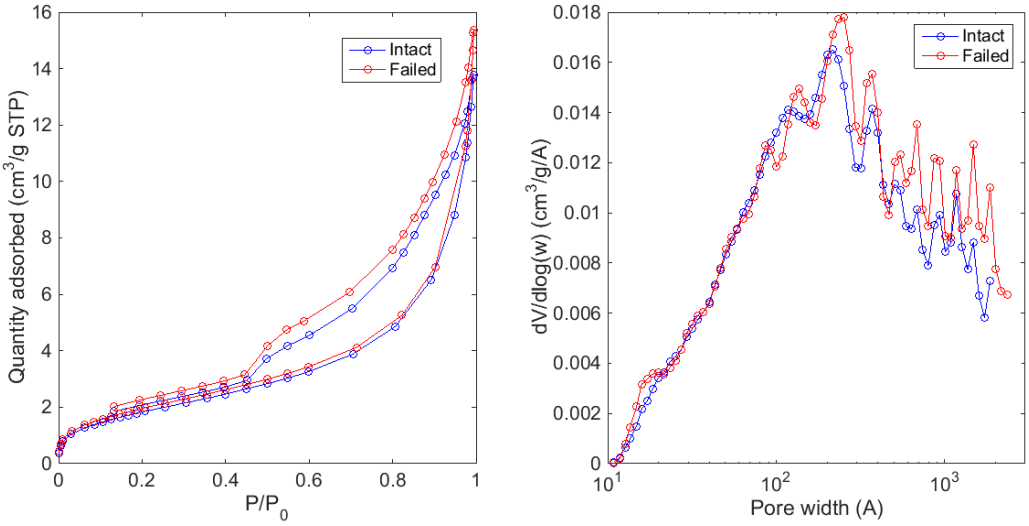

Figure 28. N_2 adsorption/desorption results for Eagle Ford 2-93, horizontal sample.

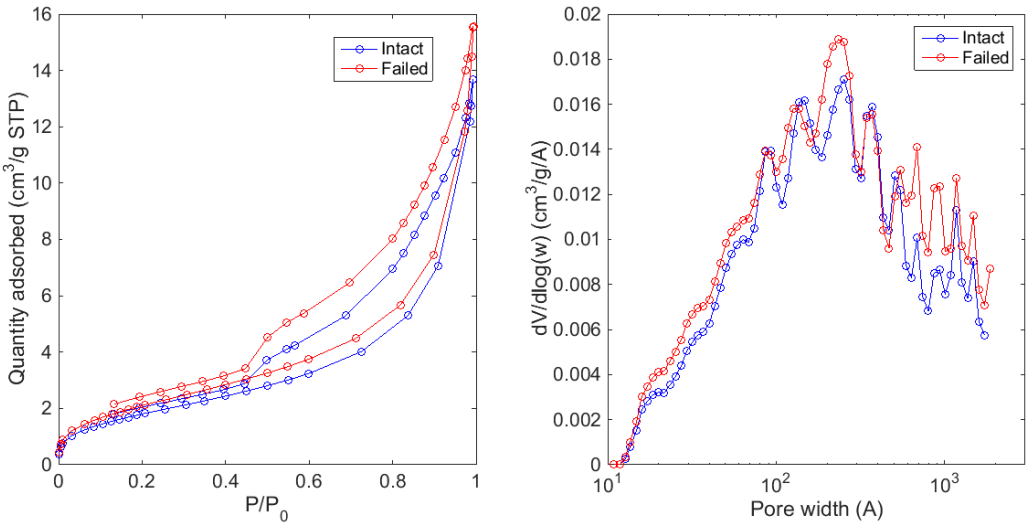

Figure 29. N_2 adsorption/desorption results for Eagle Ford 2-93, vertical sample.

In general, the maximum adsorbed amounts in the failed samples are greater than those in the intact samples. This is summarized in Fig. 30, which shows the average mesopore pore volume from N_2 adsorption in intact and failed samples. Mesopore volume is taken as the volume in pores larger than 2 nm width.

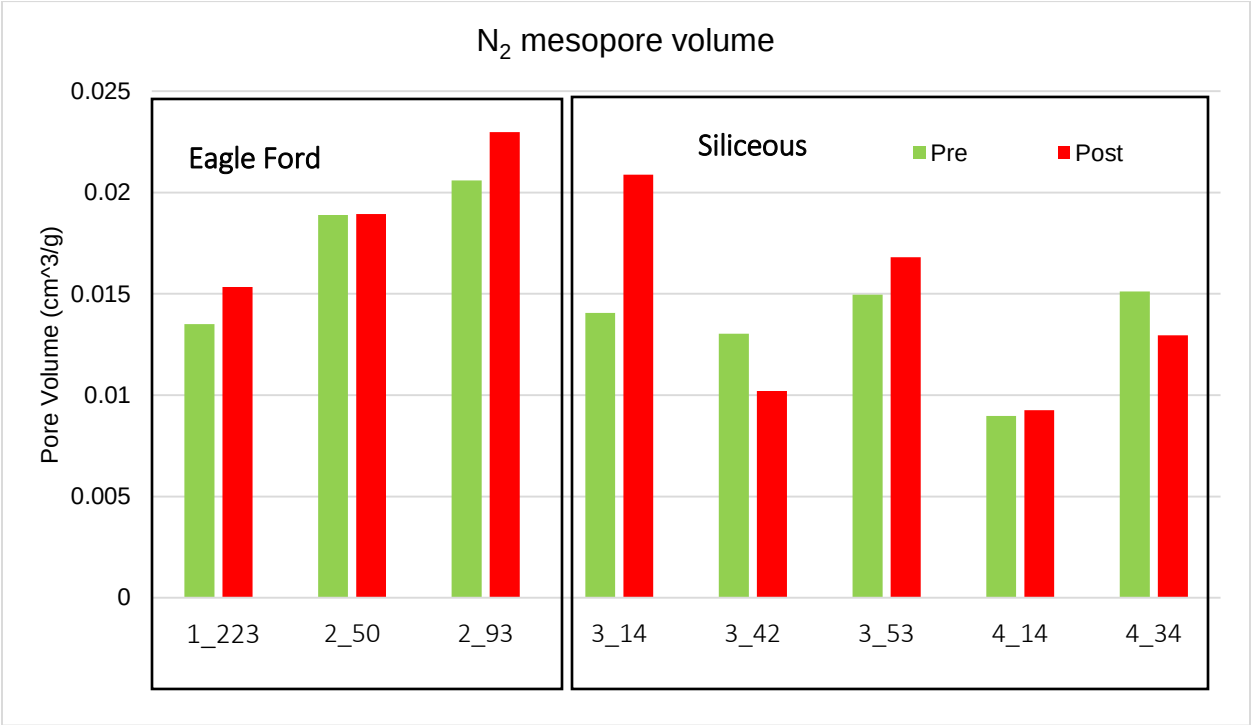

Figure 30. Average mesopore volume in pre-failure (green) and post-failure (red) samples from N_2 adsorption.

Results for CO_2 adsorption are shown in Figs. 31-46.

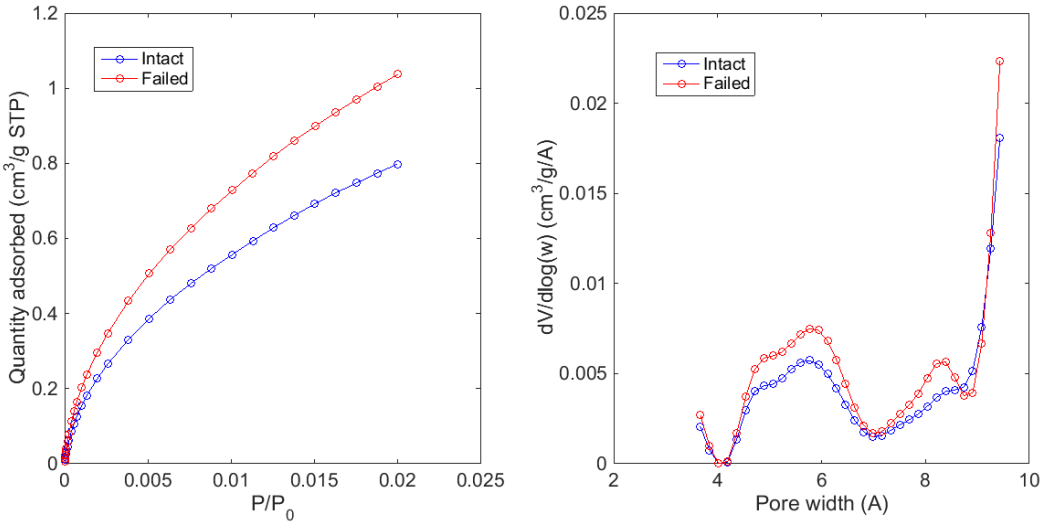

Figure 31. CO_2 adsorption results for Siliceous 3-14, horizontal sample.

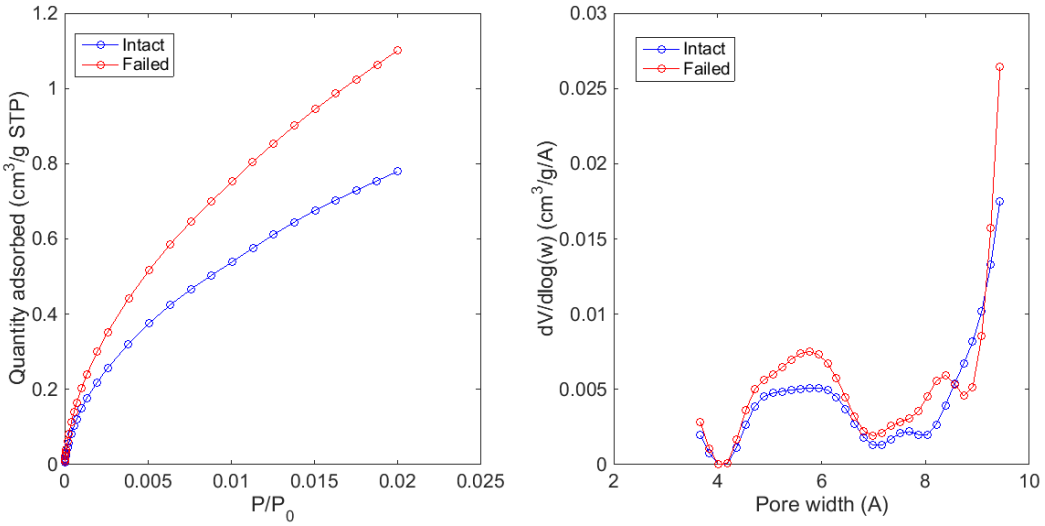

Figure 32. CO_2 adsorption results for Siliceous 3-14, vertical sample.

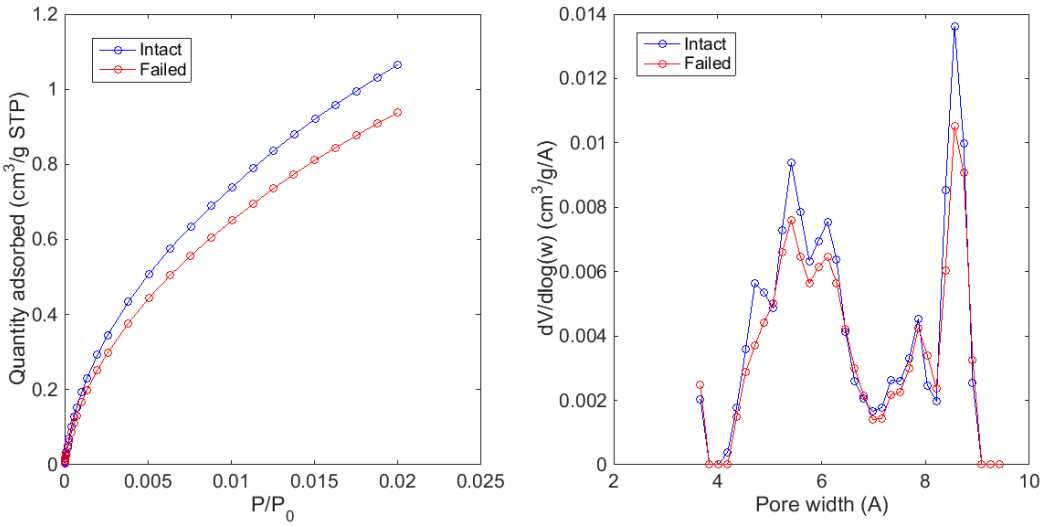

Figure 33. CO_2 adsorption results for Siliceous 3-42, horizontal sample.

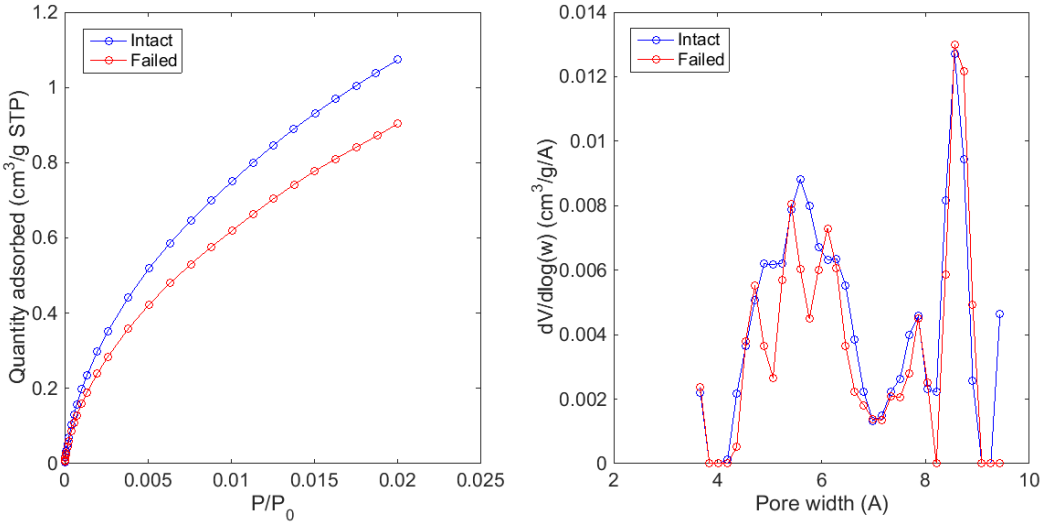

Figure 34. CO_2 adsorption results for Siliceous 3-42, horizontal sample, repeat measurement.

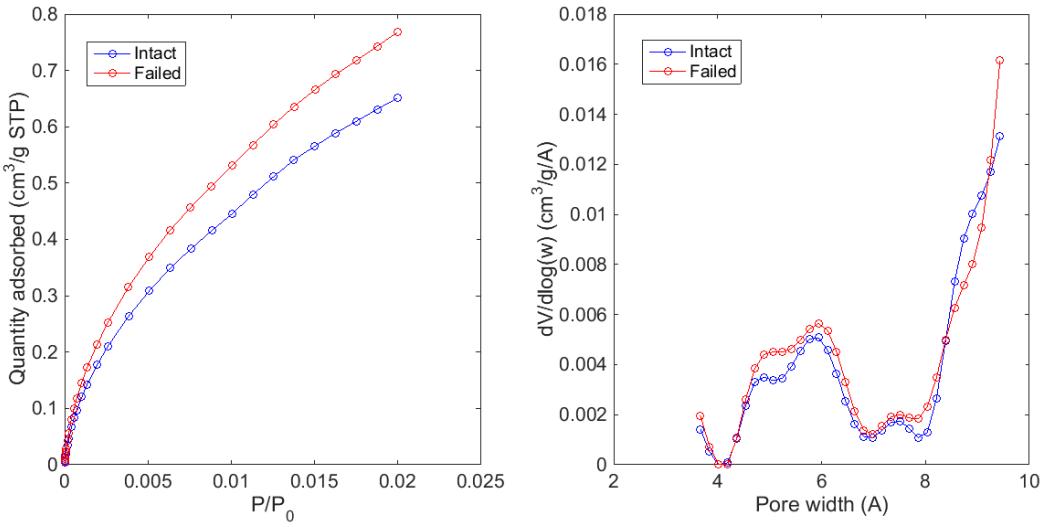

Figure 35. CO_2 adsorption results for Siliceous 3-53, horizontal sample.

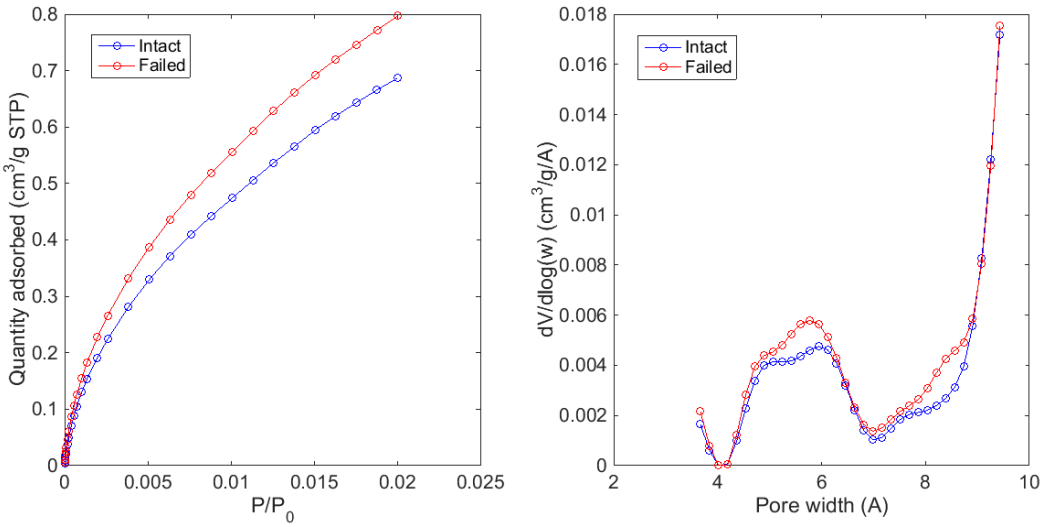

Figure 36. CO_2 adsorption results for Siliceous 3-53, vertical sample.

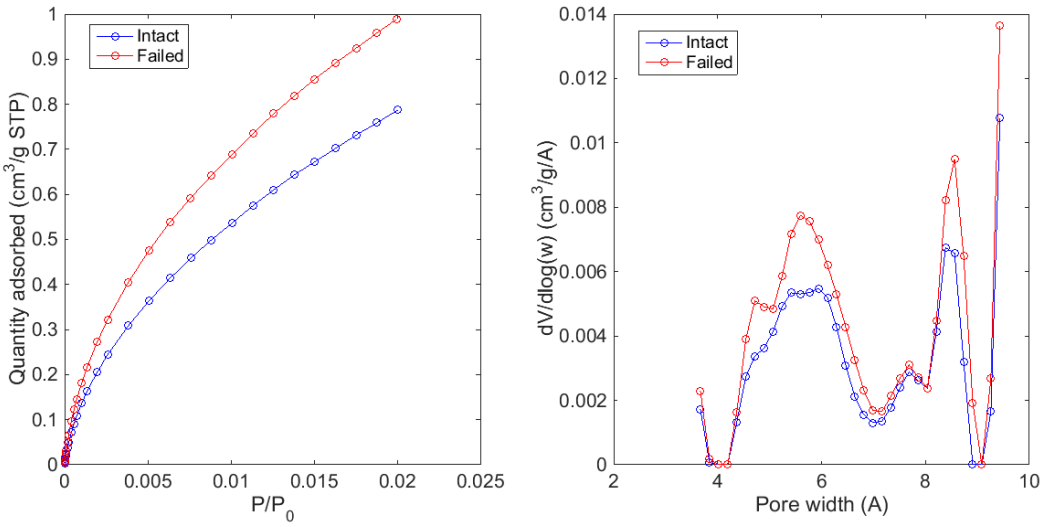

Figure 37. CO_2 adsorption results for Siliceous 4-14, horizontal sample.

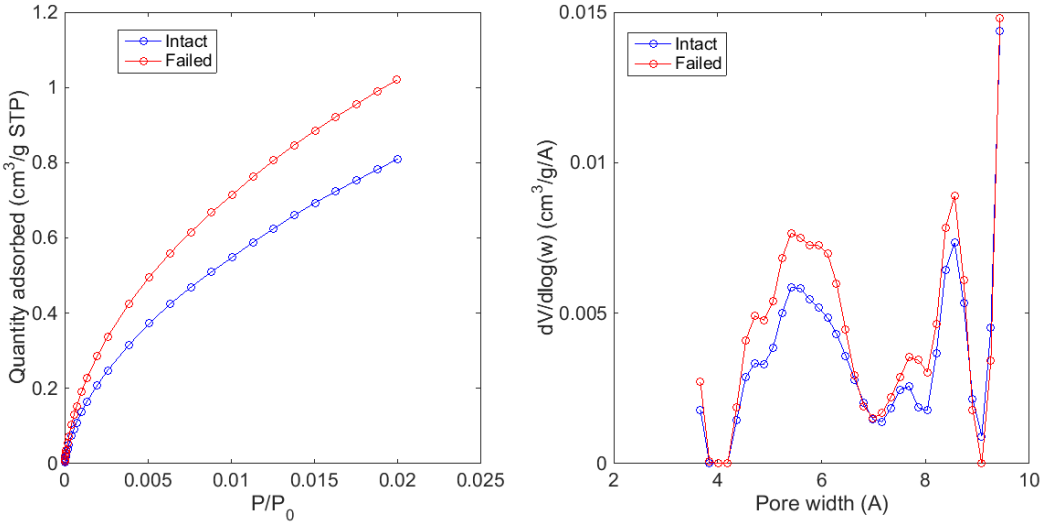

Figure 38. CO_2 adsorption results for Siliceous 4-14, horizontal sample, repeat measurement.

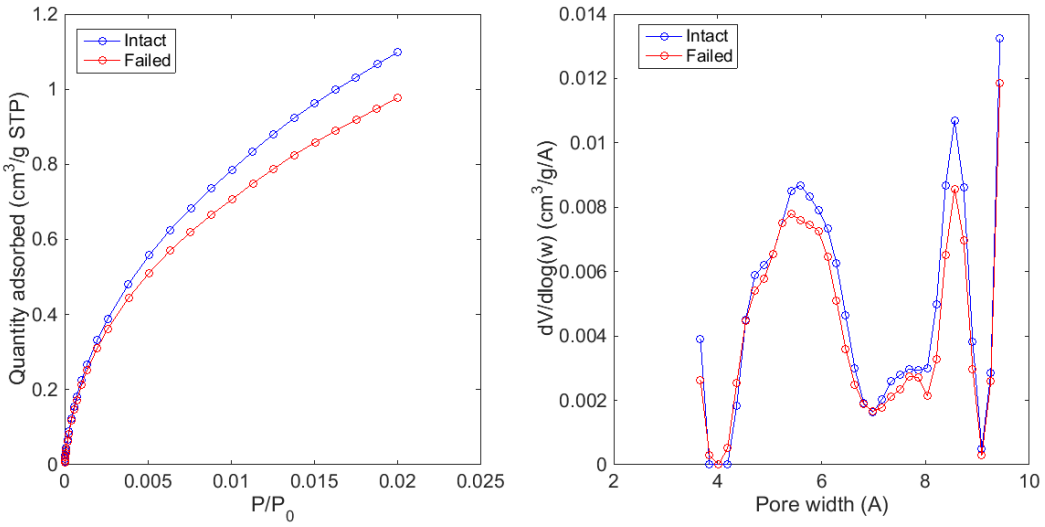

Figure 39. CO_2 adsorption results for Siliceous 4-34, horizontal sample.

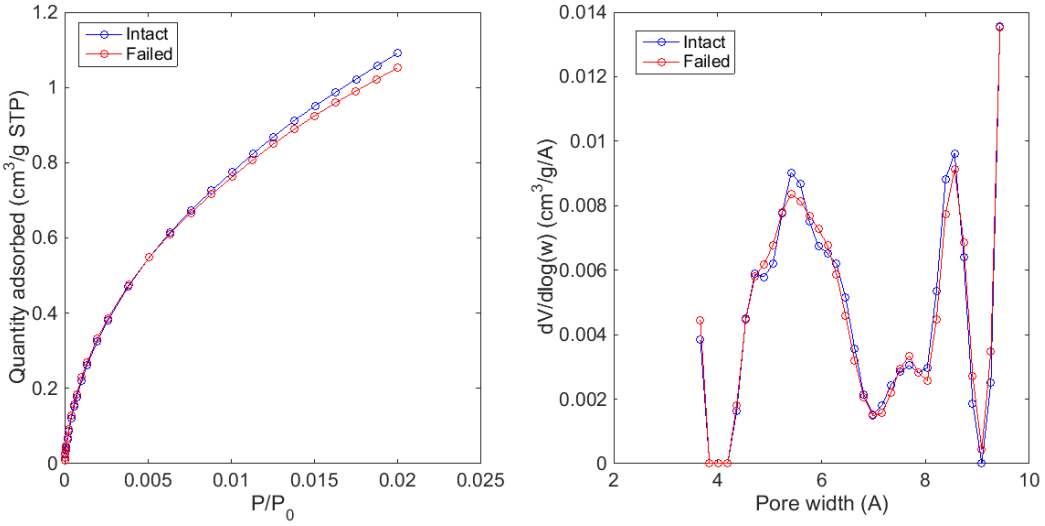

Figure 40. CO_2 adsorption results for Siliceous 4-34, horizontal sample, repeat measurement.

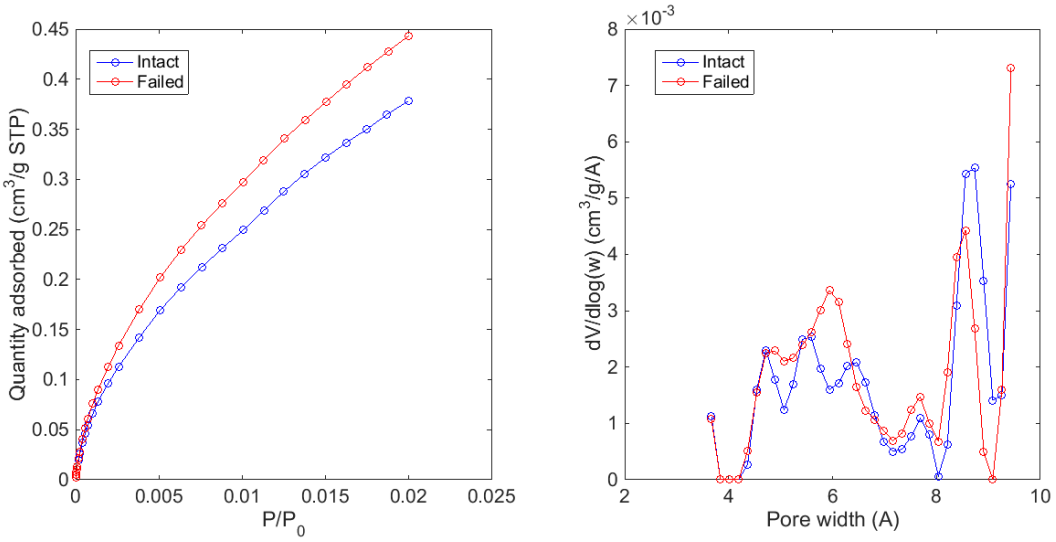

Figure 41. CO_2 adsorption results for Eagle Ford 1-223, horizontal sample.

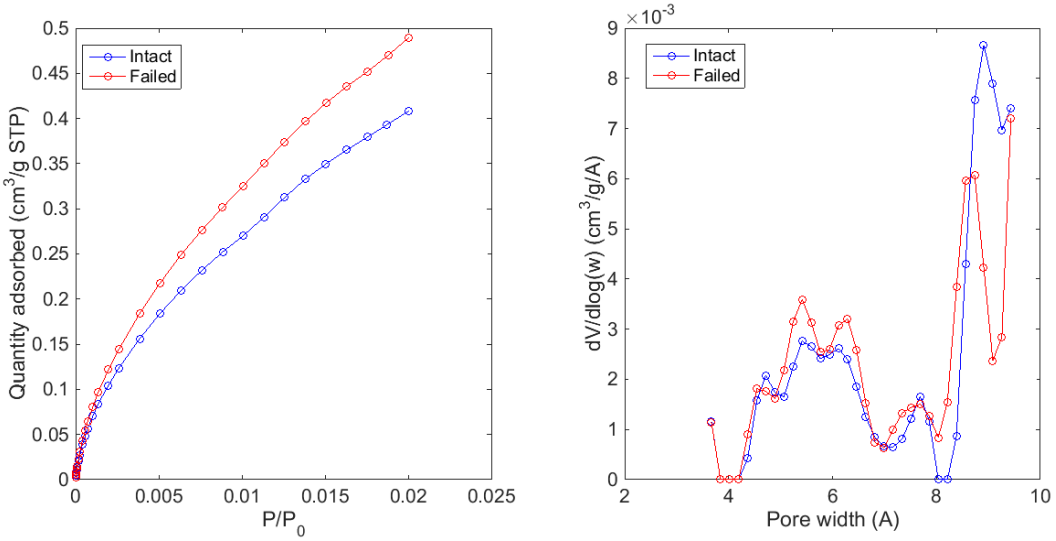

Figure 42. CO_2 adsorption results for Eagle Ford 1-223, vertical sample.

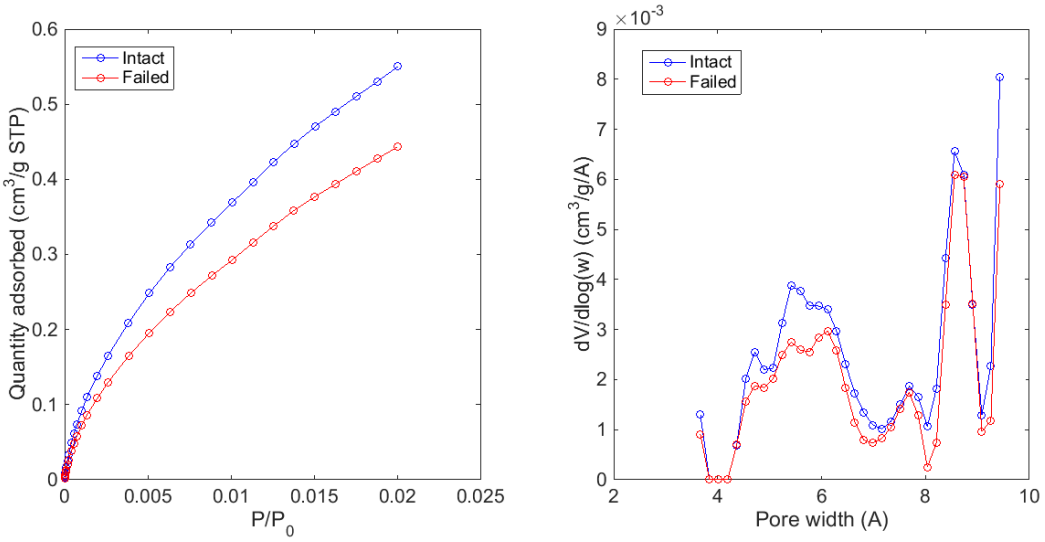

Figure 43. CO_2 adsorption results for Eagle Ford 2-50, horizontal sample.

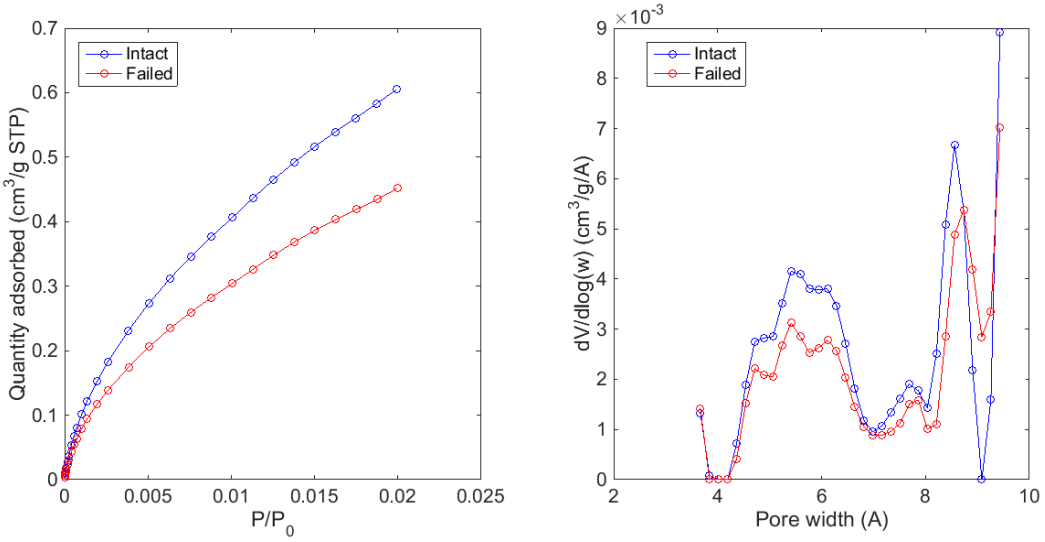

Figure 44. CO_2 adsorption results for Eagle Ford 2-50, vertical sample.

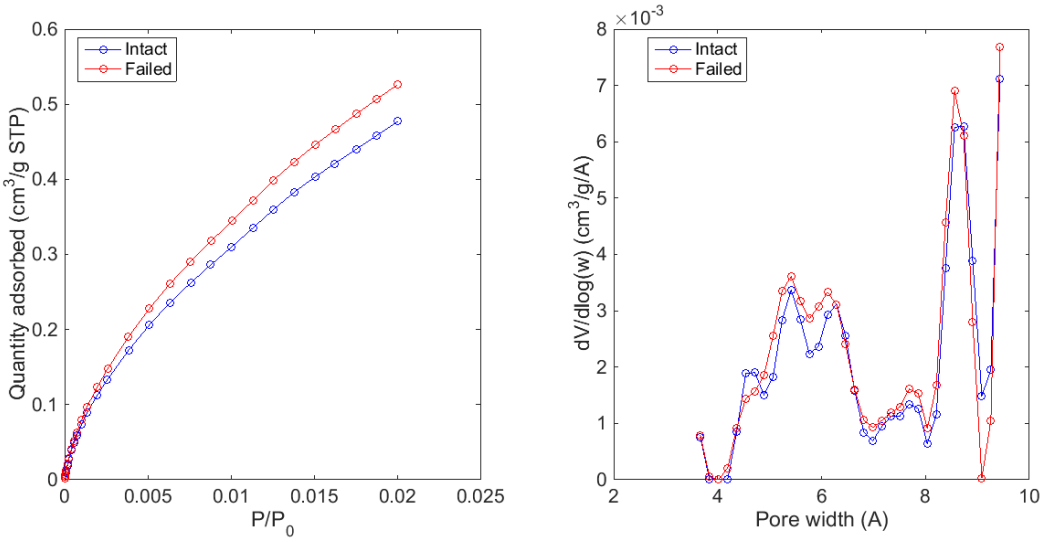

Figure 45. CO_2 adsorption results for Eagle Ford 2-93, horizontal sample.

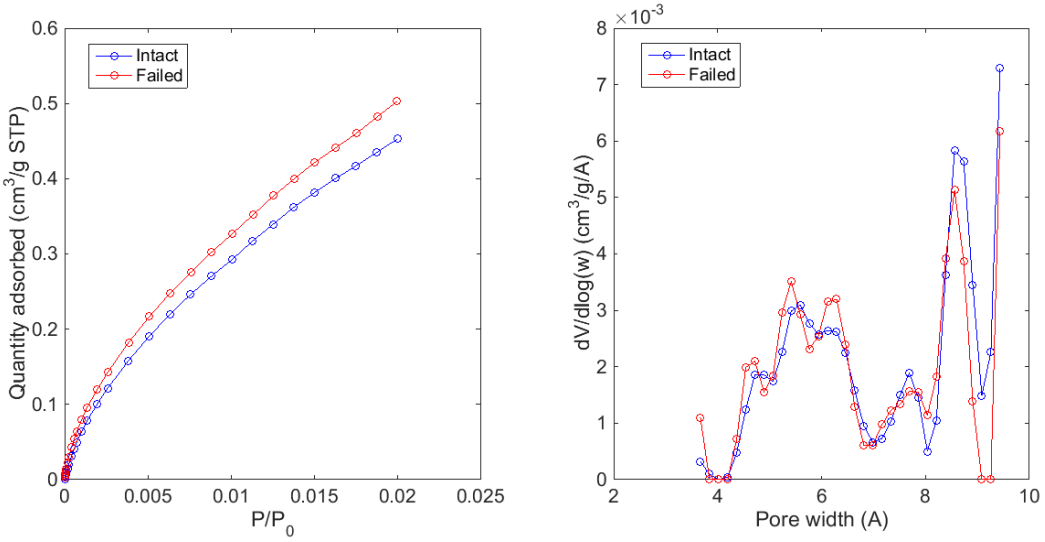

Figure 46. CO_2 adsorption results for Eagle Ford 2-93, vertical sample.

As was the case with N_2 adsorption, the amount of CO_2 adsorbed generally increased in the failed samples relative to the intact samples. Fig. 47 shows a comparison of average micropore volumes determined from CO2 adsorption. Micropores refer to pores smaller than 2 nm in width (Sing et al., 1985).

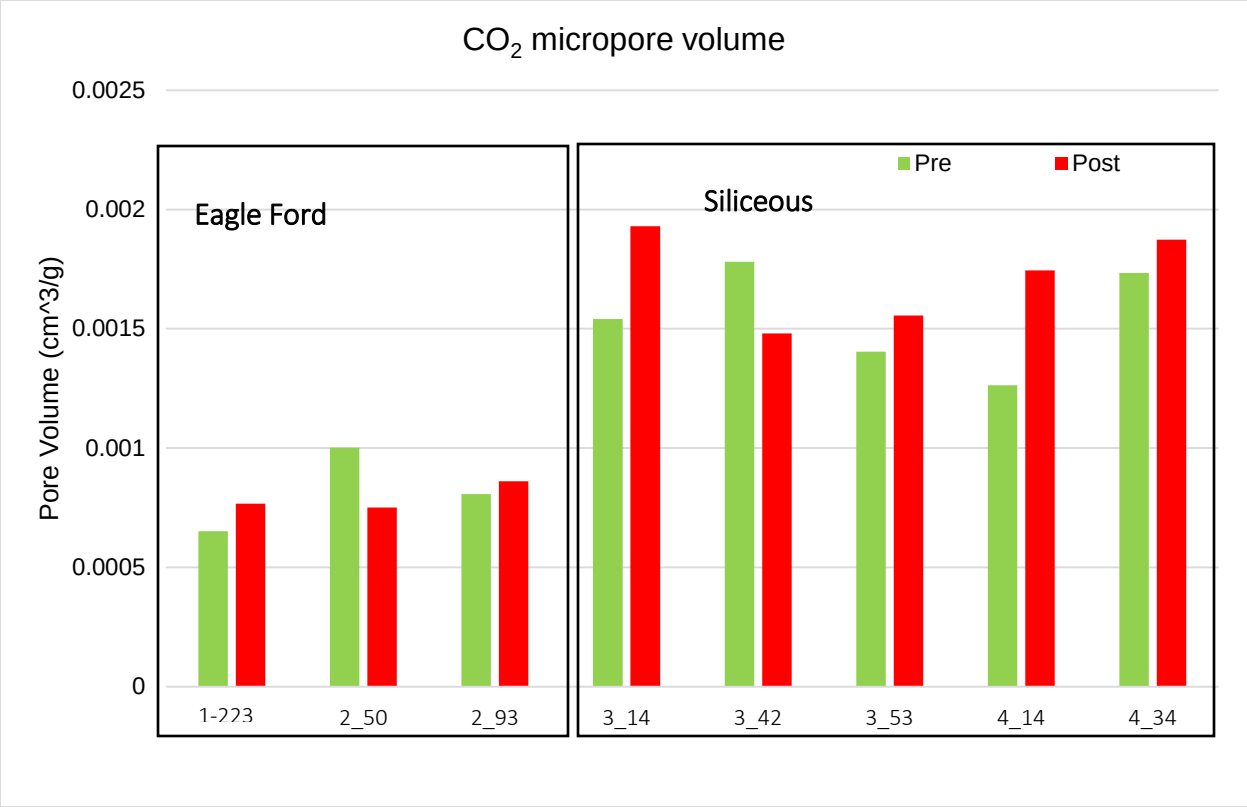

Figure 47. Average micropore volumes from CO_2 adsorption for pre-failure (green) and post-failure (red) samples.

3.5 Acoustic Measurements

To help constrain the elastic wave response during deformation leading up to failure, we measured acoustic velocities on samples during triaxial deformation. Samples were subjected to confined compressive strength testing using a GCTS triaxial testing apparatus equipped with compressional and shear velocity transducers. The samples were wrapped in a Viton sleeve and loaded into the testing cell, and strain gauges and acoustic transducers were attached (Fig. 48). The testing cell was then filled with hydraulic oil, which was used as the confining fluid. Axial stress was applied through a servo-controlled axial ram. During the test, the confining stress was increased to 10 MPa over the course of 1 minute, and then the axial stress was increased by displacing the axial ram at a rate of 0.01”/minute. Acoustic measurements were made every 30 seconds during the measurement. Measurements proceeded until failure occurred, defined as the point at which axial stress began decreasing with increasing axial displacement.

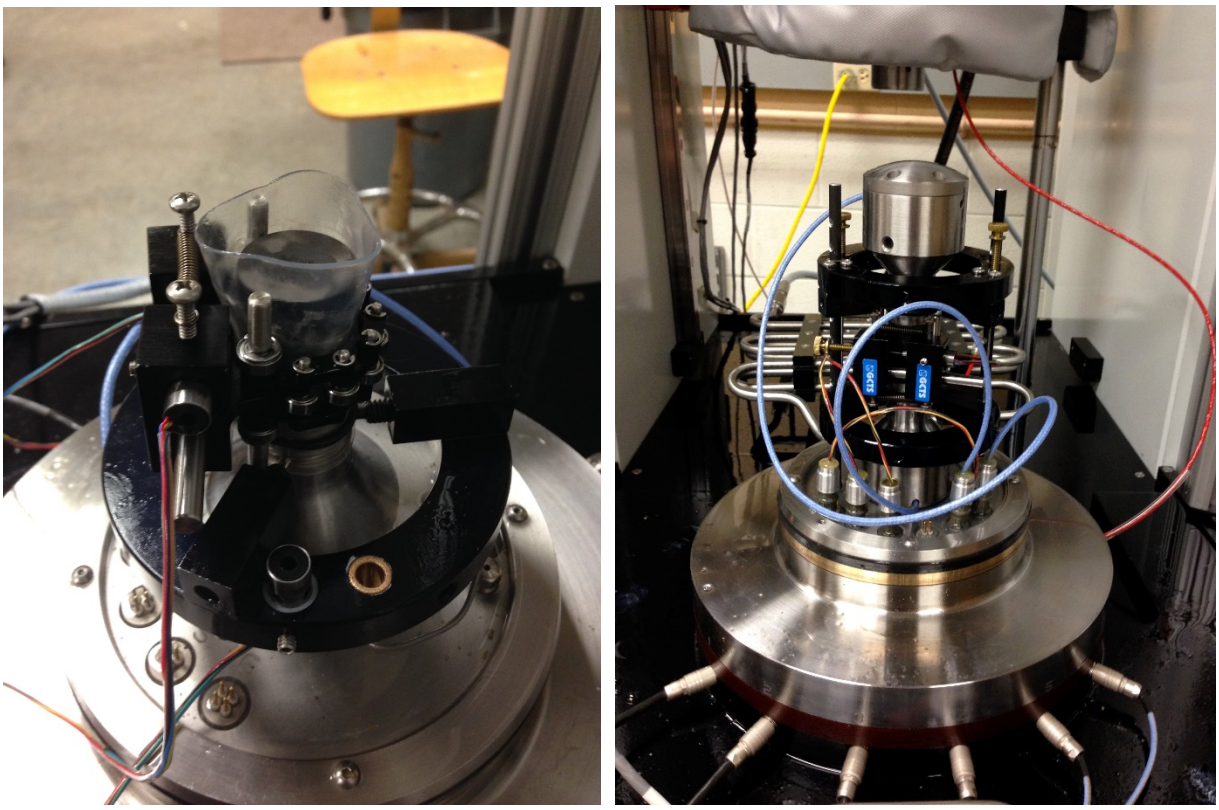

Figure 48. Photographs of apparatus used for triaxial deformation and acoustic measurements. Left: cylindrical shale sample encased in Viton sleeve with strain gauges and acoustic transducers. Shale sample is 1” in diameter. Right: Sample being loaded into the load cell.

We obtained good-quality stress-strain data from the triaxial deformation for 8 samples, which are presented in Fig. 49.

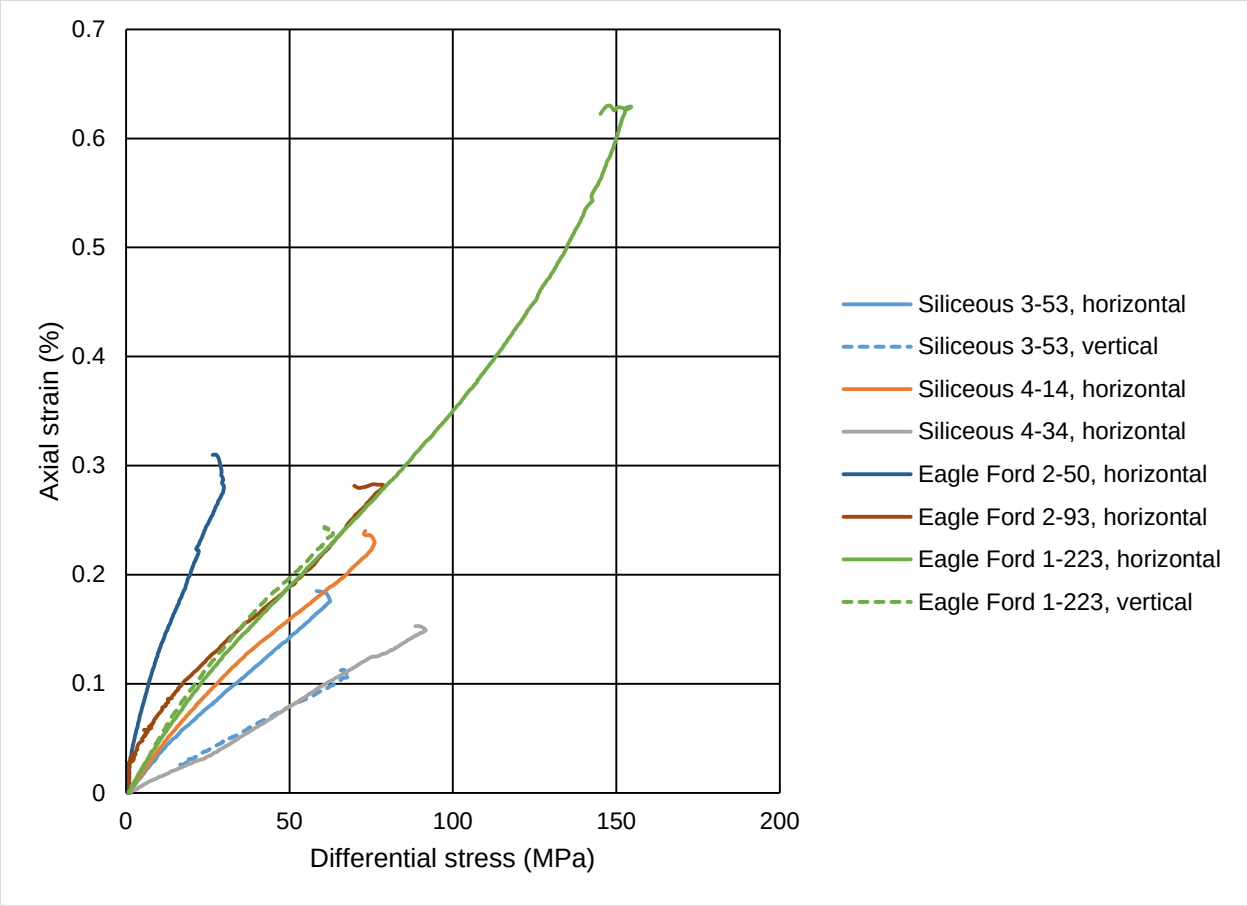

Figure 49. Stress-strain data for 8 samples. Differential stress is computed as axial stress – confining stress.

3.6 Geophysical Modeling

3.6.1 Image Segmentation and Waveform Simulations

Prior to simulating the elastic wavefield through a high-resolution image, we must assign elastic properties (P- and S-wave velocities and density) to each pixel. Accordingly, the RGB and/or grayscale images must be segmented to identify the major solid constituents and pores. This segmentation process is non-trivial, even when using the color and grayscale images. The four images in Figure 50 have slightly different outlined areas to avoid the scale and color indicators that are embedded in the image. The approach taken uses the grayscale image (a) to define boundaries and edges as a binary image (b). The color image (c) is constructed from the summation of 10 images of individual elements. We elemental images and edge detection algorithms to scale each pixel to obtain the different color values for each mineral (d). With the minerals and pores identified by individual colors, the corresponding elastic properties can be assigned.

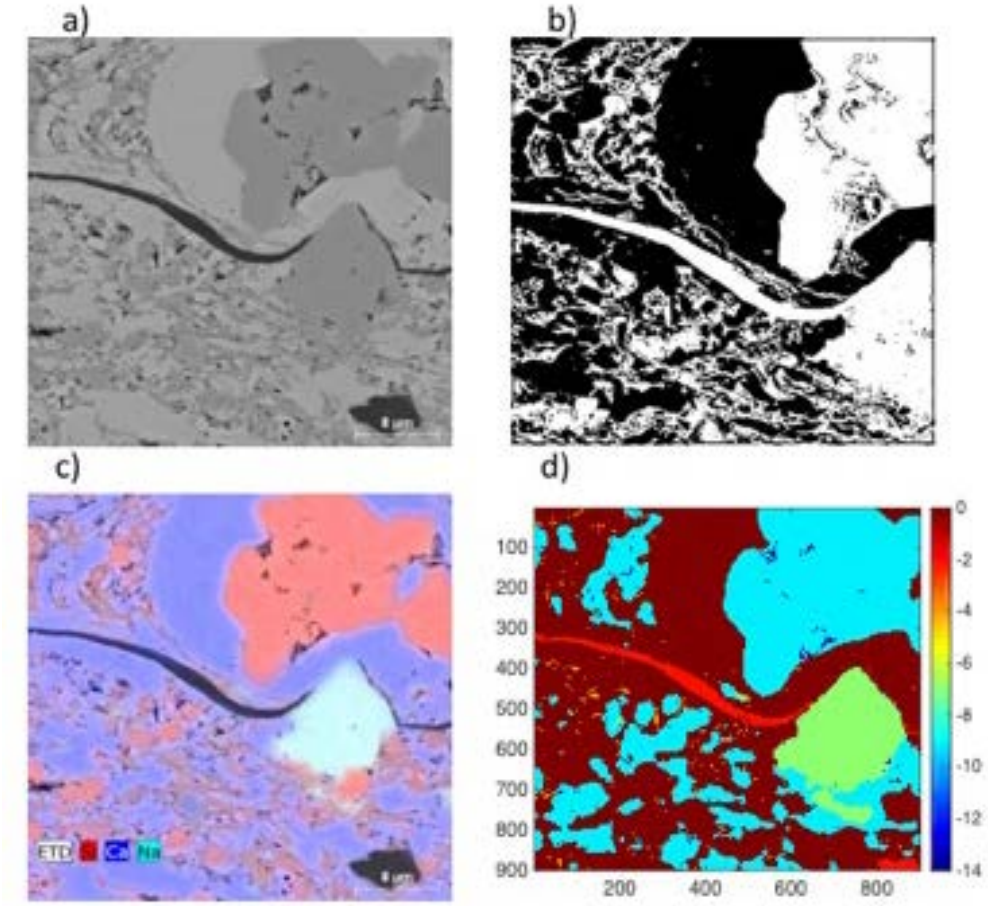

Figure 50. (a) Grayscale image; (b) edge-detection; (c) RGB image; (d) segmented mineral map used to assign seismic properties for wavefield simulation.

The process developed to obtain Figure 50d is explained here. First, if we were to rely solely on thresholding the grayscale intensity histogram (Figure 51), it is quite evident that we cannot separate viably each mineral. Although three distinct peaks are apparent in the histogram, separating quartz and feldspar is not possible.

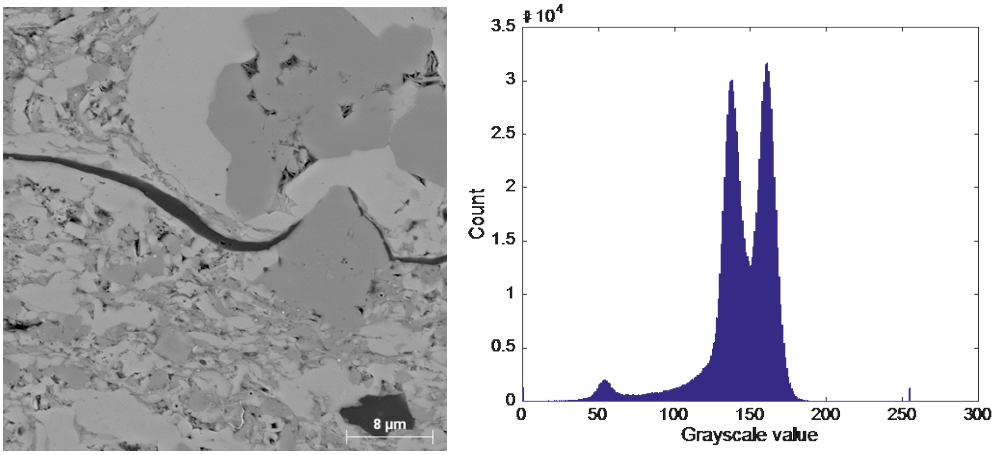

Figure 51. Grayscale image (left) and its corresponding grayscale histogram (right). If segmentation is based on thresholds determined from the histogram, non-unique results would entail where different minerals would be assigned the same value.

Fortunately, the imaging technology also provides elemental-based RGB images. Figure 52 contains color images of aluminum, calcium, potassium, sodium, carbon, sulfur, and silicon. These images indicate the locations of the major constituents in terms of minerals. Those elements correspond to clays (aluminum, potassium, and silicon), calcite (calcium), Na-feldspar (sodium and silicon), quartz (silicon), and to organic matter (carbon and sulfur). However, these elemental images still do not provide unique separations for the minerals.

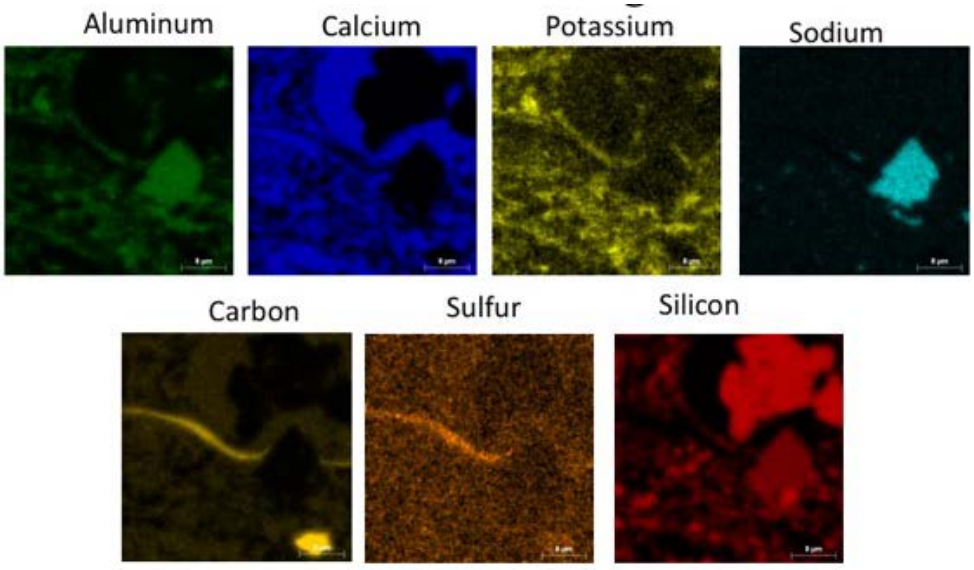

Figure 52. Element-by-element images used to construct the color image in Figure 50. These images are used in various ways to identify the major constituents in the overall image.

Grayscale equivalents of the color elemental images are in Figure 53. Here, we threshold each individual image to aid in the location of each mineral. The following steps are to identify and isolate each of the major constituents.

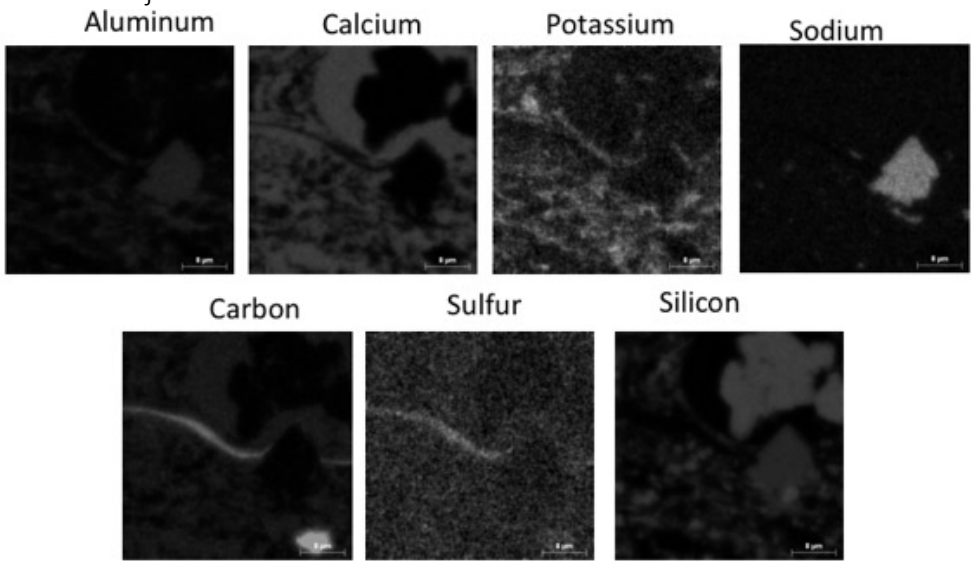

Figure 53. Each of the elemental images in Figure 52 must be converted to an 8-bit grayscale image. These grayscale images are thresholded in various ways to separate quartz, feldspar, calcite, clays, organic content, and pores.

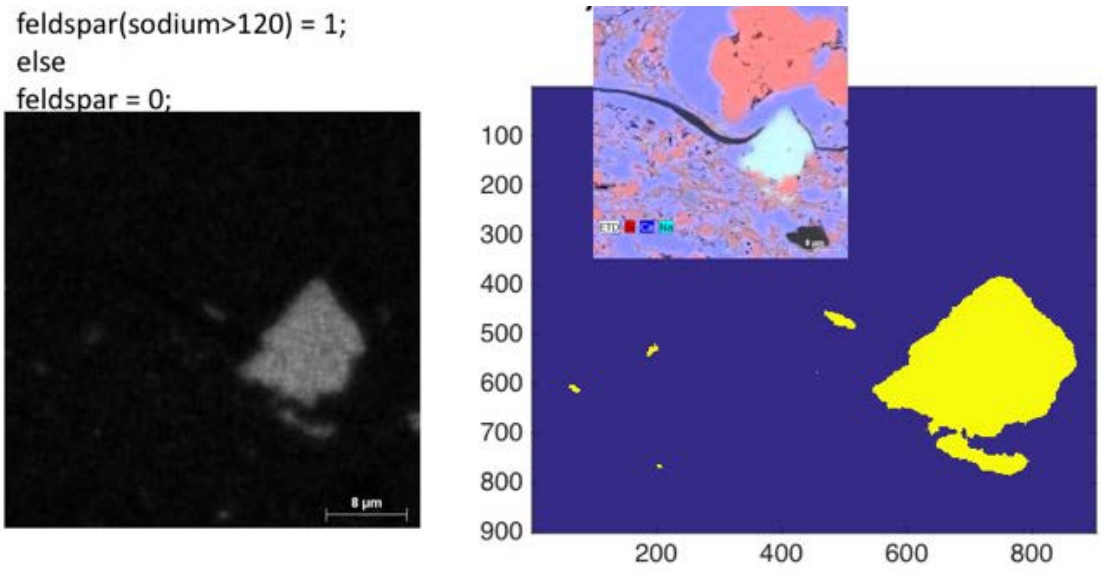

Figure 54. Relatively small amounts of feldspar are present in the color image (overlay, cyan color). The 8-bit grayscale sodium image (left) indicates quite clearly where the feldspar grains are. A threshold for the sodium image (left) assigns the appropriate pixels an integer value (yellow) for feldspar. Every other pixel is assigned a value of zero.

The first to tackle are the feldspar grains. Examination of grayscale histogram for this image indicated a threshold value of greater than 120 corresponds to feldspar (histogram not shown). The resulting integer image in Figure 54 shows the feldspar locations in yellow.

Quartz is the second mineral to identify and place. The silicon grayscale image contains traces of clays and feldspar in addition to the quartz, so this process requires several sub steps. The first is to threshold the grayscale image. Specifically, any value above 18 is assigned to quartz (Figure 55). Those locations are then placed in the feldspar image in Figure 54. Figure 55c is the combined quartz and feldspar image. Through some simple manipulation, the feldspar portion is then subtracted from the overall image to remove the feldspar (Figure 56). As a result, an image for quartz and for feldspar become available.

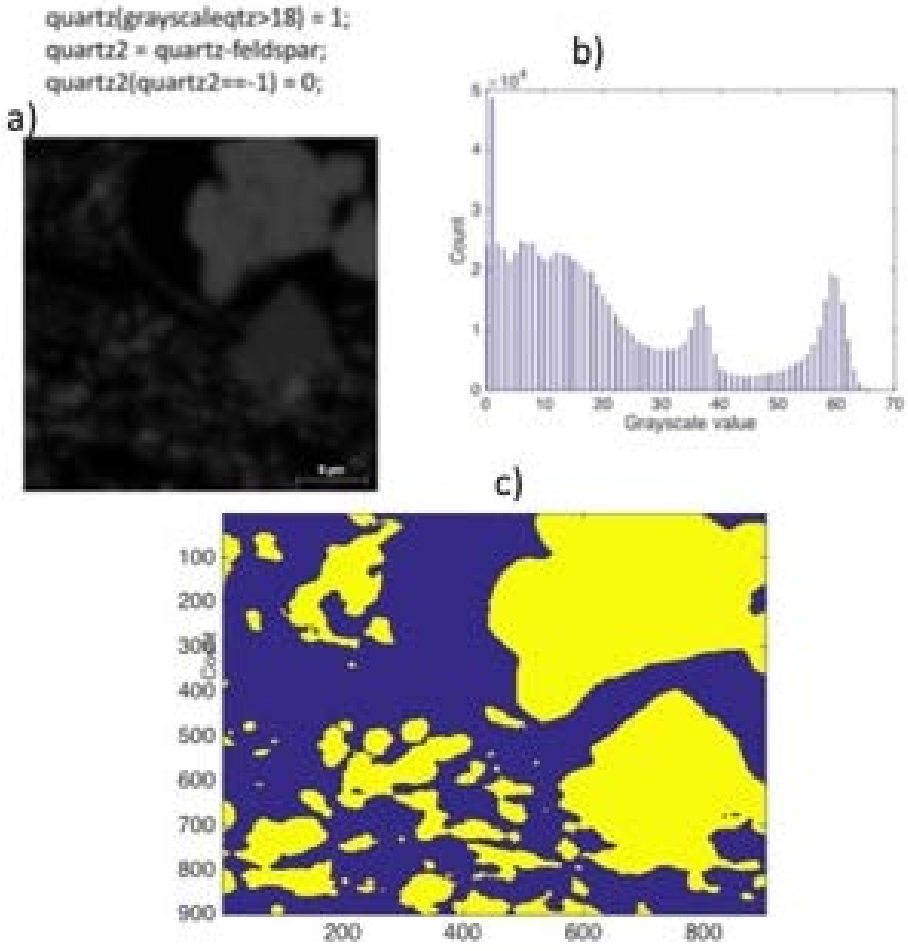

Figure 55. In a) is the silicon 8-bit grayscale image along with its histogram (b). A threshold value of 18 and greater corresponds to quartz. However, feldspar is also included in c) where yellow corresponds to both quartz and feldspar.

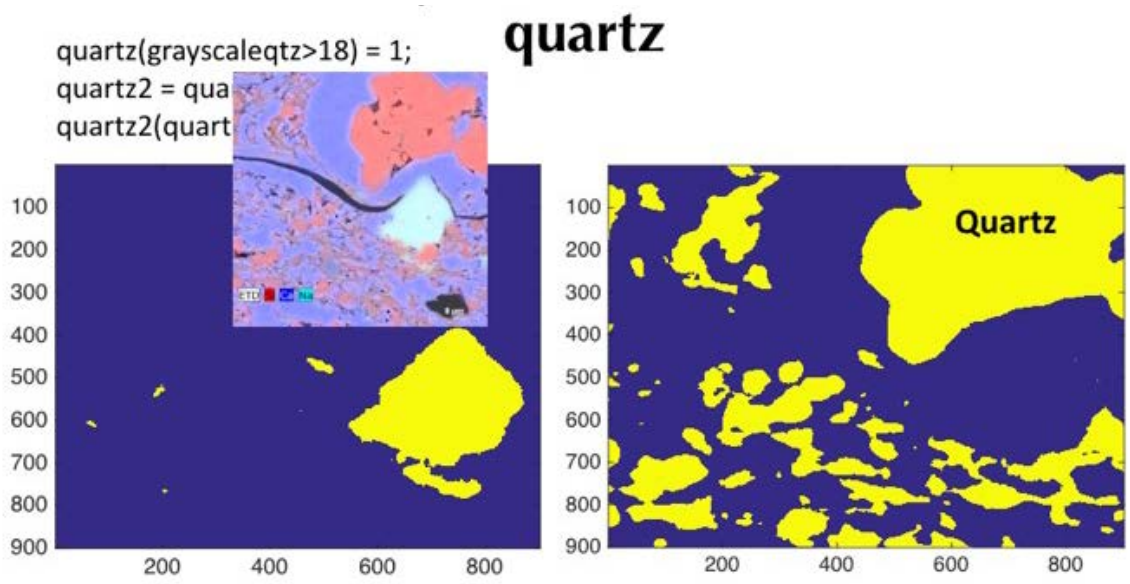

Figure 56. To separate quartz and feldspar, the feldspar image and the quartz image are assigned different integer values for the minerals. This allows the quartz image to be subtracted from the feldspar one, leaving two independent images.

Because of the sharp edges of organic content, clays, and pores, edge detection algorithms become necessary to augment the elemental images. Three processes were chosen that involve convolution of simple matrices (Figure 57) with the original grayscale image in Figure 50. The matrices are used sequentially (top to bottom in Figure 57) to smooth, identify edges, and then to smooth again. The edge-detected image Figure 57 highlights the organic matter, pores, and clay edges.

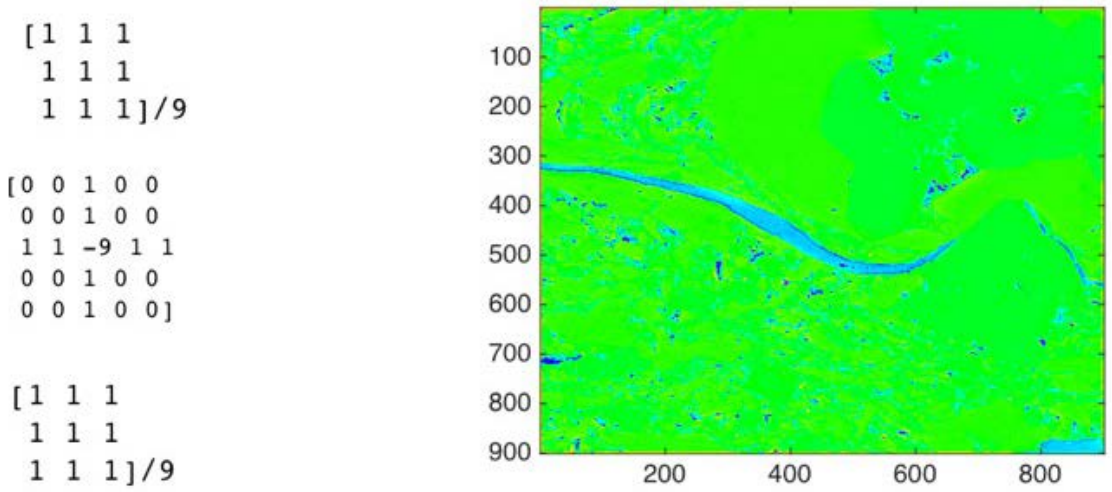

Figure 57. To demarcate pores, clay, and organic matter, an edge-detection algorithm was used to highlight them. The original grayscale image was convolved with three simple matrices (left) resulting in the image on the right. The first smoothed the image, the second found the edges, and the third smoothed again.

The grayscale version of the image in Figure 57 is then examined in terms of its histogram, and once again a threshold is applied (Figure 58a) to obtain a binary version of the edge-detected image. Combining this binary image with the grayscale carbon image (Figure 58b) along with some scaling factors, we can separate the organic matter from clay and pores. Because the original color image clearly indicates where the organic matter is, some simple manual zeroing out of the clays and pores leaves just the organic matter locations (Figure 58d). Simple integer math and a subtraction of the Figure 9d from Figure 9c gives the pores and clays in Figure 58e.

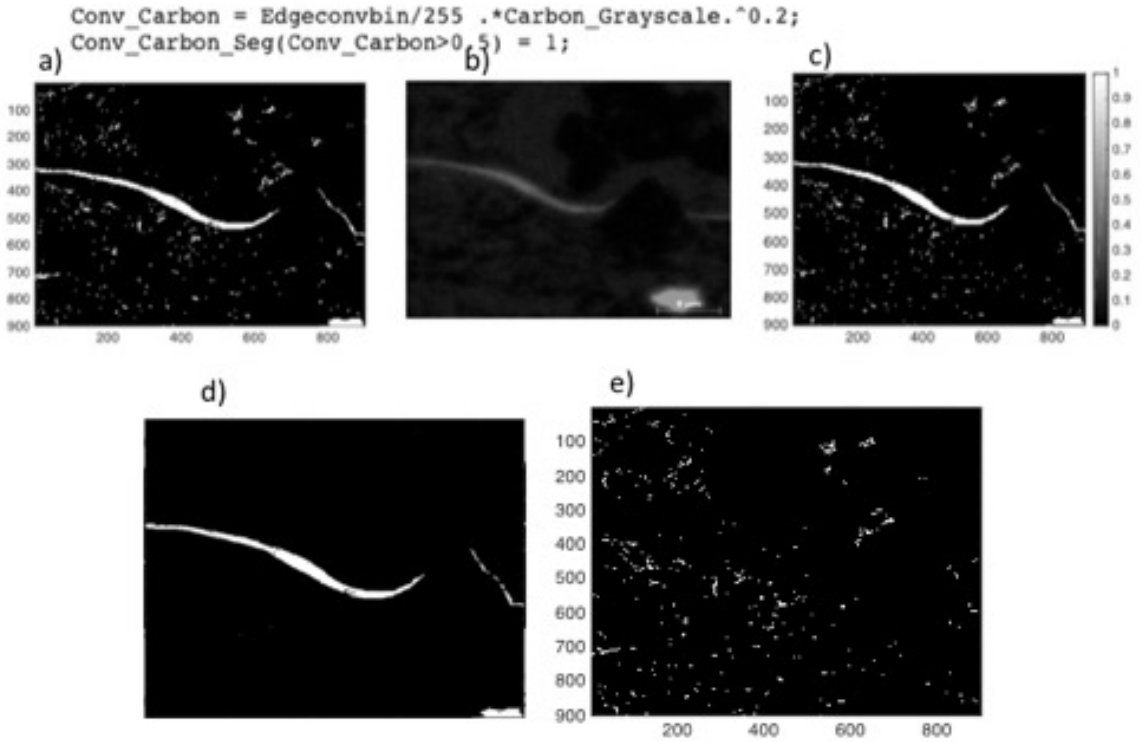

Figure 58. The edge-detected image (Figure 57) is converted to binary image through a threshold (a). a) is combined with grayscale carbon image (b) and scaled with an exponent to identify the organic matter (c) that also contains pores and clay. Manual zeroing of the pores and clays resulted in the organic matter image (c). Integer exchange and subtraction resulted in the clays and pores image in e).

The final major constituent, calcite, is the next mineral to account. This step is quite straightforward because it involves a subtraction of 1–quartz. Figure 59 shows these images. Quartz is in yellow in Figure 59 left and calcite in white in Figure 59 right. Note that the feldspar locations appear to be contained in the feldspar image. However, the feldspar image will be reused to remove it in the final compilation step.

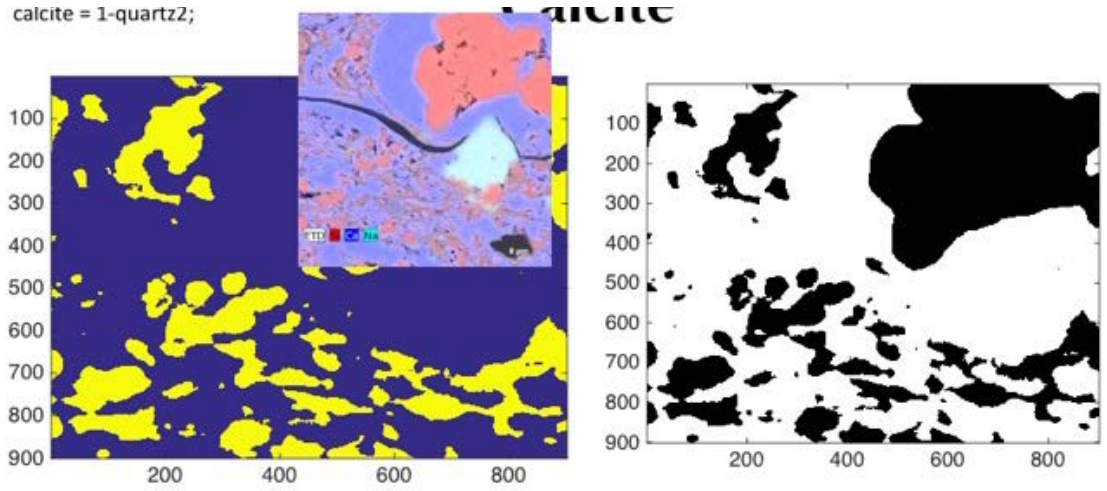

Figure 59. Identification and placement of calcite was simply obtained by subtracting the quartz image from a value of 1. In the overlay, blue is calcite and red is largely quartz. In the left image, yellow is quartz. In the right image, white is calcite. This calcite image also includes feldspar, but that is removed in the final compilation step.

The final separation is that of clays from pores. These are separated using Figure 58e and a thresholded aluminum image. Finally, with quartz, calcite, feldspar, clays, organic matter, and pores individually separated, the final image compilation becomes easy. Each mineral image is simply added along with some integer identifiers. Figure 60 is the final image of minerals, pores, and organic matter. This image is then used as the framework for the elastic wavefield simulation.

```
sc.quartz = quartz*-9;
sc.feldspar = feldspar;%.*-7;
sc.clay = Clay2.*-5;
sc.TOC = TOC.*-3;
sc.calcite = calcite;

final = sc.quartz + sc.feldspar +
sc.clay + sc.TOC + sc.calcite;
final(final>=-1) = 0;


0 = Calcite;
-4 = pore space
-12 to -14 = clay
-9 = quartz
-2 = TOC
-7 = Feldspar
```

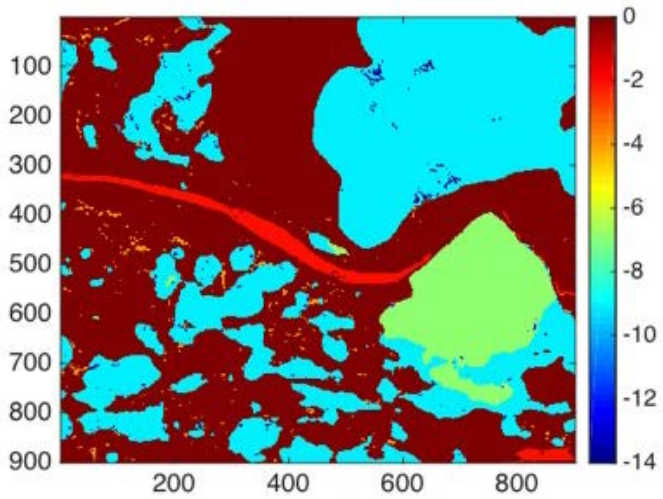

Figure 60. Final mineral assemblage designated through integer values. The color-integer scheme is on the left. The image on the right contains quartz, clay, organic matter, feldspar, calcite, and pores. Elastic properties can then easily be assigned based on the integer value for each constituent.

For the purposes of simulating the elastic wavefield using the Discontinuous Galerkin (DG) approach, an image must be segmented by mineral and then assigned velocities to each mineral. The image in Figure 60 is assigned P-wave, S-wave, and density values according to each mineral (Figure 61).

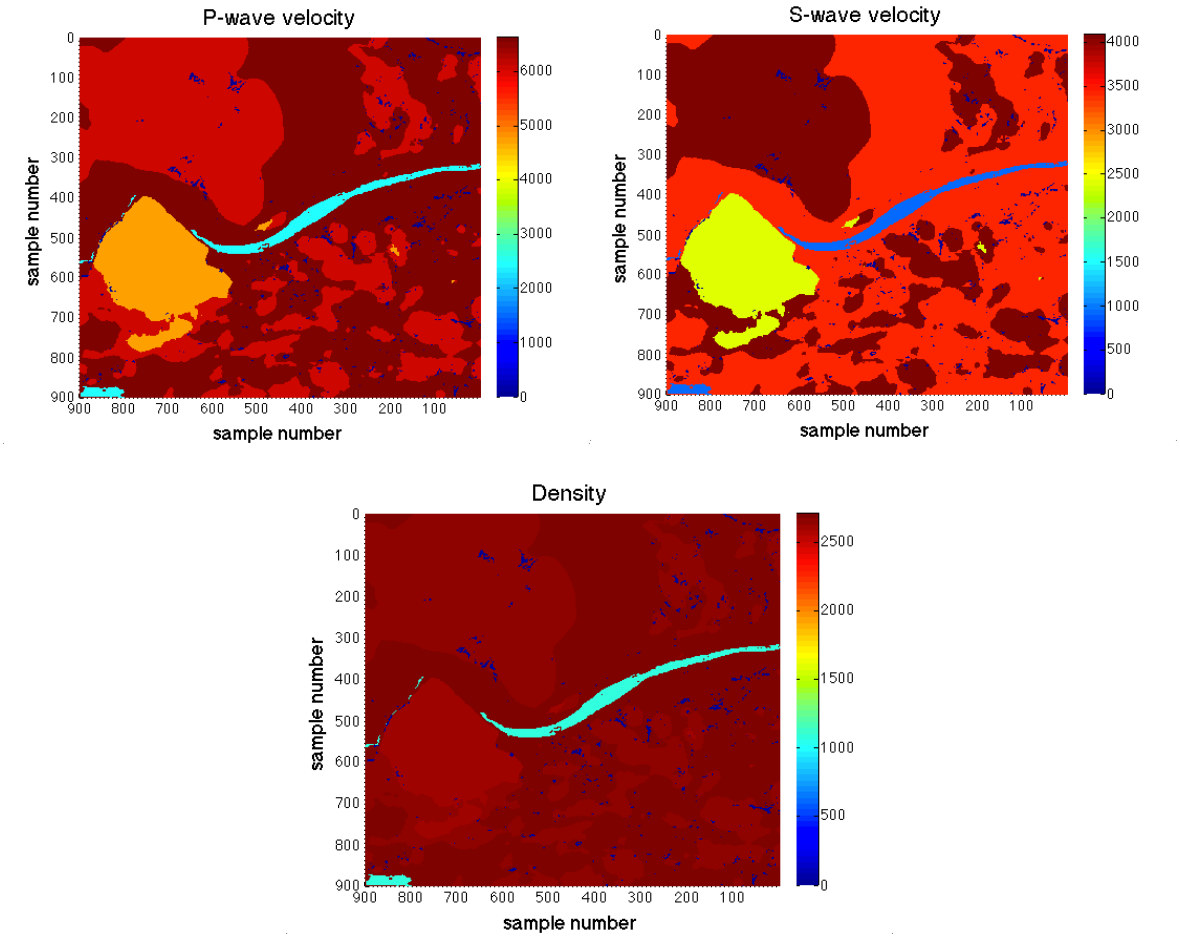

Figure 61. Initial P-wave image (top left), S-wave image (top right), and density (bottom) based on the mineral assemblage image in Figure 60.

Numerical stability of a wavefield simulation depends on the maximum velocity in terms of the time-sampling interval and on the range of velocities for the spatial sampling interval. With a maximum P-wave velocity for calcite (dark red) of greater than 6000 m/s, the time sampling interval must be quite small. To alleviate numerical problems, we were forced to change the velocities of the pores (dark blue, corresponding to empty pores) to that of water (1500 m/s). In addition, some gentle smoothing of the P-wave velocity image was necessary but not a significant amount (Figure 62). The wavelet used is a very high frequency wavelet with dominant frequency of about 100 MHz. This high frequency allows for having two full periods or wavelengths travel through the image.

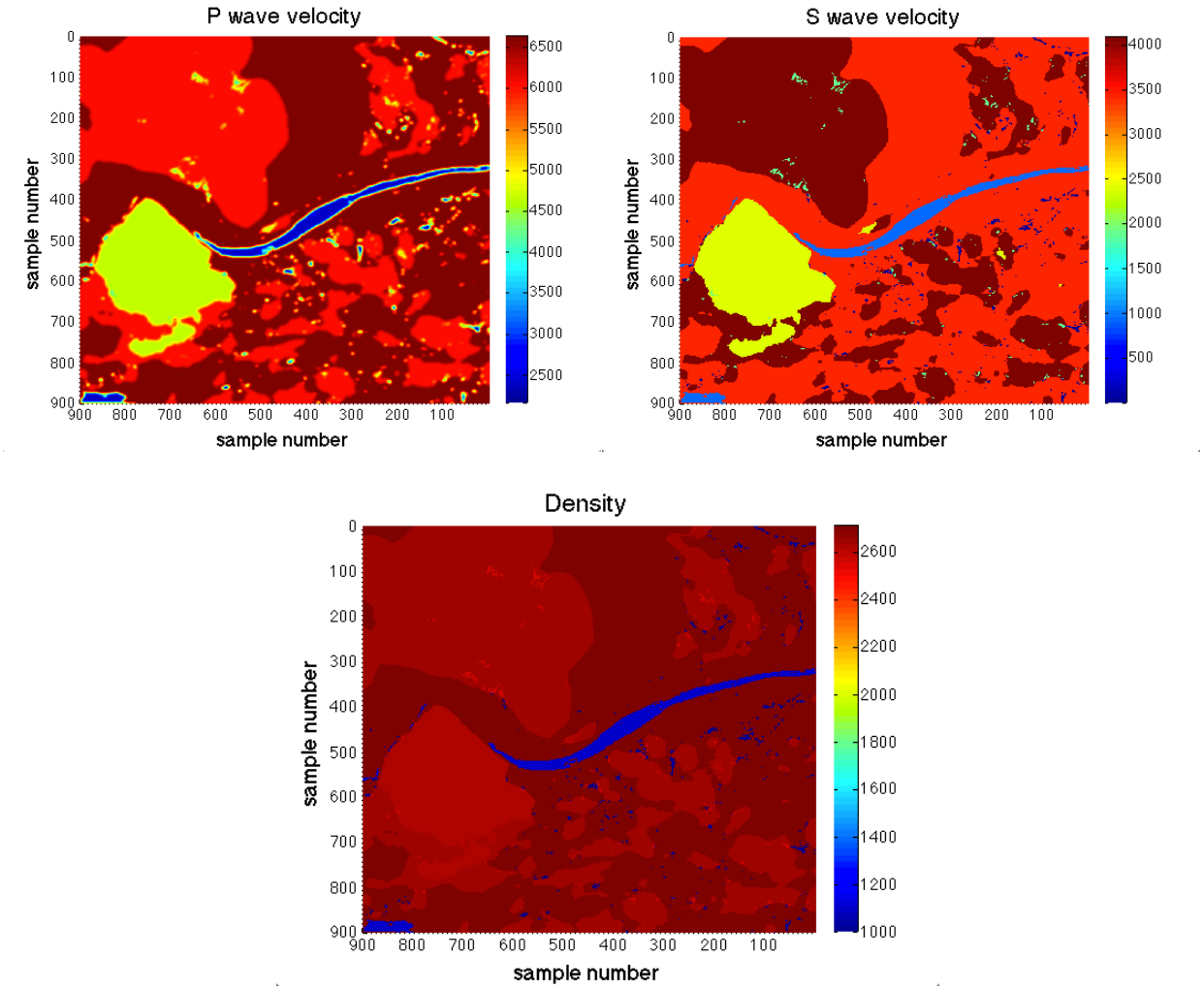

Figure 62. Modified elastic properties, including smoothing and reducing the overall range of velocities for numerical stability purposes. Most features are preserved after the slight modifications. Without these subtle changes, the wavefield simulation algorithm could not converge to a solution.

For the wavefield simulation, we place the source at the top center of the image. Receivers are placed at each node on the bottom of the receiver. This gives us the propagation in the vertical direction of the image. Figure 63 displays a wavefield snapshot () and a seismogram (b) for this vertical wavefield propagation. Because the DG method allows for the waves to propagate across discontinuities such as pores, the wavefield becomes incredibly complex. This is the elastic wavefield, so P, S, and mode-converted waves are present. The thin strip of organic matter shows internal diffractions and reflections because it has large contrasts in elastic properties relative to its surroundings. The seismogram in Figure 63b is used for travel time picks of the first arrivals of P and S waves. Table contains the summary of the picking information.

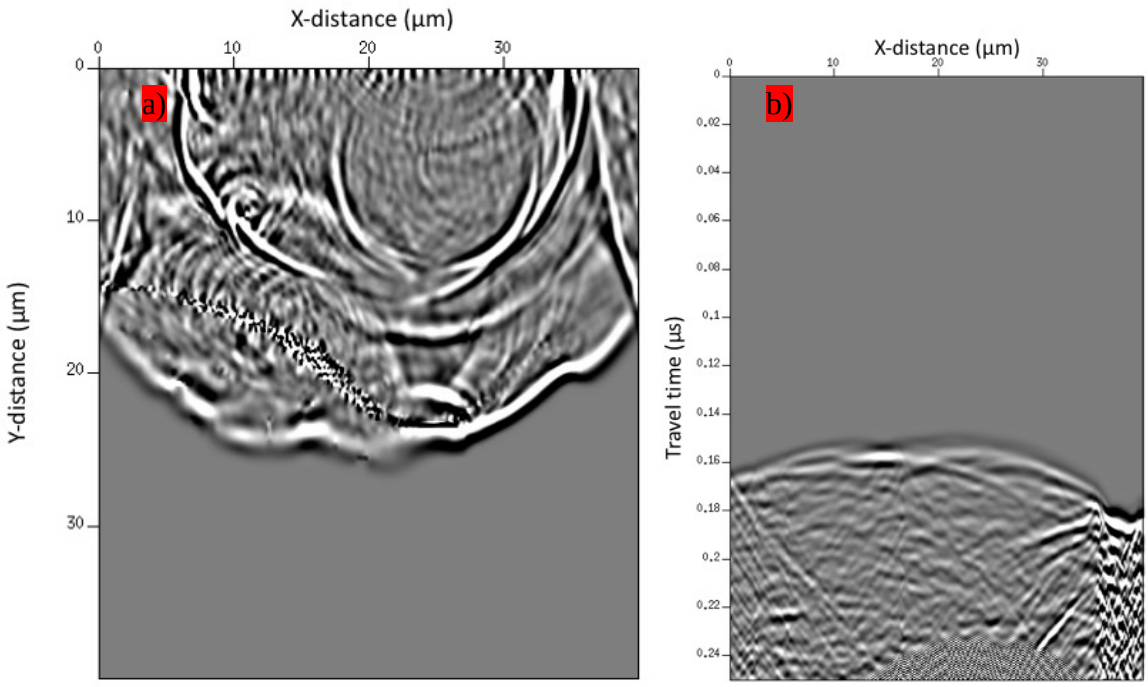

Figure 63. a) Wavefield snapshot and b) seismogram for the vertical wavefield simulation. The source was placed at the top center of the image and receivers along the bottom. This represents a point source type seismic experiment. The complex wavefield is a result of the DG algorithm sensing all features and allowing for the wavefield to propagate across discontinuities. The seismogram in b) allowed for picking first-arrival P- and S-waves.

A second wavefield simulation in the horizontal direction (Figure 64) provides the seismic anisotropy estimate that we expect. This simulation involves placing the source on the left side of the image in the center and the receivers on the right. The wavefield in Figure 64a sees the image in terms of the fastest materials as the dominant. Counter to this, the vertical one Figure 63a senses the slowest materials. The horizontal seismogram (Figure 64b) shows multiple events that appear to arrive at the same time. This is due to the horizontal wavefield following the fastest paths through the image. Most importantly, the travel times in Figure 64b are slightly less than those in Figure 63b for the first arrivals. The effective velocities are given in Table 4 for both vertical and horizontal simulations.

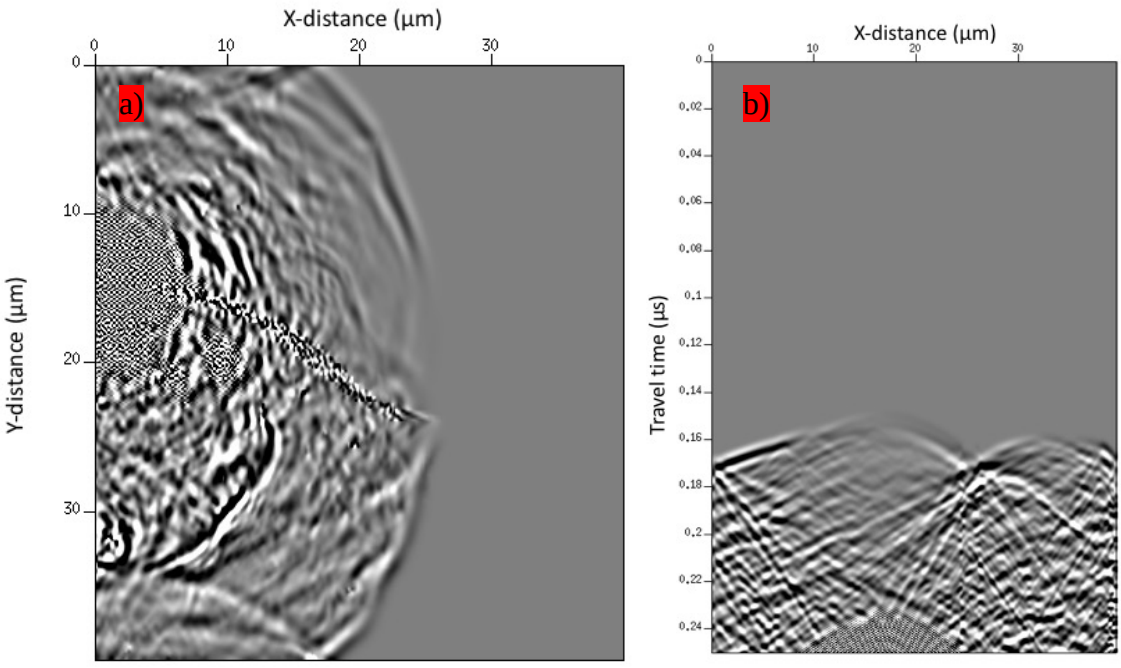

Figure 64. Horizontal wavefield snapshot (a) and the seismogram (b). For this experiment, the source was placed on the left side of the image and receivers along the right edge. The vertical and horizontal experiments provide the anisotropy estimates.

Vertical	1	2	3	Mean
P travel time	0.149µs	0.163µs	0.181µs	-
S travel time	0.242µs	0.260µs	0.280µs	-
Distance	40µm	44.71µm	44.71µm	-
Vp	6.04km/s	6.17km/s	5.56km/s	5.92km/s
Vs	3.72km/s	3.87km/s	3.59km/s	3.73km/s

Horizontal	1	2	3	Mean
P travel time	0.146µs	0.168µs	0.167µs	-
S travel time	0.239µs	0.256µs	0.256µs	-
Distance	43.07µm	44.71µm	44.71µm	-
Vp	6.63km/s	5.99km/s	6.02km/s	6.21km/s
Vs	4.05km/s	3.93km/s	3.93km/s	3.97km/s

Table 4. Three travel time picks for both P- and S-waves were made on the vertical and horizontal seismograms. Mean velocities indicate faster horizontal velocities than vertical, which is expected given the fabric of the image.

Three picks were made on the vertical and horizontal seismograms. Additional picks across the full wavefronts will be done for a more accurate set of effective velocities.

3.6.2 Ultrasonic Velocity Picks

This section presents results of picking directional ultrasonic velocities on sample Siliceous 3-14. This process involves making manual picks of first arrivals of P and S waves on waveforms. These waveforms were propagated through the sample at varying effective pressures. P-wave first arrivals tend to be easier than S-wave arrivals, but these samples and the resulting measurements prove quite challenging. Figure 65 displays the vertical P (left) and vertical S (right) waveforms for pressures from 1 to 32 MPa. The picking is made according to the interpretation of the onset of energy. The P-wave arrivals are relatively clear, but the S-wave ones are quite subjective.

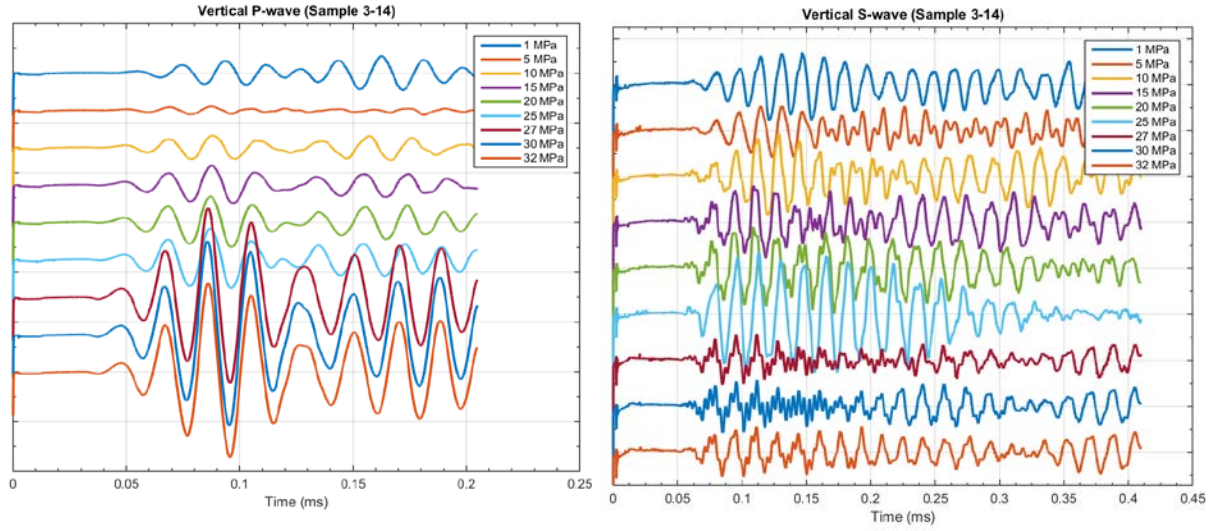

Figure 65. Waveforms from sample Siliceous 3-14 for the vertical P (left) and S (right). Vertical means propagation perpendicular to layering. The onset of energy in the P-waveforms are relatively clear to pick, but the S-waveforms present subjectivity.

Figure 66 contains the horizontal P and S waveforms over a pressure range of 1 to 25 MPa. Similar to the vertical waveforms, the P wave first arrivals are relatively obvious, but the the S-wave onset of energy is quite difficult to identify.

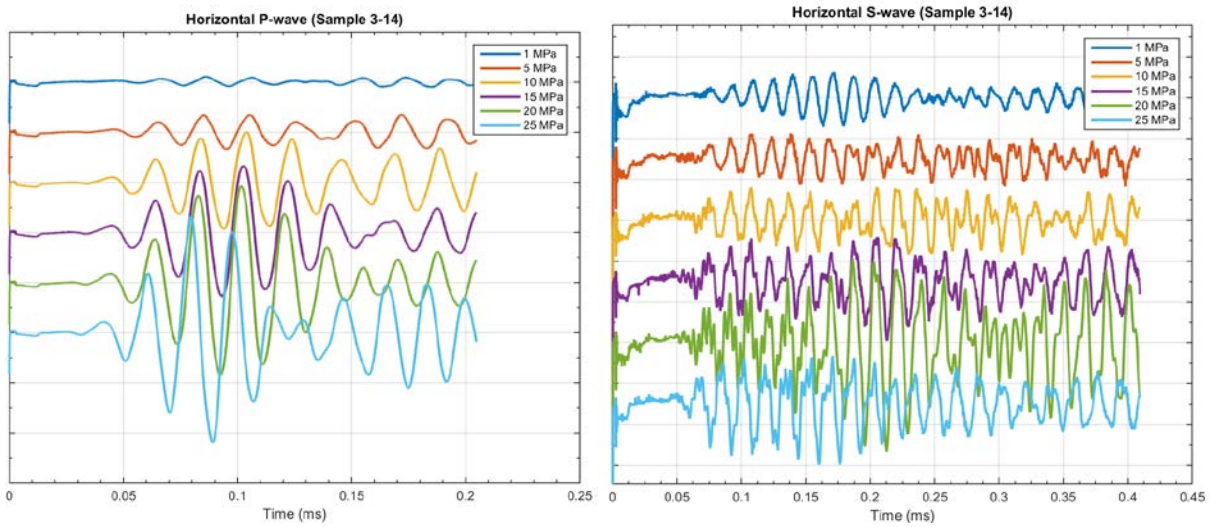

Figure 66. Waveforms from sample 3-14 for the horizontal P (left) and S (right). Horizontal means propagation parallel to layering, which is the fast direction. The onset of energy in the P-waveforms are relatively clear to pick, but the S-waveforms present subjectivity.

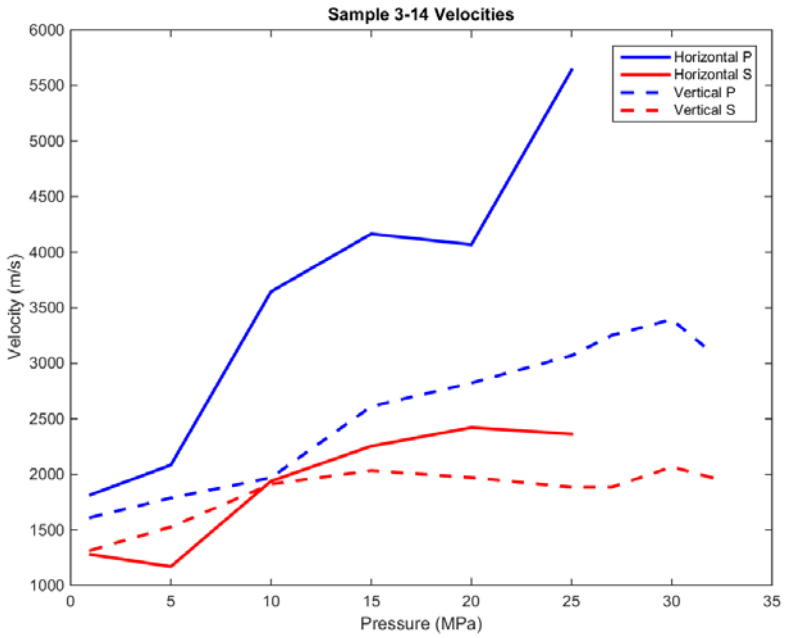

Figure 67. Picked velocities from the waveforms in Figures 65 and 66 as a function of pressure. Above pressures of 10 MPa, the overall relative values of velocities follow general expectations, with the vertical S the slowest, then horizontal S, the vertical P, and the fastest is the horizontal P. However, the pressure-dependent behavior of each is complex and likely uncertain because of the difficulty in picking the onset of energy.

The picked velocities for the waveforms in Figures 65 and 66 are shown in Figure 67. In general, velocities increase with pressure. Clearly, each curve behaves quite differently. Above 10 MPa, the velocities display anisotropic behavior for layered media that we expect. Namely, the horizontal P is faster than the vertical P, and the horizontal S is faster than the vertical S.

3.6.3 Inclusion-Based Rock Physics Modeling

Wavefield simulation through an image in two directions provides evidence of anisotropy and of possible representative values of the velocities for the whole sample. This information must be combined with velocity measurements made on the sample to understand any variability. An additional modeling method, using inclusion-based rock physics models, can provide explanations of the measured velocities to be compared also to the wavefield simulations.

The SCM approach treats each constituent (i.e., phase) as an ellipsoidal inclusion with an assigned bulk and shear modulus and density. In the anisotropic treatment, these inclusions are aligned with their major axis in the horizontal direction. Each has an aspect ratio, the ratio between the minor and major axes lengths. A smaller aspect ratio has a smaller stiffness. Each phase has a fractional proportion assigned to it. Table 5 contains those specific values.

	Bulk Modulus (GPa)	Shear Modulus (GPa)	Density (g/cm^3)	Aspect Ratio	Proportion
Quartz	36	45	2.65	1	0.25
Clay	20	7	2.55	1e–4	0.25
Feldspar	37.5	15	2.62	1	0.2
Kerogen	4	2	1.0	1e–5	0.15
Calcite	75	31	2.71	1	0.05
Pores	0	0	0	1e–2	0.10

Table 5. Minerals and their properties used in the anisotropic self-consistent modeling.

For the Siliceous 3-14 sample, the anisotropic self-consistent model (SCM) was chosen. A set of SCM models and the effective velocities from the wavefield simulations are overlain on the picked velocities in Figure 68. The data are replotted and are the same as in Figure 67. Horizontal black lines are for the wavefield simulated P-waves; magenta correspond to wavefield simulated S-waves. Horizontal blue lines are the SCM P-waves; red are the SCM S-waves.

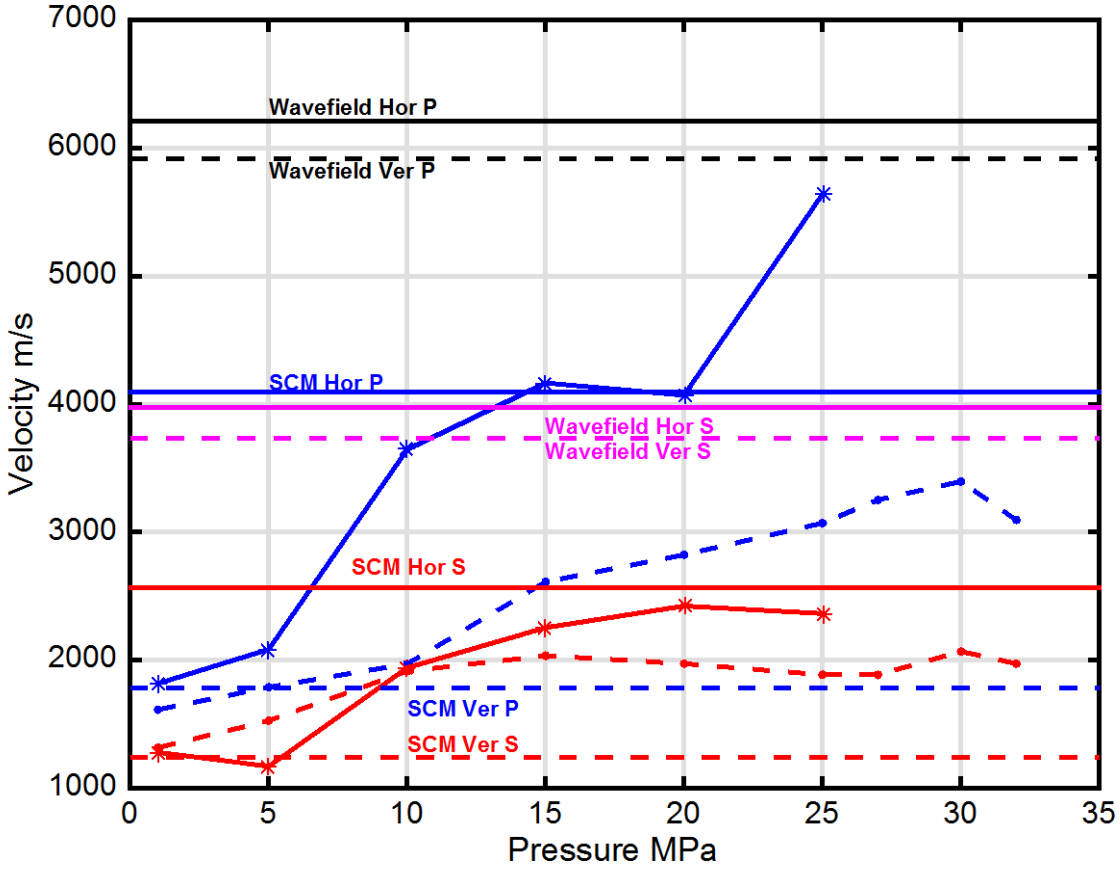

Figure 68. Compilation of the picked velocities (same as in Figure 67), the wavefield simulation velocities (black for P and magenta for S), and the SCM velocities (blue for P and red for S). The wavefield and SCM velocities are plotted as horizontal lines for qualitative comparison to the picked velocities. Clearly, the wavefield velocities overestimate the picked values. The SCM velocities partially explain the picked data. For example, the SCM horizontal P seems to explain the picked velocity at 14 and 20 MPa. However, the SCM horizontal S overestimates the picked horizontal S at all pressures. The vertical SCM P and S match the picked value only at low pressure, less than 5 MPa.

3.7 Imaging

To test how fractures connect with pores across micrometer-to-nanometer scales, we prepared 46 subsamples from 8 samples of the Siliceous and Eagle Ford shales. These samples reflect those deformed in the BEG rock deformation laboratory (see Section 3.5) and intact counterparts provided by EOG and lead-PI Daigle ("Pre" and "Post" in Table 6). The orientation of sub-sample preparation provided views of the bedding planes ("Bed") or cross-sectional views ("X-section"), from cores deformed either "parallel" or "perpendicular" to bedding (Table 6).

Of the subsamples, we have prepared 16 for imaging in the BEG JEOL FE-SEM (Focused-Energy Scanning Electron Microscope) and Zeiss mosaic-enabled FE-SEM. Of these, 8 have been

prepared in-house via ion milling (Milliken et al., 2013), producing a polished surface that allows imaging to the nanoscale (Fig. 69a). We also prepared 12 polished thin sections (via Wagner Petrographics) that allow finer detail on grain boundaries and grain-matrix relationships, though not to the same nanometer-scale enabled by ion milling (Fig. 69b). In most cases we have collected both BSE (back-scattered electron) and X-ray maps via EDS (electron dispersive spectroscopy) allowing superposition of elemental composition information over grayscale (approximately by molecular weight) textural information (Fig. 69c). The Zeiss FE-SEM allows for mosaics to be constructed during imaging (Fig. 70).

Additional sample preparation and imaging was done in collaboration with FEI (results forthcoming). In the proposed research we pledged to collect three-dimensional imaging via FIB (focused-ion-beam). Subsequently, we learned that the UT Austin nanotechnology center's FIB is not well-suited for our purposes. Thus, we negotiated an academic rate (comparable to the original budget for 3D imaging) with FEI. FEI is saturating one of our samples with an iodine solution to enhance FIB imaging, and also providing micro-CT (computerized tomography) image volumes from the same sample. A second sample has been imaged with micro-CT, and after imposing a slight strain, we will image it again (with both micro-CT and FIB) in an effort to observe fracture propagation in the same volume (see below).

In many images we observe fractures that: (i) cut along grain boundaries, (ii) preferentially follow layers of organic matter (OM), and (iii) across grain boundaries and into OM (Figs. 69, 70, 71, 72). We have not found a clear correlation between fractures and their host phases, though OM and matrix minerals (clay) appear to define separate fields; fractures appear to form preferentially within OM (Fig. 73). In the latter case we observe fractures that connect with nanoscale pores, a process we term "pore capture". Samples that have been subjected to deformation tend to have more fractures than the pre-failure samples (Fig. 74).

We note that it is difficult to confidently discriminate between fractures caused by natural deformation at depth, unloading, or imposed strain by the rock-deformation experiments (in "post"-deformation samples). We also note that in an analysis of crack length per image area, "post-deformation" samples have a higher crack length, suggesting that some of the imaged fracture length formed during the rock deformation experiments in those images. An analysis from first principles based upon reasonable stress conditions and elastic properties is in progress that should also shed light on the origin of fractures in the microstructure.

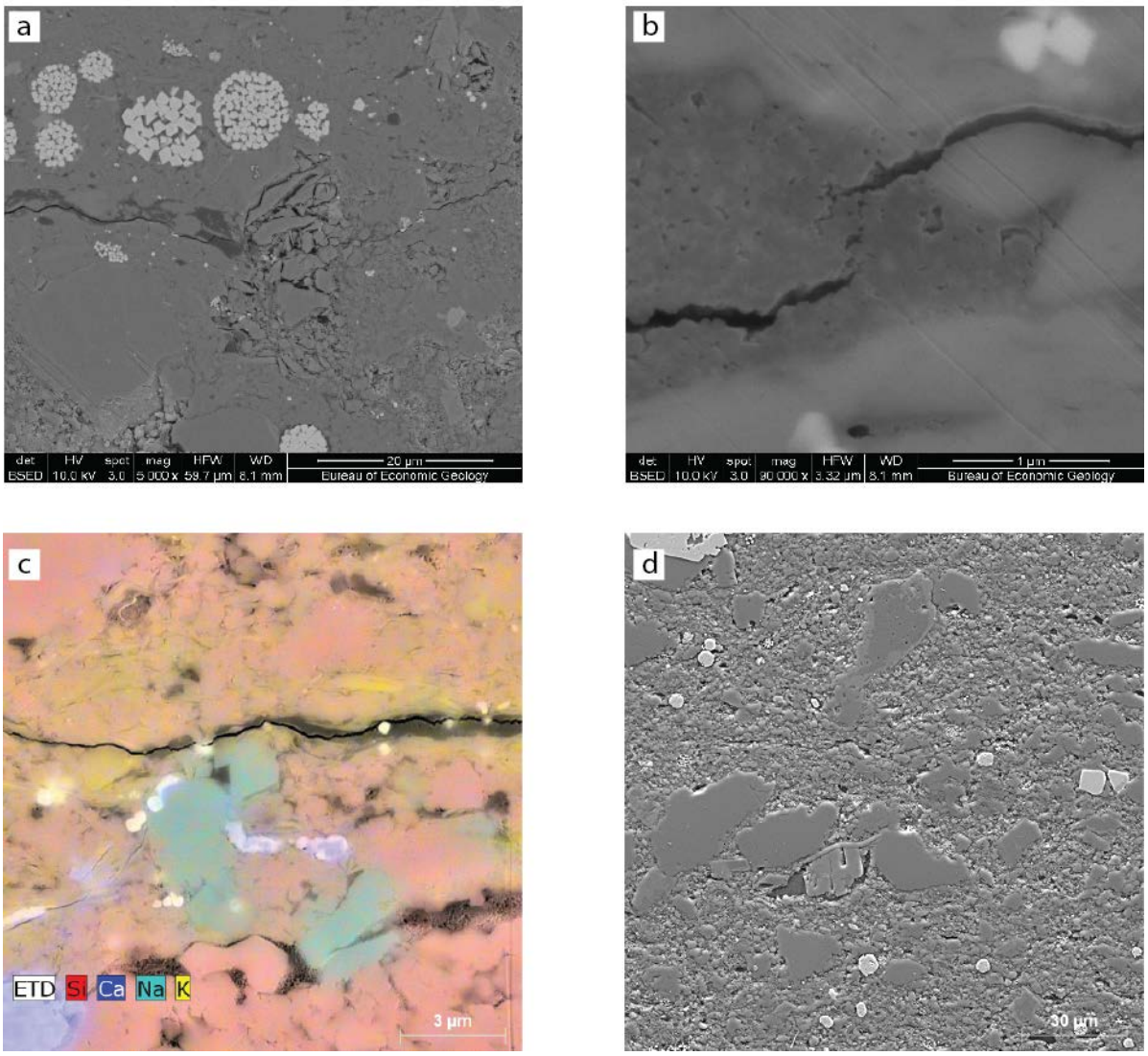

Figure 69. (a) fracture following OM into a brecciated region of Siliceous shale, (b) "pore capture" in OM in Siliceous shale, (c) fracture cuts layer of OM in Siliceous shale, with an example of a superposed X-ray map, (d) FE-SEM BSE image of polished thin section to show contrast with ion milled samples (a-c).

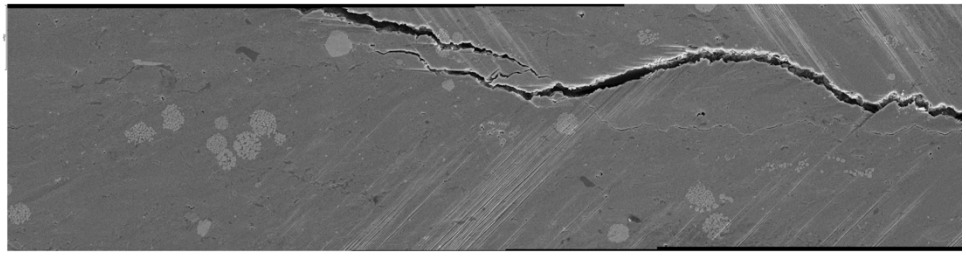

Figure 70. Mosaic from the Zeiss FE-SEM illustrating a fracture with crack-tip branching structure in Siliceous shale.

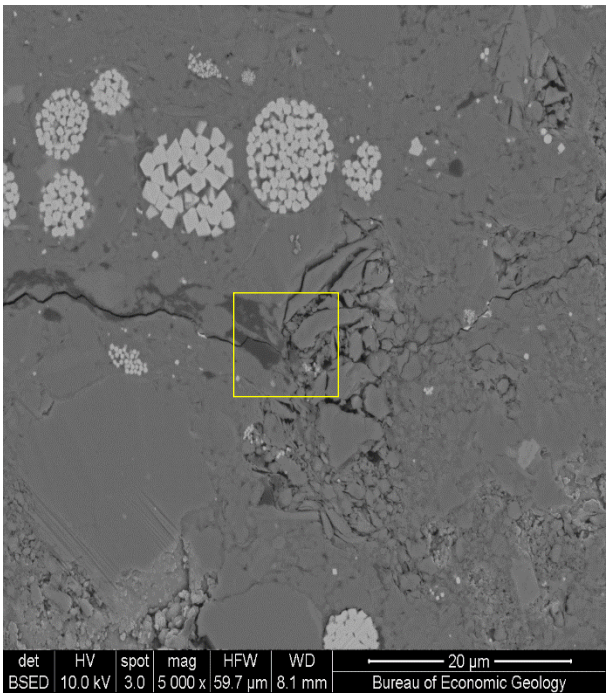

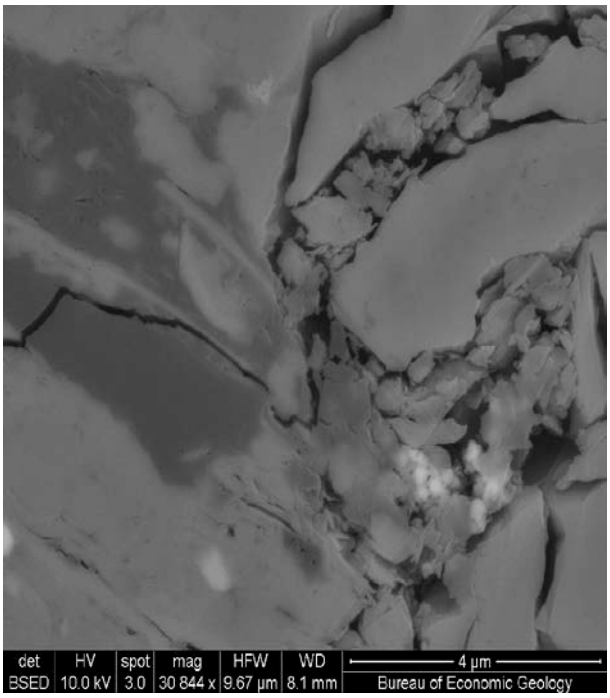

Figure 71. FE-SEM BSE images of Siliceous sample 3-53 post-failure. Stress was applied normal to bedding and normal to the plane of the images. Overview (left) shows pervasive dilatant shear in clays. Close-up image (right; location marked by yellow box at left) show propagation of fracture into organic matter associated with dilatancy in clays.

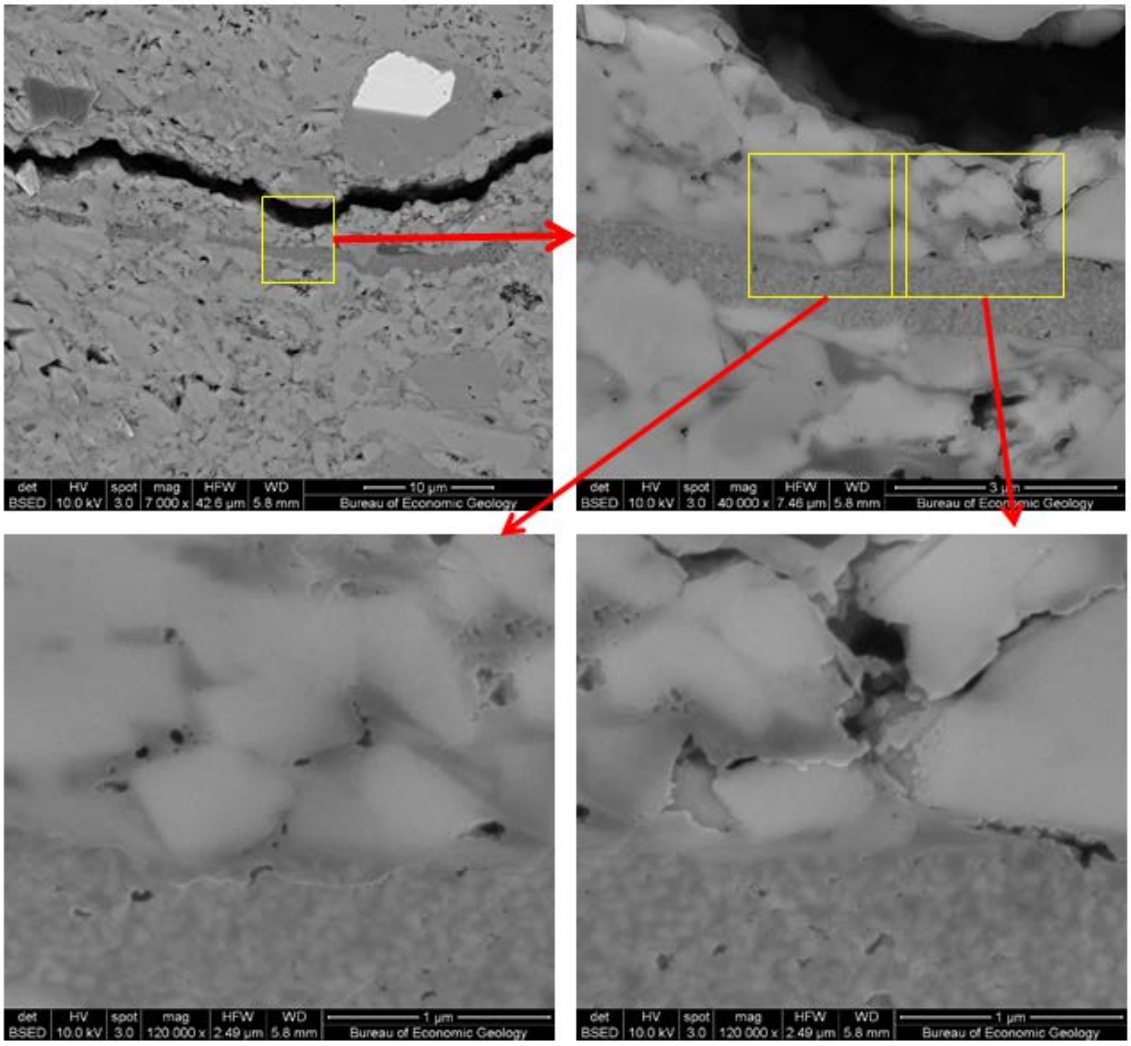

Figure 72. FE-SEM BSE images of Eagle Ford sample 1-223 post-failure. Stress was applied parallel to bedding and normal to the plane of the images. Top left: overview of fracture formed during shear failure. Top right: close-up image of fracture (location shown in yellow box in top left image). Bottom left: close-up of fractures propagating into organic matter. Bottom right: close-up of fractures propagating into organic matter.

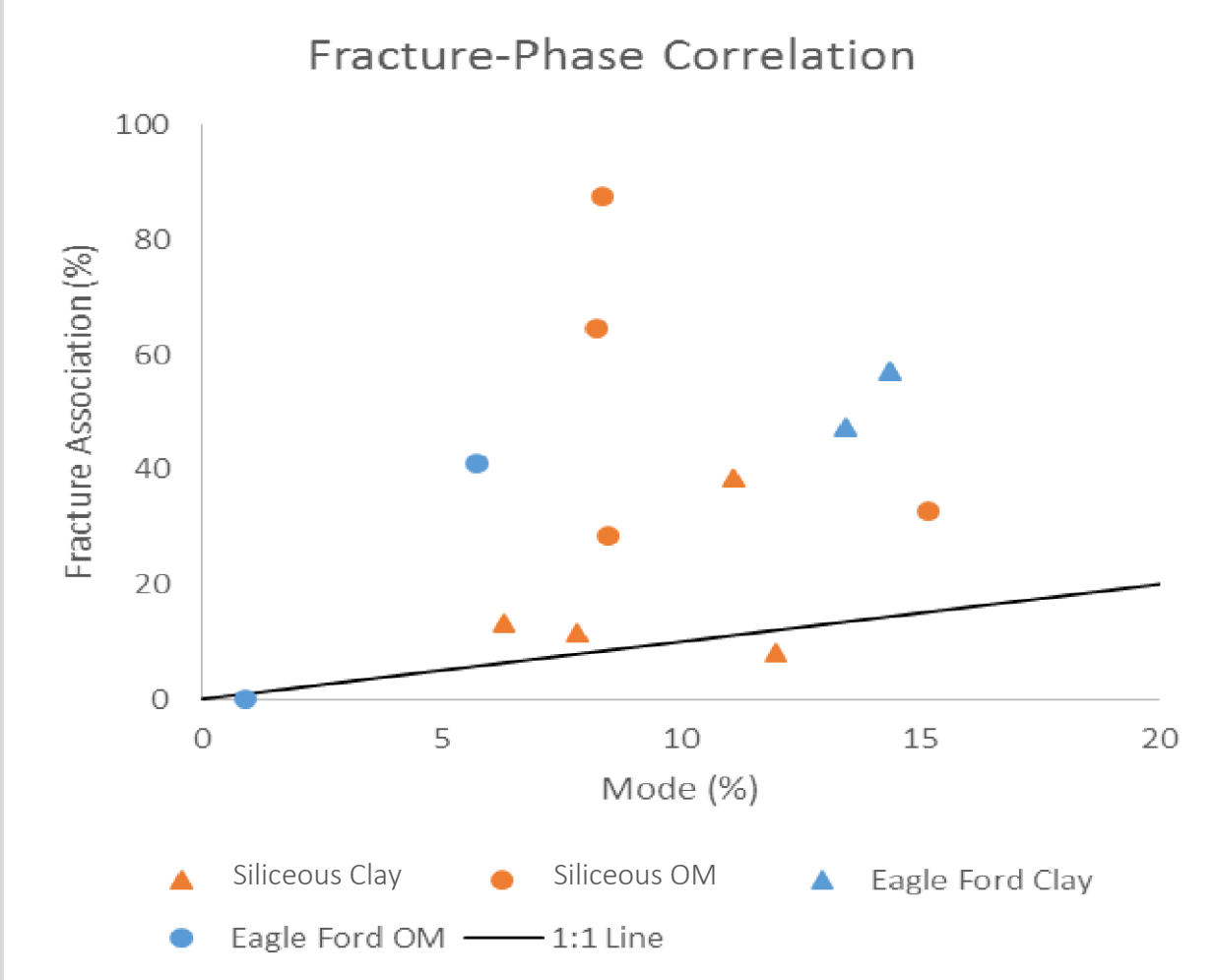

Figure 73. Organic material appears to host more fractures than clay matrix in both Siliceous shale and Eagle Ford.

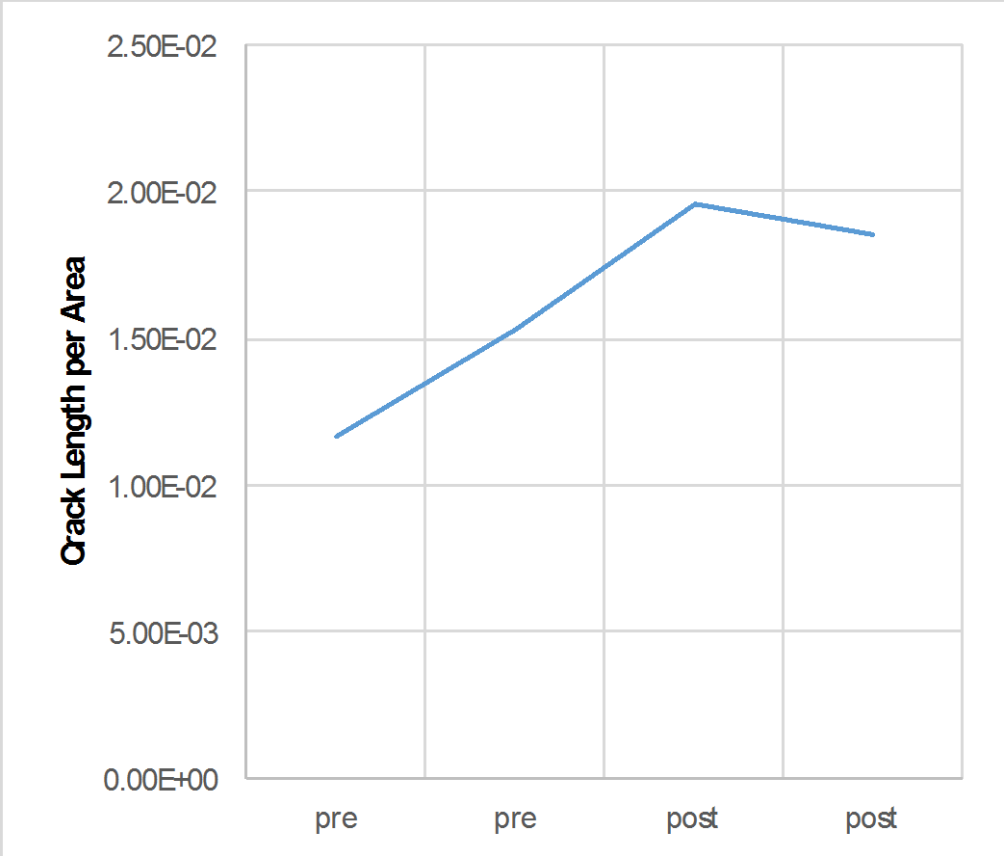

Figure 74. Crack length is higher in samples that have been subjected to rock deformation experiments.

Unique number	Formation	Sample	Failure	Core Orientation	Surface of interest
1	Siliceous	4-34	Pre	Bedding Parallel	Bed
2	Siliceous	4-34	Pre	Bedding Parallel	X-section
3	Siliceous	3-14	Pre	Bedding Parallel	Bed
4	Siliceous	3-14	Pre	Bedding Parallel	X-section
5	Siliceous	3-14	Pre	Bedding Perpendicular	Bed
6	Siliceous	3-14	Pre	Bedding Perpendicular	X-section
7	Siliceous	3-14	Post	Bedding Parallel	Bed
8	Siliceous	3-14	Post	Bedding Parallel	X-section
9	Siliceous	3-14	Post	Bedding Perpendicular	Bed
10	Siliceous	3-14	Post	Bedding Perpendicular	X-section
11	Siliceous	3-42	Pre	Bedding Parallel	Bed
12	Siliceous	3-42	Pre	Bedding Parallel	X-section
13	Siliceous	3-42	Pre	Bedding Perpendicular	Bed

14	Siliceous	3-42	Pre	Bedding Perpendicular	X-section
15	Siliceous	3-42	Post	Bedding Parallel	Bed
16	Siliceous	3-42	Post	Bedding Parallel	X-section
17	Siliceous	3-42	Post	Bedding Perpendicular	Bed
18	Siliceous	3-42	Post	Bedding Perpendicular	X-section
19	Siliceous	3-53	Pre	Bedding Parallel	Bed
20	Siliceous	3-53	Pre	Bedding Parallel	X-section
21	Siliceous	3-53	Pre	Bedding Perpendicular	Bed
22	Siliceous	3-53	Pre	Bedding Perpendicular	X-section
23	Siliceous	3-53	Post	Bedding Parallel	Bed
24	Siliceous	3-53	Post	Bedding Parallel	X-section
25	Siliceous	3-53	Post	Bedding Perpendicular	Bed
26	Siliceous	3-53	Post	Bedding Perpendicular	X-section
27	Eagle Ford	2-50	Pre	Bedding Perpendicular	Bed
28	Eagle Ford	2-50	Pre	Bedding Perpendicular	X-section
29	Eagle Ford	2-50	Post	Bedding Parallel	Bed
30	Eagle Ford	2-50	Post	Bedding Parallel	X-section
31	Eagle Ford	2-93	Pre	Bedding Perpendicular	Bed
32	Eagle Ford	2-93	Pre	Bedding Perpendicular	X-section
33	Eagle Ford	2-93	Post	Bedding Parallel	Bed
34	Eagle Ford	2-93	Post	Bedding Parallel	X-section
35	Siliceous	4-14	Post	Bedding Parallel	Bed
36	Siliceous	4-14	Post	Bedding Parallel	X-section
37	Siliceous	4-34	Post	Bedding Parallel	Bed
38	Siliceous	4-34	Post	Bedding Parallel	X-section
39	Eagle Ford	1-223	Pre	Bedding Perpendicular	Bed
40	Eagle Ford	1-223	Pre	Bedding Perpendicular	X-section
41	Eagle Ford	1-223	Post	Bedding Parallel	Bed
42	Eagle Ford	1-223	Post	Bedding Parallel	X-section
43	Eagle Ford	1-223	Post	Bedding Perpendicular	Bed
44	Eagle Ford	1-223	Post	Bedding Perpendicular	X-section
45	Eagle Ford	1-223	Pre	Bedding Parallel	Bed
46	Eagle Ford	1-223	Pre	Bedding Parallel	X-section

Table 6. Sample table for the imaging effort. See text for definitions and sample descriptions.

4. Conclusion

Our results provide insight into how shales deform at the microscale during shear failure, and have important implications for hydrocarbon transport through the rock after fracking. Overall, our observations suggest that strain partitioning and differences in deformation style (brittle vs. ductile) at the grain scale significantly affect the response of the rock to imposed shear deformation and dictate whether microscale permeability enhancement may occur. The porosity response at sub-micron scales is directly affected by the abundance of clay minerals, the existing fabric of the rock, and the direction of loading relative to any existing fabric. On the basis of our results, we propose a mechanistic model in which shear failure increases porosity at the grain scale through a combination of brecciation, cataclasis, and dilatant shearing that exploits the contrast in mechanical strength among the different mineral components of the shale. The permeability enhancement associated with these processes arises due to the contrast in mechanical strength between clays and other materials: clay minerals can shear and slide past each other, but this style of deformation is arrested and transitions to a brittle, grain-fracturing style at the interfaces between clays and calcite, quartz, and organic matter. The fractures that propagate into the latter are guided by internal heterogeneity of mechanical strength and intersect the organic-hosted pores. The hydrocarbons contained in these pores are then free to migrate through the fractures in the organic matter and through the dilatantly sheared clays and other crushed inorganic matrix to the main induced tensile fracture system.

Evidence for this in the differences between the Eagle Ford and siliceous samples. The siliceous samples are finely laminated even at the micron scale, with individual lamina often composed of weak material such as clay and organic matter. In contrast, the Eagle Ford samples are massive to weakly laminated and do not typically exhibit the same lamina-scale partitioning of weak minerals. The deformation patterns are distinctly different between the two rocks. In the Eagle Ford samples, the distributed nature of the stronger minerals (calcite and quartz) creates a system of stress bridges that completely span the stronger grains, in many cases shielding the clay and organic matter from bearing an applied load. This is consistent with observations in younger, higher-porosity mudrocks during primary consolidation immediately following deposition (Schneider et al., 2011). Deformation in the Eagle Ford samples often manifests as parting along grain contacts with associated grain rotation and/or breakage. The localized shearing associated with these processes deforms the clays and organic matter, in some cases resulting in fractures propagating into the organic matter. In the siliceous samples, the stronger and weaker minerals are partitioned in discrete laminae. Like the Eagle Ford, the deformation is accommodated in the stronger layers by breakage along grain contacts, grain breakage, and grain rotation. However, since the weaker layers are not shielded from the applied load by stress bridges, the deformation in the weaker layers is more intense. Fractures tend not to propagate through the clay minerals, but show up as dilatancy between clay grain aggregates. The organic matter in the siliceous samples is often associated with clays or present as thin laminae. In both cases, because the organic matter is not composed of discrete particles but is more of a continuous solid, deformation is taken up by fracturing between zones of slightly differing mechanical strength (e.g., Wilkinson et al., 2015). The overall result is more intense dilatancy in

the weaker layers in the siliceous samples, in particular when loading occurs perpendicular to bedding, which maximizes the load that is borne by the weaker material.

This work has important implications for design and execution of hydraulic fracture stimulation. In microscopically isotropic shales like the Eagle Ford, greater amounts of shear deformation should be expected to increase the pore connectivity at the grain scale. Such shales should respond positively to higher injection pressures during fracking, as has been suggested by some studies (e.g., Centurion et al., 2012), since this will increase the shear stresses along existing natural fractures or imparted by the fluid in the induced tensile fractures. However, increased pressures are associated with increased safety risks, and more intensive fracking operations may translate to increased need for resources such as water and chemicals. Novel fracturing technologies that exploit the microscale deformation mechanisms in microscopically isotropic shales are needed to reduce the risks associated with fracking. In microscopically laminated shales like the siliceous samples we analyzed, the direction of stress application is an important component for maximizing microscale porosity enhancement during shear deformation. Loading perpendicular to bedding increases porosity enhancement because more deformation is borne by the weaker layers, including the organic matter. In such shales, preexisting fractures play an important role in determining the effectiveness of hydraulic fracturing, since the primary induced tensile fractures will tend to be oriented subvertically, directing shear stresses in the bedding-parallel direction. Preexisting fractures can allow stress to be transmitted perpendicular to bedding either by slipping or by filling with pressurized fracturing fluid. This may explain why existing joint sets are so important for production from other well-laminated shales such as the Marcellus (Engelder et al., 2009).

References

Bolton, A.J., Maltman, A.J., Fisher, Q., 2000. Anisotropic permeability and bimodal pore-size distributions of fine-grained sediments. *Mar. Petrol. Geol*., 17, 657-672.

Centurion, S., Cade, R., Luo, X., 2012. Eagle Ford shale: Hydraulic fracturing, completion, and production trends: Part II. SPE Annual Technical Conference and Exhibition, paper SPE 158501.

Coates, G.R., Xiao, L., Prammer, M.G., 1999. *NMR Logging Principles and Applications*. Houston, TX: Gulf Professional Publishing, 234 pp.

Chang, C., Zoback, M. D., Khaksar, A., 2006. Empirical relations between rock strength and physical properties in sedimentary rocks. *J. Petrol. Sci. Eng*., 51, 223-237.

Chapman, M., 2003. Frequency-dependent anisotropy due to meso-scale fractures in the presence of equant porosity. *Geophys. Prospect*., 51, 369–379.

Chapman, M., 2009. Modeling the effect of multiple sets of mesoscale fractures in porous rock on frequency-dependent anisotropy. *Geophysics*, 74, D97–D103.

Daigle, H., 2014. Microporosity development in shallow marine sediments from the Nankai Trough. *Mar. Geol*., 357, 293-303.

Delle Piane, C., Dewhurst, D.N., Siggins, A.F., Raven, M.D., 2011. Stress-induced anisotropy in brine saturated shale. *Geophys. J. Int*., 184, 897–906.

Engelder, T., Lash, G.G., Uzcategui, R.S., 2009. Joint sets that enhance production from Middle and Upper Devonian gas shales of the Appalachian Basin. *AAPG Bull*., 93(7), 857–889.

Fisher, M.K., Heinze, J.R., Harris, C.D., Davidson, B.M., Wright, C.A., Dunn, K.P., 2004. Optimizing horizontal completion techniques in the Barnett Shale using microseismic fracture mapping. SPE Annual Technical Conference and Exhibition, paper SPE 90051.

Frohlich, C., 2012. Two-year survey comparing earthquake activity and injection-well locations in the Barnett Shale, Texas. *P. Natl. Acad. Sci. USA*, 109(35), 13934-13938.

Gale, J.F.W., Reed, R.M., Holder, J., 2007. Natural fractures in the Barnett Shale and their importance for hydraulic fracture treatments. *AAPG Bull*., 91(4), 603–622.

Javadpour, F., Fisher, D., Unsworth, M., 2007. Nanoscale gas flow in shale gas sediments. *J. Can. Petrol. Tech*., 46(10), 55-61.

Jiang, C., Bryant, S., Daigle, H., 2015. A bundle of short conduits model of the pore structure of gas shale. Unconventional Resources Technology Conference, paper URTeC-2169349.

Jiang, M., Spikes, K.T., 2013. Estimation of reservoir properties of the Haynesville Shale by using rock physics modeling and grid searching. *Geophys. J. Int*., 195(1), 315-329.

Katsube, T.J., Williamson, M., Best, M.E., 1992. Shale pore structure evolution and its effect on permeability. Society of Core Analysts 1992 Symposium, paper 9214.

Kenyon, W.E., Kleinberg, R.L., Straley, C., Gubelin, G., Morriss, C., 1995. Nuclear magnetic resonance imaging - Technology for the 21st century. *Oilfield Rev*., 7(3), 19-33.

Keranen, K.M., Savage, H.M., Abers, G.A., Cochran, E.S., 2013. Potentially induced earthquakes in Oklahoma, USA: Links between wastewater injection and the 2011 Mw 5.7 earthquake sequence. *Geology*, 2011–2014.

Kuila, U., Prasad, M., 2011. Surface area and pore-size distribution in clays and shales. SPE Annual Technical Conference and Exhibition, paper SPE 146869.

Lastoskie, C., Gubbins, K.E., Quirke, N., 1993. Pore size distribution analysis of microporous carbons: A density functional theory approach. *J. Phys. Chem*., 97, 4786-4796.

Loucks, R.G., Reed, R.M., Ruppel, S.C., Jarvie, D.M., 2009. Morphology, genesis, and distribution of nanometer-scale pores in siliceous mudstones of the Mississippian Barnett Shale. *J. Sediment. Res.*, 79, 848–861.

Madonna, C., Quintal, B., Frehner, M., Almqvist, B.S.G., Tisato, N., Pistone, M., Marone, F. Saenger, E.H., 2013. Synchrotron-based X-ray tomographic microscopy for rock microstructure investigations. *Geophysics*, 78, D53-D64.

Maxwell, S.C., Waltman, C.K., Warpinski, N.R., Mayerhofer, M.J., Boroumand, N., 2009. Imaging seismic deformation induced by hydraulic fracture complexity. *SPE Reserv. Eval. Eng*., 12(1), 48-52.

Mayerhofer, M.J., Lolon, E.P., Warpinski, N.R., Cipolla, C.L., Walser, D., Rightmire, C.M., 2008. What is stimulated reservoir volume? *SPE Prod. Oper*., 25(1), 89-98.

Milliken, K.L., 2003. Late diagenesis and mass transfer in sandstone-shale sequences. In Holland, H.D., Turekian, K.K., eds., *Treatise on Geochemistry*, 7, 159-190.

Milliken, K. L., Esch, W. L., Reed, R. M., Zhang, T,. 2012a. Grain assemblages and strong diagenetic overprinting in siliceous mudrocks, Barnett Shale (Mississippian), Fort Worth Basin, Texas. *AAPG Bull*., 96(8), 1553–1578.

Milliken, K. L., Papazis, P. K., Dohse, C., Day-Stirrat, R. J., 2012b. Carbonate lithologies of the Mississippian Barnett Shale, Fort Worth Basin, Texas. In Breyer, J. A. (ed.), Shale Reservoirs - Giant Resources for the 21st Century, *AAPG Memoirs,* 97, 290-321.

Milliken, K.L., Rudnicki, M., Awwiller, D.N., Zhang, T., 2013. Organic matter-hosted pore system, Marcellus Formation (Devonian), Pennsylvania. *AAPG Bull*., 97(2), 177-200.

Myers, T. (2012a). Potential contaminant pathways from hydraulically fractured shale to aquifers. *Ground Water*, 50(6), 872–882.

Myers, T. (2012b). Author's Reply. *Ground Water*, 50(6), 828–830.

Passey, Q.R., Bohacs, K.M., Esch, W.L., Klimentidis, R., Sinha, S., 2010. From oil-prone source rock to gas-production shale reservoir - Geologic and petrophysical characterization of unconventional shale-gas reservoirs. CPS/SPE International Oil & Gas Conference and Exhibition, paper SPE 131350.

Pervukhina, M, Gurevich, B., Golodoniuc, P., Dewhurst, D.N., 2011. Parameterization of elastic stress sensitivity in shales. *Geophysics*, 76, WA147–WA155.

Ravikovitch, P.I., Neimark, A.V., 2002. Experimental confirmation of different mechanisms of evaporation from ink-bottle type pores: Equilibrium, pore blocking, and cavitation. *Langmuir*, 18(25), 9830-9837.

Ravikovitch, P.I., Ó Domhnaill, S.C., Neimark, A.V., Schüth, F., Unger, K.K., 1995. Capillary hysteresis in nanopores: Theoretical and experimental studies of nitrogen adsorption on MCM-41. *Langmuir*, 11, 4765-4772.

Roque-Malherbe, R.M.A., 2007. *Adsorption and Diffusion in Nanoporous Materials*. Boca Raton, FL: CRC press, 269 pp.

Sayers, C.M., 2013. The effect of anisotropy on the Young's moduli and Poisson's ratios of shales. *Geophys. Prospect*., 61, 416–426.

Schmitt, M., Fernandes, C.P., da Cunha Neto, J.A.B., Wolf, F.G., dos Santos, V.S.S., 2013. Characterization of pore systems in seal rocks using nitrogen gas adsorption combined with mercury injection capillary pressure techniques. *Mar. Petrol. Geol.*, 39, 138-149.

Schneider, J., Flemings, P. B., Day-Stirrat, R. J., & Germaine, J. T. (2011). Insights into pore-scale controls on mudstone permeability through resedimentation experiments. *Geology*, 39(11), 1011–1014.

Silin, D., Kneafsey, T., 2012. Shale gas : Nanometer-scale observations and well modelling. *J. Can. Petrol. Tech.*, 51(6), 464-475.

Soeder, D.J., 1988. Porosity and permeability of eastern Devonian gas shale. *SPE Formation Eval*., 3(1), 116-124.

Sondergeld, C.H., Ambrose, R.J., Rai, C.S., Moncrieff, J., 2010a. Micro-structural studies of gas shales. SPE Unconventional Gas Conference, paper SPE 131771.

Sondergeld, C.H., Newsham, K.E., Comisky, J.T., Rice, M.C., Rai, C.S., 2010b. Petrophysical considerations in evaluating and producing shale gas resources. SPE Unconventional Gas Conference, paper SPE 131768.

Spikes, K.T., Jiang, M., 2013. Rock physics relationships between elastic and reservoir properties in the Hayneseville Shale*. AAPG Memoirs*, 105, 189-203.

Tarazona, P., 1985a. Free-energy density functional for hard spheres. *Phys. Rev. A*, 31, 2672-2679.

Tarazona, P., 1985b. Erratum: Free-energy density functional for hard spheres. *Phys. Rev. A*, 32, 3148.

Tembe, S., Lockner, D.A., Wong, T., 2010. Effect of clay content and mineralogy on frictional sliding behavior of simulated gouges: Binary and ternary mixtures of quartz, illite, and montmorillonite. *J. Geophys. Res*., 115, B03416.

United States Environmental Protection Agency, 2011. Draft plan to study the potential impacts of hydraulic fracturing on drinking water resources. Report EPA/600/D-11/001. http://www2.epa.gov/sites/production/files/documents/HFStudyPlanDraft_SAB_020711.pdf.

Valenza, J.J., Drenzek, N., Marques, F., Pagels, M., Mastalerz, M., 2013. Geochemical controls on shale microstructure. *Geology*, 41(5), 611–614.

Walls, J.D., 2011. Digital rock physics provides new insight into shale reservoir quality. *E&P Mag.*, August 2011, 52-53.

Wang, F.P., Reed, R.M., 2009. Pore networks and fluid flow in gas shales. SPE Annual Technical Conference and Exhibition, paper SPE 124253.

Warpinski, N.R., Kramm, R.C., Heinze, J.R., Waltman, C.K., 2005. Comparison of single- and dual array microseismic mapping techniques in the Barnett Shale. SPE Annual Conference and Exhibition, paper SPE 95568.

Wilkinson, T.M., Zargari, S., Prasad, M., Packard, C.E., 2015. Optimizing nano-dynamic mechanical analysis for high-resolution, elastic modulus mapping in organic-rich shales. *J. Mater. Sci.*, 50(3), 1041-1049.

Williams-Stroud, S., Ozgen, C., Billingsley, R.L., 2013. Case History Microseismicity-constrained discrete fracture network models for stimulated reservoir simulation. *Geophysics*, 78(1), B37-B47.